Max-Planck-Institut
für Kolloid- und Grenzflächenforschung

Universität Potsdam

Max Planck Institut für Kolloid- und Grenzflächenforschung

Abteilung Biomaterialien

Biomedical applications and multifunctional nanostructures based on magnetite nanoparticles synthesized in presence of biological additives

Dissertation
zur Erlangung des akademischen Grades
"doctor rerum naturalium"
(Dr. rer. nat.)
in der Wissenschaftsdisziplin "Molekulare Biotechnologie"

eingereicht an der
Mathematisch-Naturwissenschaftlichen Fakultät
der Universität Potsdam

von
Victoria Eleonore Reichel

Potsdam, den 05.10.2016

„Wirklich ist alles, was meßbar ist“

Max Planck

ABSTRACT

Magnetotactic bacteria synthesize intracellular nanoparticles within an organelle called the magnetosome. These biomineralized nanoparticles consist of highly monodisperse stable single domain iron oxide nanoparticles and a surrounding membrane. The magnetosomes align into a chain by their attachment to a filament made of the protein MamK and through dipole-dipole interactions. Magnetotactic bacteria use their magnetosome chain as a compass needle to orient themselves within the earth's magnetic field to seek optimal living conditions. Isolated magnetosomes exhibit colloidal stability in solution due to their surrounding membrane, which makes them candidates for biomedical applications, e.g. hyperthermia or MRI contrast agents. In contrast, synthetic magnetite nanoparticles tend to aggregate, which is disadvantageous for these applications.

In this thesis, I followed a biomimetic strategy to overcome the limitations of such synthetically produce magnetite nanoparticles by mimicking the magnetosome chain. Magnetite nanoparticles were co-precipitated in a mild alkaline environment in the presence of poly-l-arginine. Colloidally stable 40 nm magnetite nanoparticles were formed when precipitated with the additive assembled into chain structures similar to magnetosome chains. Poly-l-arginine affects the size, morphology and assembly of the nanoparticles.

High resolution transmission electron microscopy, energy dispersive X-ray spectroscopy and small angle neutron scattering were applied to characterize the structural properties. Each 40 nm particle is composed of ~10 nm sub-units, yet diffract like a single crystal. Bulk magnetic measurements and magnetic induction maps recorded from individual particles using off-axis electron holography show that each 40 nm particle typically contains a single magnetic domain.

Consequently, each 40-nm polyR-magnetite nanoparticle is a real mesocrystal, comprising single crystallinity and stable single domain magnetic behavior. Its structural and magnetic properties are determined by the size of the superstructure rather than that of its components.

In addition, the small angle neutron scattering analysis showed a structural component called mass fractal, where the scattering is determined from individual magnetite mesocrystals. The mass fractal indicated the presence of internal organic between the ~ 10 nm sub-units.

Since the obtained nanoparticles are monodisperse, colloidally stable and exhibit stable single domain magnetic properties, we tested their potential in the above mentioned applications. PolyR-magnetite nanoparticles were non-toxic to a concentration of 100 µg/ml in static cell viability assays using human endothelial cells and thus, are comparable to the standard contrast agent Resovist®. Relaxivities of polyR-magnetite nanoparticles were performed in order to test their potential of contrast agents for magnetic resonance imaging. Our nanoparticles showed enhanced relaxivity performance than the standard contrast agent Resovist® according to their R2/R1 ratios of 17, whereas Resovist® achieves R2/R1 ratios of 11. Additionally, polyR-magnetite nanoparticles were tested towards their potential heating properties in hyperthermia. They exhibit specific absorption rates of 208 W/g, which shows five times better heating than of the standard material Ferridex®.

In an additional step to further mimic magnetosome chains, we compiled the polyarginine-magnetite nanoparticles with biogenic building blocks from magnetotactic bacteria. First, the polyarginine-magnetite nanoparticles were synthesized, with a fluorescent antibody directed against mCherry and finally the antibody nanoparticle conjugates were attached to the biogenic template made of the MamK_mCherry_His_6 filament. The formed multifunctional structure exhibits fluorescent as well as magnetic properties as shown by the actuation of the biomimetic construct with an external magnetic field.

ZUSAMMENFASSUNG

Magnetotaktische Bakterien besitzen die Fähigkeit magnetische Nanopartikel, die sogenannten Magnetosomen, intrazellulär in einem Organell herzustellen. Diese höchst monodispersen biomineralisierten Eisenoxid-Nanopartikel weisen magnetisch stabile Einzeldomänen auf und sind von einer Membran umgeben. Die Magnetosome richten sich durch magnetische Dipol-Dipol Wechselwirkungen und durch ihre Befestigung an ein Proteinfilament kettenförmig aus. Magnetotaktische Bakterien verwenden diese Magnetosomenketten als Kompassnadeln, um sich selbst im Erdmagnetfeld auszurichten und dadurch beste Lebensbedingungen anzustreben. Isolierte Magnetosome weisen kolloidale Stabilität in Lösung auf, welche durch ihre umgebende Membran erlangt wird. Diese Eigenschaft macht sie zu geeigneten Kandidaten in biomedizinischen Anwendungen, wie zum Beispiel in der Hyperthermie oder als Kontrastmittel in der Magnetresonanztomographie. Im Vergleich zu Magnetosomen, neigen synthetisch hergestellte Magnetitnanopartikel zur Aggregation, welches jedoch einen großen Nachteil für viele Anwendungen birgt.

In meiner Doktorarbeit wurden Magnetosomenketten nachgeahmt und nach deren Vorbild synthetische Magnetitnanopartikel hergestellt. Die Magnetitnanopartikel wurden mit Hilfe der Kopräzipitation unter Anwesenheit von Poly-L-Arginin in einer mild-alkalischen Umgebung erzeugt. 40 nm große, kolloidal stabile Magnetitnanopartikel wurden während der Kopräzipitation synthetisiert und bildeten mit Hilfe der Additive Kettenstrukturen aus, die denen der Magnetosomen stark ähnlich sind. Poly-L-Arginin beeinflusst somit die Größe, die Morphologie und das Aggregationsverhalten der Magnetitnanopartikel.

Hochauflösende Transmissionselektronenmikroskopie, energiedispersive Röntgenspektroskopie und Kleinwinkel Neutronenstreuung, wurden zur Charakterisierung der strukturellen Eigenschaften der synthetisch hergestellten Magnetitnanopartikel verwendet. Jedes einzelne 40 nm große Partikel weist ein Beugungsbild eines perfekten Einkristalls auf, obwohl es aus ca. 10 nm großen Untereinheiten zusammengesetzt ist.

Magnetische Messungen der gesamten Magnetitnanopartikelsuspension und magnetische Induktionskarten, die von individuellen Partikeln mit Hilfe von Elektronenholographie aufgezeichnet wurden, wurden zu Analyse der magnetischen Eigenschaften der Kristalle verwendet. Es konnte gezeigt werden, dass jedes 40 nm große Partikel eine magnetisch stabile Einzeldomäne aufweist.

Jedes 40 nm Poly-L-Arginin-Magnetitnanopartikel besitzt ein Beugungsbild eines Einkristalls und zeigt ein magnetisch stabiles Einzeldomänen-Verhalten. Das weist daraufhin, dass jedes Partikel ein echter Mesokristall ist, da seine strukturellen und magnetischen Eigenschaften durch seine Gesamtgröße und somit der Superstruktur und nicht durch dessen einzelnen Untereinheiten bestimmt wird.

Mit Hilfe von Kleinwinkel-Neutronenstreuung konnte ein Strukturelement, das sogenannte Massenfraktal, gezeigt werden, dessen Streuung von einzelnen Mesokristallen bestimmt wird. Das Massenfraktal weist darauf hin, dass sich der organische Anteil auch zwischen den ca. 10 nm großen Untereinheiten eines einzelnen Mesokristalls befinden könnte.

Da die monodispersen Nanopartikel eine magnetisch stabile Einzeldomäne und kolloidale Stabilität besitzen, wurden diese für die oben erwähnten Anwendungen untersucht. Poly-L-Arginin-Magnetitnanopartikel sind bis hin zu Partikelkonzentrationen von 100 µg/ml in statischen Zell Viabilitätstests unter Verwendung von humanen Endothelzellen, nicht toxisch und somit mit dem Standardkontrastmittel Resovist® vergleichbar. Relaxivitätsmessungen der Partikel wurden durchgeführt, um deren Potential als mögliche Kontrastmittel zu prüfen. Die Partikel wiesen eine bessere Leistung als das Standardkontrastmittel Resovist® auf, welche sich durch ihre R2/R1 Rate von 17 im Gegensatz zu einer R2/R1 Rate von 11 für Resovist®, auszeichnete. Die Partikel wurden zusätzlich bezüglich ihrer Heizleistung in der Hyperthermie getestet. Sie zeigten spezifische Absorptionsraten von 208 W/g und wiesen eine fünfmal bessere Heizleistung im Gegensatz zu Ferridex® auf.

Um die Eigenschaften der Magnetosomenketten nachzuahmen, wurden Poly-L-Arginin-Magnetitnanopartikel mit biogenen Bausteinen aus magnetotaktischen Bakterien vereint.

Als erstes wurden die Poly-L-Arginin-Magnetitnanopartikel synthetisiert, woraufhin diese mit fluoreszierenden anti-mCherry Antikörpern funktionalisiert wurden, welche des Weitern an die biogene Schablonen, dem MamK_mCherry_His_6 Filament, befestigt wurden. Die daraus geformte multifunktionelle Struktur weist fluoreszierende und auch magnetische Eigenschaften auf. Der Antrieb dieser Struktur in einem externen Magnetfeld wird dadurch ermöglicht.

TABLE OF CONTENT

1. INTRODUCTION AND OBJECTIVES OF THE WORK

Magnetite accompanies us in various situations and plays a crucial role in our daily life. If somebody is going to an organ screening in hospital, magnetic materials, especially magnetite, is applied (Ito et al., 2004). Tumors can be visualized and a diagnosis can be made through magnetic resonance imaging, using magnetite nanoparticles as contrast agents (Na et al., 2009). Furthermore, diseases can be treated with the help of magnetic nanoparticles and their heating capacities in hyperthermia (Thiesen and Jordan, 2008). Magnetic properties of iron oxides in general, but of magnetite in particular, are used in paleo- and geomagnetic reconstruction (Geiss et al., 2008). The minerals help reconstruct past climates and continents positioning through preserving of the main vectors of the Earth's magnetization (Acton, 2011). Sailors in ancient times were using magnetic materials as well. The lodestone was used for navigation, which was the earliest known magnetic compass (Annett, 1921). Hence, various applications require magnetite nanoparticles. Magnetite ($Fe^{II} Fe_2^{III} O_4$, Fe_3O_4) is one of a number of iron oxide phases that can be found in nature and it is also synthesized in the laboratory (Cornell and Schwertmann, 2003), (Schwertmann and Cornell, 2007), (Wiberg, 2001). Research on magnetite nanoparticles ranges from fundamental questions about the mechanisms of nanoparticle formation following nucleation of a few atoms to the fabrication of functional magnetic materials, their use in technological and medical applications and biomimicking of magnetite nanoparticle synthesis in organisms (Baumgartner et al., 2014).

When making a brief excursus in the biological world of magnetotactic bacteria, one will realize that these tiny creatures are able to synthesize magnetite nanoparticles, called the magnetosomes, within their cell bodies (Faivre and Schuler, 2008). The bacteria owe a various set of organic macromolecules, which exhibit fascinating tools for synthesis and stabilization of magnetite nanoparticles (Jogler and Schüler, 2009). Each nanocrystal is trapped in a membrane invagination of the cell and fixed on a protein filament forming the magnetosome chain. Their magnetic crystals exhibit monodispersity, colloidal stability and show single domain magnetic properties. They use their magnetosome chain to align within the earth magnetic field (Faivre and Bennet, 2016). This helps them to orient in their environment and to seek optimal living conditions (Faivre and Schuler, 2008), (Uebe and

Schüler, 2016). When magnetic nanoparticles exceed a certain size regime, as they do in magnetosomes (Figure 1b), stable single domain magnetic behavior is observed, whereas their permanent magnetic dipoles interact with each other resulting in chain formation of the nanoparticles (Kiani et al., 2015). These nanoparticle chain-like assemblies would typically collapse into clusters or closed-ring structures, so-called flux-closure rings, due to their favored energy state and if no further stabilization is guaranteed (Hu et al., 2008). In case of magnetosomes, it was shown that magnetosome chains are stabilized through their attachment onto semi-flexible MamK filaments with the help of MamJ proteins (Kiani et al., 2015).

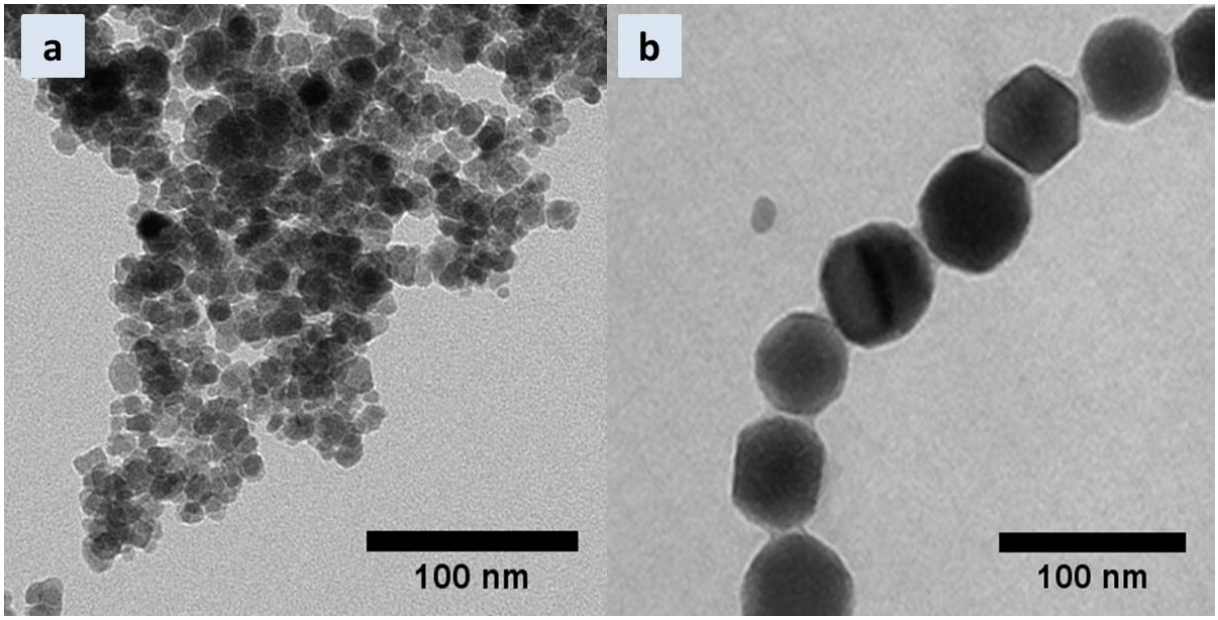

Figure 1: (a) Magnetite nanoparticles formed in the co-precipitation method without additives. (b) Isolated and purified magnetosome chain from Magnetospirillum magneticum strain AMB-1.

In contrast to biogenic magnetite, synthetic magnetite can be produced using various routes of magnetite nanoparticle synthesis (Schwertmann and Cornell, 2007), (Roca et al., 2009), (Faivre, 2016). An approach of magnetite nanoparticle synthesis is the co-precipitation method, whereas ferrous and ferric iron are added in an alkaline environment at room temperature (Massart, 1981). Synthetically-produced magnetite nanoparticles with such technique tend to form aggregates (Figure 1a), which is a limitation to their usability (Vikesland et al., 2016). In general, colloidal stability of a magnetite nanoparticle dispersion

(Park et al., 2009) is challenging to achieve. Furthermore, magnetite nanoparticles tend to precipitate in a polydisperse manner. However, in nanotechnology, monodispersity is highly desirable to guarantee a suitable nano-system for further applications. Different additives were investigated to keep magnetic nanoparticles monodisperse and colloidal stable. Polymers, such as polyethylenimine, further peptides and proteins, fatty acids, e.g. oleic acid, are widely used additives during the synthesis of magnetite nanoparticles (Laurent et al., 2008), (Kovalenko et al., 2007). Furthermore capsids, which are empty virus shell proteins, liposomes, and micelles are used to entrap magnetite nanoparticles inside nanocontainers (Qazi et al., 2012), (Reichhardt et al., 2011). These additives are used due to their charge, structure, hydrophilicity, and the molar ratio between iron and additive (Zhongjun et al., 2009).

Magnetite is negatively charged in alkaline medium and the electrostatic interaction of positively charged molecules is most favorable (Tombacz et al., 2006). Thus, positively charged macromolecules directly interact with precipitated magnetite and monodisperse, colloidal stable particles are produced (Baumgartner et al., 2014).

It was observed, that magnetite nanoparticles can form mesocrystalline-like or flower-like structures when precipitating in presence of organic additives (Wan et al., 2015), (Zhang et al., 2006), (Wang et al., 2006). If magnetite nanoparticles fulfill all the prior mentioned criteria, they are ready to be tested regarding to possible applications. Iron oxide nanoparticles are used as T2 negative contrast agents resulting in a dark signal in magnetic resonance imaging (MRI) and are applied in hyperthermia (Ito et al., 2005). The size, shape, stability, magnetic properties and biocompatibility highly influence their performance for the prior mentioned medical applications (Dutz and Hergt, 2014).

To further enhance properties of magnetite nanoparticles for biomedical applications, bio-conjugation of a variety of bioactive macromolecules, such as peptides, or fluorescent coated antibodies were investigated (Wang et al., 2011). The interest of growing multifunctional structures, creating a biomimetic magnetosome chain, grew, as it was shown that extracted magnetosome chains show antitumoral activity when exposed to a magnetic field (Philipse and Maas, 2002). In recent years, various hierarchical structures and template based synthesis, e.g. a genetically variant of human ferritin was fused to a silver binding peptide, which was then further used as a template for silver nanoparticle growth, was

investigated (Meldrum et al., 1992). However, the chemical stability of templates is limited, thus the synthesis of silver particles requires harsh synthesis conditions. In our recent paper, a three-fold step mechanism to mimic the magnetosome chain was shown. Particles were first synthetized, then conjugated to a specific antibody and afterwards linked to a recombinant protein filament. A magnetosome-like chain was assembled, which is affected by magnetic fields (Jehle et al., 2016).

1.2 OBJECTIVES

1.2.1 POLYR-MAGNETITE NANOPARTICLES: STRUCTURE, MAGNETIC PROPERTIES AND FORMATION MECHANISM

The general objective of this work is to better understand the possible formation of stable single domain (SSD) magnetite nanoparticles in the presence of a biological additive, poly-l-arginine (polyR), using the co-precipitation method. Magnetic properties are affected by particle sizes, morphologies and the particle size distribution. Typically, synthesized magnetite nanoparticles are considered to be superparamagnetic (SP) and it is difficult to form monodisperse stable single domain (SSD) magnetic nanoparticles, especially from an aqueous-based process. 40 nm colloidal stable and monodisperse flower-like SSD magnetite nanoparticles are formed and consist of sub-units in a superparamagnetic (SP) size regime. The flower-like shaped nanoparticles are suggested to be mesocrystals. A true mesocrystal is composed of small sub particles but its structural properties are determined by its superstructure.

Specifically, the aim of this work is to discover if the superstructure of polyR-magnetite nanoparticles is dictating the structural properties as well as the magnetic behavior, according to form real magnetic mesocrystals.

Another outstanding feature is the organic distribution of the polyR-magnetite nanoparticles, especially within the internal structure of each particle. Methods such as bulk magnetic and electron holography measurements were used for the determination of the magnetic properties and high resolution transmission electron microscopy was utilized to identify the crystalline structure of each nanoparticle. Small angle neutron scattering was investigated for the analysis of the distribution of polyR within polyR-magnetite nanoparticles.

1.2.2 POLYR-MAGNETITE NANOPARTICLES AS POTENTIAL MEDICAL TOOLS

The next goal was to evaluate the effects of monodisperse, colloidal stable and SSD polyR-magnetite nanoparticles on cell viability *in vitro* to ensure their usability for biomedical applications. In this work, first results of the particle`s potential for MRI contrast agents and their performance in hyperthermia were discussed. Their advantages and disadvantages in comparison to already established nanosystems in biomedicine were specified.

1.2.3 FORMATION OF ORDERED MATERIALS BASED ON POLYR-MAGNETITE NANOPARTICLES

The last goal of this work was to create a multifunctional biomimetic assembly using recombinant MamK_mCherry_His_6 filaments, which are utilized as biological templates to bind synthetic polyR-magnetite nanoparticles in order to attempt the reconstruction of the magnetosome chain. Anti-mCherry antibodies containing a fluorescent dye (Alexa Fluor®) were prior conjugated to polyR-magnetite nanoparticles, in order to bind the specific mCherry recognition sites of the filament. A method such as high resolution transmission electron microscopy was used for imaging the multifunctional assembly of antibody-conjugated nanoparticles on protein filaments. Fluorescent labeling and actuation in an applied magnetic field were utilized to prove the particle-antibody-filament attachment.

2. BACKGROUND AND METHODS

2.1 SYNTHETIC FORMATION OF MAGNETITE

2.1.1 THE DIFFERENT SYNTHETIC ROUTES OF MAGNETITE

Synthetic magnetite nanoparticles can be formed via many different routes (Laurent et al., 2008). Possible approaches include reactions in constrained environments (Nassar and Husein, 2006), hydrothermal reactions (Daou et al., 2006), flow injection synthesis (Salazar-Alvarez et al., 2006), polyol methods (Daou et al., 2006), sol-gel reactions (Cai and Wan, 2007), aerosol/vapor methods (Kumfer et al., 2010), electrochemical methods (Cabrera et al., 2008), sonolysis (Cano et al., 2010) and the classical co-precipitation (Baumgartner et al., 2013b) to name a few. In one important method, the sol-gel method, the materials are produced from small monomers, which are converted into a colloidal solution that acts as a precursor for an integrated network of particles (Wei et al., 2015). Sol-gel syntheses are performed at room temperature and the product acquires the final crystalline state via aging (Vinogradov and Vinogradov, 2014). High-temperature and hydrothermal reactions are also used to form magnetite nanoparticles (Laurent et al., 2008). In these cases, ultrafine powders are formed at temperatures above 200°C. The particle size increases with time, which can result in larger magnetite aggregates. In this thesis, the co-precipitation technique was used.

2.1.2 CO-PRECIPITATION OF MAGNETITE

The co-precipitation technique is the most widely utilized route to produce magnetite nanoparticles in large amounts due to its simplicity, high yield, and low cost (Vayssieres et al., 1998). Iron salts such as chlorides are dissolved in a stoichiometric ratio for magnetite (Fe(II) / Fe(III) = 1 / 2) at pH 1 – 1.5 and initially form monomeric iron in solution (Baumgartner et al., 2013a; Massart, 1981). The co-precipitation method consists in increasing the pH by addition of a base (e.g. sodium hydroxide). Upon pH increase, the monomeric iron species hydrolyze and then polymerize due to oxolation and olation reactions. Olation is a reaction by which metal ions form polymeric hydroxides from aquohydroxo complexes by the elimination of water. Subsequently, in oxolation reaction, the hydroxo (Fe-OH-Fe) bridges found in the iron polymer complexes are replaced by oxo

(Fe-O-Fe) bridges (Jolivet et al., 2004). If olation is slow compared to oxolation, the solid will be an oxide (this is the case of magnetite). If it is faster, the coexistence of oxo and hydroxo bridges will lead to an oxyhydroxide (such as ferrihydrite). In order to form magnetite, the co-precipitation reaction takes place under continuous stirring, at room temperature, and under nitrogen atmosphere to avoid oxidation and therefore maghemite formation.

2.1.3 MAGNETITE FORMS FROM PARTICULATE INTERMEDIATES: DESCRIPTION OF THE "NON-CLASSICAL" ROUTE

A drawback of the synthesis of magnetite nanoparticles using the co-precipitation technique is that typically only SP particles can be obtained. Therefore, efforts were developed in recent years to control the particle size of the magnetite nanoparticles. The standard co-precipitation technique was modified and nanoparticles were shown to be growing beyond the superparamagnetic / stable single domain threshold value (Baumgartner et al., 2013b). Two minutes after the initial addition of iron chloride to the dilute sodium hydroxide solution, so-called primary particles are observed. These primary particles exhibit dimensions of about 2 nm in diameter. Primary particles subsequently aggregate in branched networks, which become denser after 6 minutes, forming spheroidal nanoparticles of magnetite as shown by the reflections on the high resolution images (Baumgartner et al., 2013b). These first magnetite particles exhibit sizes of about 10 nm in diameter. With increasing reaction time, the magnetite nanoparticles increase in size. The crystal surfaces exhibit high surface roughness attributed to the presence of primary particles on the surface of the growing magnetite crystals. In the moment of accretion, the dimension of the primary-particles decreases to around 1 nm on the surface. Potential explanations of this size decrease include contraction due to water loss concomitant with olation or oxolation bond formation and/or partial re-dissolution. Therefore, the primary particles are not only involved in the nucleation of synthetic magnetite nanoparticles but are also critical for their growth (Baumgartner et al., 2013b).

2.1.4 MAGNETITE SYNTHESIS IN THE PRESENCE OF BIOLOGICAL ADDITIVES

Magnetotactic bacteria (MTB) are gram-negative bacteria, which consists of an organelle that consist of iron oxide stable single domain (SSD) nanoparticles with a surrounding membrane, called the magnetosome. The formation of magnetosomes is controlled by a set

of genes (*mam*: magnetosome membrane and *mms*: magnetosome membrane specific), which are clustered in the magnetosome island (Schübbe et al., 2003), (Bazylinski and Frankel, 2004; Ullrich et al., 2005). They are responsible for the magnetosomes biomineralization and their organization. The lately discovered mad genes were associated with the control of magnetosome morphology and are specific to strains forming elongated magnetosomes (Lefèvre et al., 2013). Additionally, the role of proteins in mainly: *M.gryphiswaldense* (MSR-1) and *M.magneticum* (AMB-1) strains has been studied in detail. The proteins MamG, MamF, MamD and MamC help in the control of the magnetosome size and are found in the magnetosome membrane (Scheffel et al., 2008). For magnetosome chain stabilization, MamK, a bacterial actin-like filamentous protein, is responsible (Katzmann et al., 2010). Furthermore, MamJ anchors the magnetosomes to the MamK filaments (Lin et al., 2014). The arrangement of other proteins into functional complexes within the magnetosome membrane is driven by MamE and MamO (Lower and Bazylinski, 2013). To establish the physical and chemical conditions needed for magnetite precipitation, MamP is involved in controlling the redox condition within the magnetosome organelle (Siponen et al., 2013b). The first protein, which was identified to possibly affect magnetite formation *in vitro* is the Mms6 protein, originating from *M. magneticum* AMB-1 (Arakaki et al., 2003). Stable single domain particles, both *in vivo* and *in vitro*, were obtained due to Mms6 controlling the magnetite size (Murat et al., 2012). MamJ, which is the anchor of magnetosomes to the MamK filament, owes acidic residues, which are eventually binding moieties for cationic $Fe^{II/III}$. A strong effect on aggregation, morphology, crystallinity, particle size and phase of the precipitate is obtained, when using MamJ as an additive (Baumgartner et al., 2014). MamP is another protein exclusively found in MTB and represents a new class of c-type cytochromes, acting as an iron oxidase. It contributes to the ferrihydrite formation, which is possibly needed for crystal growth of magnetite *in vivo*. In magnetite crystal formation a precise Fe^{III}/Fe^{II} ratio is required and MamP enables the formation of the ferrihydrite precursor, which, when Fe^{II} is present in addition, develops towards magnetite in the magnetosome or *in vitro* (Siponen et al., 2013a). Recently, the magnetosome membrane specific protein F (MmsF) has been discovered in *Magnetospirillum magneticum* strain AMB-1. MmsF is most likely a protein shell, which is termed the proteinosome, which is not solely an aggregation of a uniform protein density. Magnetite nanoparticles were precipitated within the MmsF self-assembled water soluble proteinosomes *in vitro*, whereas magnetite

nanoparticles formation was strictly controlled. Magnetite nanoparticles increased in size and displayed a more defined morphology, unambiguous with magnetosomes of *Magnetospirillum magneticum* strain AMB-1 (Rawlings et al., 2014). Isolated magnetosomes are colloidally stable in solution due to their surrounding membrane in certain concentrations (Faivre and Godec, 2015). Commonly, synthetic magnetite tends to aggregate, which is disadvantageous for many applications. Therefore, additives were introduced, which stabilize the magnetite nanoparticles. It is of great interest to biomimic the magnetosome membrane building blocks and to investigate new additives within the magnetite synthesis. Polymers, such as polyethylenimine, or fatty acids, e.g. oleic acid (Kovalenko et al., 2007), are widely used additives during the synthesis of magnetite nanoparticles (Laurent et al., 2008), (Kovalenko et al., 2007) . Furthermore capsids, which are empty virus shell proteins, and micelles are used to synthesize magnetite nanoparticles inside nanocontainers (Qazi et al., 2012), (Reichhardt et al., 2011). These additives are used due to their e.g. charge, structure, hydrophilicity, and the molar ratio between iron and additive (Zhongjun et al., 2009). Polypeptides such as poly-L-glutamic acid (polyE) and poly-L-arginine (polyR) are also used for *in vitro* studies (Baumgartner et al., 2014). The main difference in these polypeptides is the availability of different charged groups, which can non-specifically interact with iron or iron (oxyhydr) oxide species in different manners. It has been shown, that polycationic polypeptides preferably attach to magnetite crystals (Baumgartner et al., 2014). In the case of the highly positive charged poly-amino acid “poly-l-arginine” (polyR), its cationic guanidinium group can electrostatically interact with negatively charged iron (oxyhydr) oxide crystal surfaces in alkaline environment (Lai et al., 2009). PolyR affects the size, morphology and aggregation behavior of the formed magnetite nanoparticles. Stable-single-domain sized and highly monodispersed stable nanoparticles are formed, which are able to assemble into a chain structure in solution (Baumgartner et al., 2014). The colloidal stability of these synthetic magnetite nanoparticles is similar to the colloidal stabilization of magnetite crystals by magnetosome membranes in magnetotactic bacteria. In magnetosomes, the compartmentalization is based on a lipid-bilayer, where the lipids expose mainly positively charged amines toward the intracellular magnetite crystal (Baumgartner et al., 2014). In addition, the size and shape of the magnetite crystals could be regulated by varying the amino acid composition of the peptide (Lenders et al., 2015).

2.1.5 EXCURSE: MESOCRYSTALS

Mesocrystals are normally grown in a micrometer scale regime and they are mainly found in nature. A mesocrystal is a microscopically structured crystal which forms a superstructure of crystals with mesocopic size. Crystalline sub-units are assembled into perfect 3D structures (Cölfen and Antonietti, 2008). It is difficult to distinguish between a mesocrystal and a single crystal as they show identically scattering patterns. Therefore, microscopy techniques are used to proof the mesocopic sizes of sub-units. Typically, mesocrystals form through a nonclasscial crystallization route, which is observed in nature as well. Mesocrystal alignments are formed by an organic matrix or compartments are filled by the organic matter. Inorganic particles attach and nucleate to the organic. A critical volume fraction within the formation of the crystals has been reached to form crystal structures, which align mutually. The higher the volume fraction, the higher entropic forces and the easier regular packing and ordering of crystals occur. A constrained reaction environment with a constant influx of reactants is needed for the crystallization (Niederberger and Cölfen, 2006). Having a closer look in biomineralization, the amorphous precursor material deposited in an early stage of growth and the organic matrix plays an important role. Mesocrystals exhibit various properties, such as single crystal like behavior, high crystallinity and porosity, an inner connection bridging by organics and/or inorganics (Zhou and O'Brien, 2008), (Cölfen and Mann, 2003). They show larger surfaces than seen in perfect single crystals (Cölfen and Antonietti, 2005).

2.1.6 EXPERIMENTAL

2.1.6.1 SYNTHESIS OF $^{57}FeCl_2$ AND $^{57}FeCl_3$

To perform magnetite synthesis, two main precursor ingredients were used, which are ferrous and ferric chloride (Falbe and Regitz; Kruse, 1997). Typically, these iron chlorides are purchased from a commercial vendor, however iron isotopes are additionally used in magnetite synthesis for small angle neutron scattering experiments (see chapter 2.1.6.2), which are solely available in metal ^{57}iron pieces. Ferrous chloride is obtained by the reaction of metallic iron with hydrochloric acid under an oxygen free atmosphere, e.g. N_2, whereas ferric chloride can be synthesized by the reaction of metallic iron with hydrochloride acid within an oxidizing environment, e.g. O_2, or H_2O_2.

$$Fe + 2\,HCl \rightarrow FeCl_2 + H_2 \qquad \textit{Eq.1}$$

$$2\,Fe + 6\,HCl + 3\,H_2O_2 \rightarrow 2\,FeCl_3 + 6\,H_2O \qquad \textit{Eq. 2}$$

Metal ^{57}iron pieces were purchased from Trace Science International and were used without further purification. A vacuum distillation apparatus (Figure 2) was used and the metal iron was inserted in a 3 neck bottle flask, which was continuously flushed with nitrogen. Additionally, a degassed 37 % solution of HCl was added to the metallic iron via a syringe through a buckler. The temperature was kept at 60°C using a water bath under continuous stirring. To produce $^{57}FeCl_2$, the reaction had to be performed in a strict nitrogen atmosphere to prevent oxidation of any metallic iron. $^{57}FeCl_3$ was produced using a reaction vessel, which was flushed with air instead of nitrogen. To increase the oxidation, 2 ml of 37 % H_2O_2 was added to the reaction vessel, after fully dissolving of the metallic iron. After dissolving the metallic iron in HCl, either $^{57}FeCl_2$ or $^{57}FeCl_3$, depending on an inert atmosphere or oxidizing conditions was produced. The HCl was removed via evaporation in a vacuum distillation apparatus connected to a vacuum pump. Additionally, a reflux condenser was installed within the apparatus. $^{57}FeCl_2$ or $^{57}FeCl_3$ powder was dissolved in H_2O MilliQ and could be directly used for further experiments. The Ferrozin assay was used to distinguish between $^{57}FeCl_2$ (Carpenter and Ward, 2010). The total ^{57}Fe concentration was analyzed using an Inductively Coupled Plasma Optical Emission Spectrometry (ICP OES) device (Hou et al., 2000).

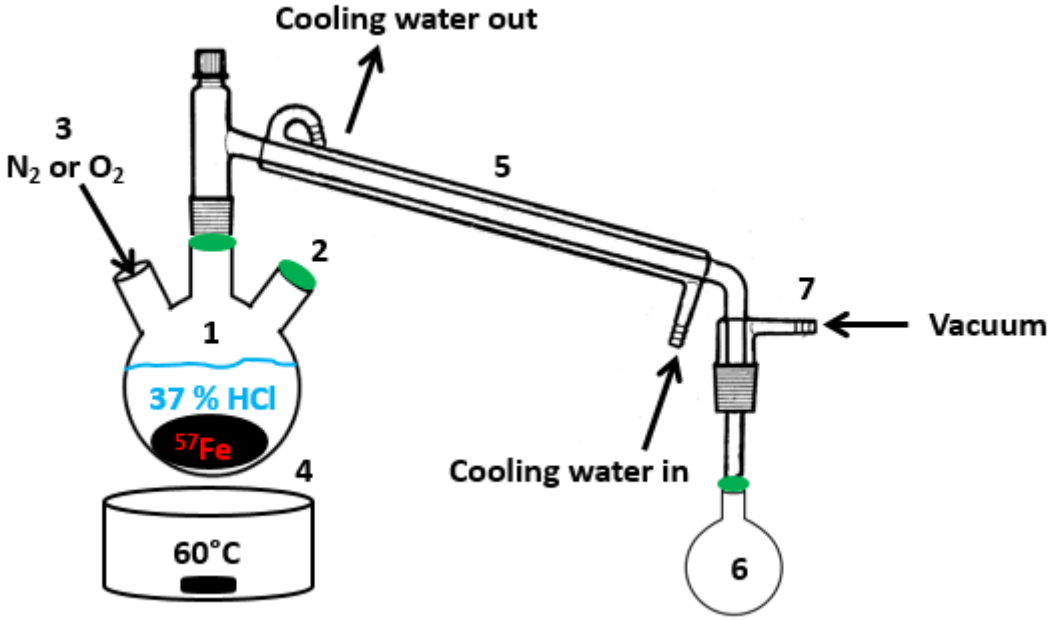

Figure 2: $^{57}FeCl_2$ and $^{57}FeCl_3$ production in a vacuum distillation apparatus: (1) 3-neck bottle flask filled with either iron powder or ^{57}Fe isotope metal pieces with additionally 37 % HCl, which was added through a (2) buckler. (3) Either nitrogen for the production of $^{57}FeCl_2$ or oxygen for the production of $^{57}FeCl_3$ was introduced, additional H_2O_2 could be added through (2) the buckler to enhance the oxidation. (4) During the whole process the solution was continuously stirred and heated up to 60°C through a water bath. During the whole process, (5) the device is cooled using a Liebig condenser. (6) The access of HCl was collected in during the vacuum distillation process, whereas the vacuum was applied through (7).

2.1.6.2 Co-precipitation method

Magnetite nanoparticles were synthesized by co-precipitation in aqueous solution (Baumgartner et al., 2013a). Ferrous and ferric iron chloride salts form magnetite by hydrolysis with sodium hydroxide within an alkaline milieu.

$$FeCl_2\,(aq.) + 2\,FeCl_3\,(aq.) + 8NaOH\,(aq.) \rightarrow\ Fe_3O_4\,(\downarrow) + 4\,H_2O + 8\,NaCl\,(aq.) \qquad \textit{Eq. 3}$$

All reagents were purchased from a commercial vendor and were used without further purification. A computer-controlled titration device was used (Metrohm AG). The device consists of a titration unit (Metrohm Titrino 888) containing a 5 ml cylinder, a dosing unit

(Metrohm Dosimat 805) containing 1 ml unit and a Biotrode pH electrode (Figure 3a). A 50 ml reaction vessel (Figure 3b) with the thermostat was used and the temperature was kept constant at 25°C. The reactor was kept under a controlled nitrogen atmosphere. All solutions were deoxygenated with nitrogen. The reaction vessel was filled with 10 ml of H_2O MilliQ to which poly-L-arginine (15.000 MW – 70.000 MW) was added to a final concentration of 0.1 mg/ml. Iron (II) chloride tetrahydrate and iron (III) chloride hexahydrate, purchased from Sigma Aldrich, were used in a stoichiometric ratio of magnetite (Fe^{II}/Fe^{III} = ½) to prepare a 0.1 M iron solution. A 0.1 M NaOH solution, purchased from Merck, was used for titration. The reaction was started by addition of the iron solution (1 µl/min) to the reaction vessel containing the poly-L-arginine solution under continuous stirring using a mechanical stirrer. The pH value was kept under permanent control at pH 11 using the NaOH titration unit and a pH electrode. Pure magnetite nanoparticles were precipitated identically as described above, without any additive in the reaction vessel and varying pH (9-11). The flow rate of the iron solution was 1 µl/min. The particle solution was washed three times with H_2O MilliQ from sodium chloride residues via magnetic separation and resuspended in H_2O MilliQ.

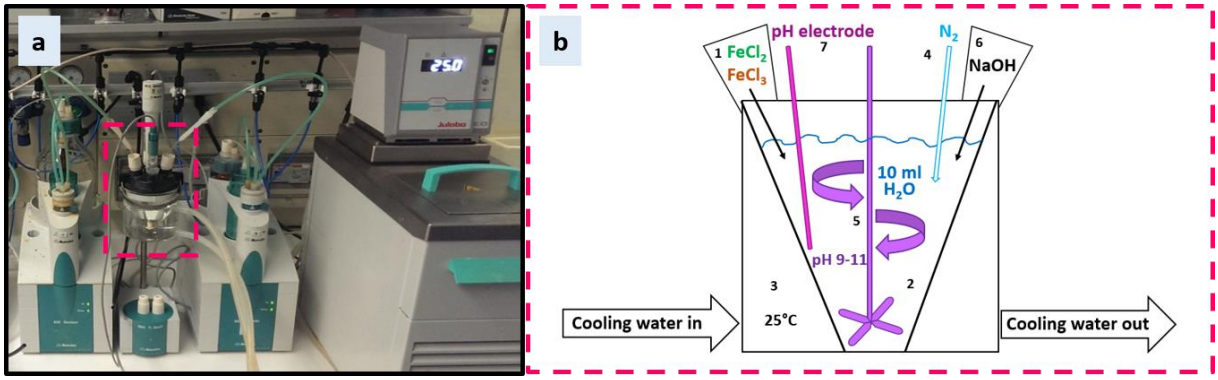

Figure 3: (a) Photograph of titration device for magnetite co-precipitation. (b) Co-precipitation synthesis vessel: (1) $FeCl_2$ and $FeCl_3$ were added to (2) 10 ml H_2O MilliQ in a 50 ml reaction vessel with (3) thermostat at 25°C under controlled (4) nitrogen atmosphere and (5) continuously stirring. (6) NaOH was used for titration and the pH value was monitored continuously using a (7) pH electrode.

2.2 ELECTRON MICROSCOPY (EM)

Electron microscopy is used to analyze structures of materials, such as nanoparticles, capsids and filaments (Williams and Carter, 1996). The resolution (d) is limited by λ and by the numeric aperture of the system (NA) and is given by the Abbe equation

$$d = \frac{\lambda}{2n\,sin\alpha} \approx \frac{\lambda}{2NA} \qquad \textit{Eq. 4}$$

where n is the refractive index, α is half the aperture angle and λ it the radiation wavelength. In electron microscopy, electrons with short wavelengths are used so that a resolution down to the Angström level is typically obtained.

Field emission guns or heated filaments are used to emit electrons, which are accelerated by applying high electric potentials of several hundred kV. Emitted electrons have a wavelength of

$$\lambda = \frac{h}{\sqrt{2m_e eU}} \qquad \textit{Eq. 5}$$

, where m_e is the particle mass, h is the Planck constant, and the kinetic energy of electrons in a potential field $1/2\ mv^2 = eU$ according to the de Broglie relation

$$\lambda = h/mv. \qquad \textit{Eq. 6}$$

When the energy of the detecting source is increased, the wavelength λ decreases, resulting in a better resolution. Energies up to 1 MeV are available nowadays, which permits images in the sub-nanometer scale.

2.2.1 SCANNING ELECTRON MICROSCOPY (SEM)

SEM is a scanning technique, where magnetic lenses are used to focus an electron beam to one spot, which scans over a specimen surface. Images are generated either by the detection of elastically backscattered electrons, or by secondary electrons, which are emitted from the surface of a sample due to inelastic scattering events of the incident beam. Scanning electron microscopy images give topographical information of sample surfaces (Oatley et al., 1966).

2.2.1.1 EXPERIMENTAL: SEM

Scanning electron microscopy SEM was used for studying the morphology and structure of the samples. Therefore secondary electrons (SE) and a back-scattered electron (BSE) detector were used. EDXS (Energy Dispersive X-ray Spectroscopy) spectra were recorded using two EDXS detectors and acceleration voltages up to 15 kV.

Samples for SEM analysis were prepared as following: 20-50 µl of the sample suspension was dropped on a SiO_2 wafer, which was placed on top of an aluminum sample holder with an additional conductive film. The samples were sputtered using a gold-platinum plasma. SEM images were obtained using a LEO 1550-Gemini and a JEOL JSM-7500F. The LEO 1550-Gemini was operated by Heike Runge and Rona Pitschke.

2.2.2 TRANSMISSION ELECTRON MICROSCOPY (TEM)

In TEM, an electron beam is passing through a specimen, interacts with the sample and the image is detected by a charge-coupled device (CCD) camera (Williams and Carter, 1996), (Pyrz and Buttrey, 2008). Diffraction patterns are formed in the back focal plane by the objective lens through electrons scattered by the specimen. They are combined to generate an image in the image plane. As it is an intermediate image, the diffraction pattern is simultaneously present in the TEM. It depends on the intermediate lens which of them appears in the plane of the second intermediate image. The projective lens magnifies the object on the viewing screen. One can switch from real space (image), to the reciprocal space (diffraction pattern) through the strength of the intermediate lens. When choosing the imaging mode, an objective aperture is inserted in the back focal plane to select one or more beams, which are contributing to the final image. Different variations such as Bright Field (BF), Dark Field (DF) and High Resolution TEM (HRTEM) can be chosen. An aperture in the plane of the first intermediate image defines the region of which the diffraction is obtained for the selected area electron diffraction (SAED). Heavy atoms guarantee a stronger interaction with electrons than light atoms, if the thickness of the sample is homogenous. Heavier atoms appear with darker contrast than light atoms (mass contrast). In thick areas, more electrons than in thin areas are scattered (thickness contrast). If an area is very thick but consists of lighter elements, the contrast is almost the same than for a thin specimen consisting of heavy atoms. Electrons are additionally stronger scattered at crystalline areas by Bragg diffraction, which appears as a dark contrast in BF images (diffraction contrast). To

summarize, the objective aperture blocks all scattered electron beams, which are deflected away from the optical axis. Thus the corresponding areas appear dark in BF images. For BF and DF imaging, the Bragg contrast and the mass-thickness contrast are of great importance (Williams and Carter, 1996).

2.2.2.1 EXPERIMENTAL: TEM

Low-magnification BF images were obtained using a Zeiss 912 Omega transmission electron microscope with an acceleration voltage of 120 kV.

Samples for transmission electron microscopy analysis were prepared as following: 10 µl of the sample suspensions were dropped on a Parafilm slice. A carbon coated copper grid was placed on the drop with the carbon side facing towards the fluid. The nanoparticle samples were placed there for 15 minutes at room temperature (RT) to get adsorbed to the carbon surface. The liquid phase was removed afterwards with a precision tissue paper (Kimwipe paper). To remove impurities the grids were washed twice by placing them on a drop of 10 µL d.d.H_2O for 5 min. In order to stain peptides and proteins, the grids were placed on a drop of 10 µl of 2 % uranyl acetate for 10 s. The uranyl acetate solution was removed from the grid with a precision tissue paper, followed by 3 washing steps. Some samples were additional prepared while positioning them inside a homogeneous magnetic field in order to align nanoparticles.

2.2.2.2 EXPERIMENTAL: HIGH RESOLUTION TRANSMISSION ELECTRON MICROSCOPY (HRTEM)

Low magnification bright-field (BF) images, high-resolution TEM (HRTEM) images and selected-area electron diffraction patterns were obtained using Philips CM20 and JEOL 3010 TEMs at accelerating voltages of 200 and 300 kV, respectively. Images were recorded either on image plates (on the Philips CM20) or using a Gatan Orius charge-coupled device (CCD) camera (on the JEOL 3010). Digital Micrograph and SingleCrystal software was used for TEM data processing and interpretation. Particle sizes were measured from digitized images using ImageJ software.

2.2.2.3 EXPERIMENTAL: ENERGY DISPERSIVE X-RAY SPECTROSCOPY (EDXS) AND ELECTRON ENERGY LOSS SPECTROSCOPY (EELS)

A probe-aberration-corrected FEI Titan 60-300 TEM was used for obtaining BF and high-angle annular dark-field (HAADF) scanning TEM (STEM) images. The annular dark-field detector inner semi-angle was 69 mrad. Elemental maps of Fe, O and C were obtained from spectrum images acquired using both EDXS and EELS. EELS spectrum images were also used to generate thickness maps of the particles. For spectrum imaging, low-loss and core-loss energy-loss spectra were recorded simultaneously using a Gatan dual-EELS Enfinium spectrometer.

Additionally, BF and HAADF STEM images were recorded using a FEI Tecnai™ F20X-Twin transmission electron microscope operating at 200 kV. HRTEM images and SAED patterns with corresponding FFT patterns were obtained. The EDAX system was used for EDXS. EELS (Electron Energy Loss Spectroscopy) spectra were recorded using a Gatan Tridiem system.

2.2.3 ELECTRON HOLOGRAPHY (EH)

The phase change of electron waves travelling through the specimen is measured using EH. The most popular technique of EH is the off-axis EH, in which the sample is coherently illuminated with a field emission electron gun. The beam is divided into two, one part illuminates the sample and the other is used as reference. Due to interaction with the sample, one part of the beam is modulated in amplitude and phase while the reference beam is not affected. A positively charged electrostatic biprism is used to superimpose the reference wave and the object wave resulting in a holographic interference pattern. This pattern is used to map, at the nanometer scale, the magnetic induction within and around materials. This induction recorded as a function of an applied field and/or temperature. The crystallography, morphology and particle interactions are inferred from the magnetic behavior (Dunin-Borkowski et al., 2004), (Faivre, 2016), (Midgley and Dunin-Borkowski, 2009).

2.2.3.1 EXPERIMENTAL: EH

EH experiments were performed using an image-aberration-corrected FEI Titan 60-300 TEM operated at 300 kV and a Fischione dual-axis tomography holder. Electron holograms were recorded in magnetic-field-free conditions in Lorentz mode using a Gatan direct electron

detection (K2-IS) camera in counting mode. This camera provides better signal-to-noise ratio and fewer pixel artefacts than a conventional CCD camera. In order to perform magnetization reversal experiments, the sample was tilted by ±75° and magnetized in the direction of the electron beam using the objective lens field of 1.41 T. The objective lens was then switched off, the sample tilted back to 0° in magnetic-field-free conditions and electron holograms of the resulting magnetic remanent states were acquired using a biprism voltage of 200 V. The sample was magnetized three times in opposite directions. Each magnetic induction map was created by adding phase contours to half of the difference between phase images recorded with the specimen magnetized in opposite directions. TEM images were processed using Gatan Digital Micrograph and Semper software.

2.2.4 ELECTRON TOMOGRAPHY (ET)

Electron tomography is used for visualization of 3D structures in the nano-meter range for macromolecular and sub cellular objects. TEM is used for the data collection, whereas the electron beam passes through a specimen at incremental degrees of rotation surrounding the center of the sample. Images are recorded about a tilt axis every one or two degrees, over as large a specimen tilt range as possible. This ensemble of the images is the template for 3D reconstruction (Midgley and Dunin-Borkowski, 2009).

2.2.4.1 EXPERIMENTAL: ET

Three-dimensional shapes of the particles were determined using electron tomography. HAADF STEM images were recorded at every 2º tilt in a range from +65º to -65º, using a Fischione single tilt tomography holder. The alignment of the images of and three dimensional object reconstruction was done using Tomato software (Houben and Sadan, 2011). To reconstruct the tomogram a standard simultaneous iterative reconstruction algorithm (SIRT) was applied. The tomogram was visualized using unregistered version of MeVisLab software.

2.3 MAGNETIC PROPERTIES OF NANOPARTICLES

Magnetite belongs to the ferrimagnetic materials, which is similar to ferromagnetic materials but its magnetic structure is comparable to an anti-ferromagnet. The electron spins and therefore their magnetic moments in a simple ferromagnet are aligned in one direction forming a large net magnetic moment in the material. Opposed to that, spins in an anti-ferromagnet are aligned that all magnetic moments are of equal magnitude but point to opposite directions and therefore owe a zero net magnetic moment. In the case of ferrimagnetic ordering, it is similar to anti-ferromagnetic ordering but with antiparallel spins with an unequal magnitude. Hence, the Fe^{3+} ions in both sites are aligned anti-parallel (Figure 4), which means that their magnetic moment of the unit cell only comes from the Fe^{2+} ions (Zhang and Satpathy, 1991), (Wyckoff and Wyckoff, 1960), (Hargrove and Kündig, 1970).

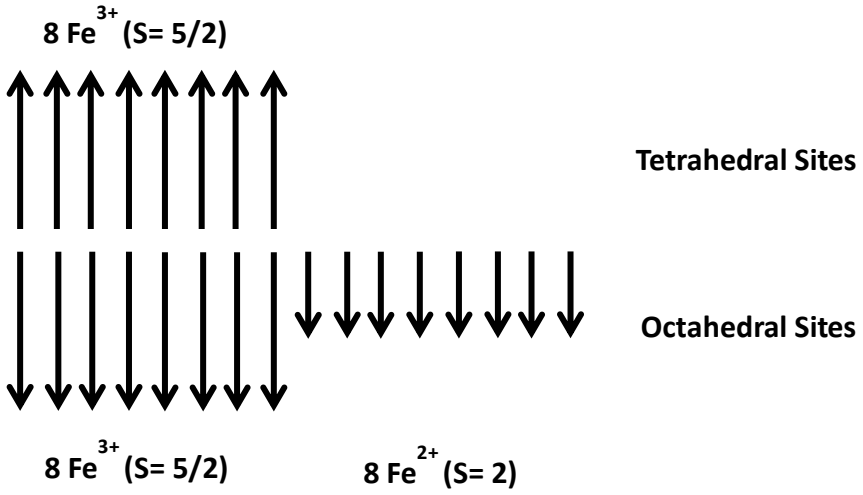

Figure 4: The unit cell of magnetite and its ferrimagnetic ordering of electron spins.

The magnetic properties of magnetite nanoparticles are mainly influenced by the nanoparticle dimensions. Nanoparticles below a size of 30 nm exhibit a superparamagnetic behavior (SP). In this case, magnetite nanoparticles have to be placed in an external magnetic field to exhibit measurable magnetic properties. Magnetite nanoparticles between 30 and 80 nm are called stable single domain (SSD). A ferrimagnet in which the magnetization does not shift across the magnet has the single domain behavior. Particles greater than ~80 nm are multi-domain (MD). In this case, several magnetic domains coexist

within a single particle, thereby reducing the net volume magnetization of the sample (Figure 5) (Faivre, 2016).

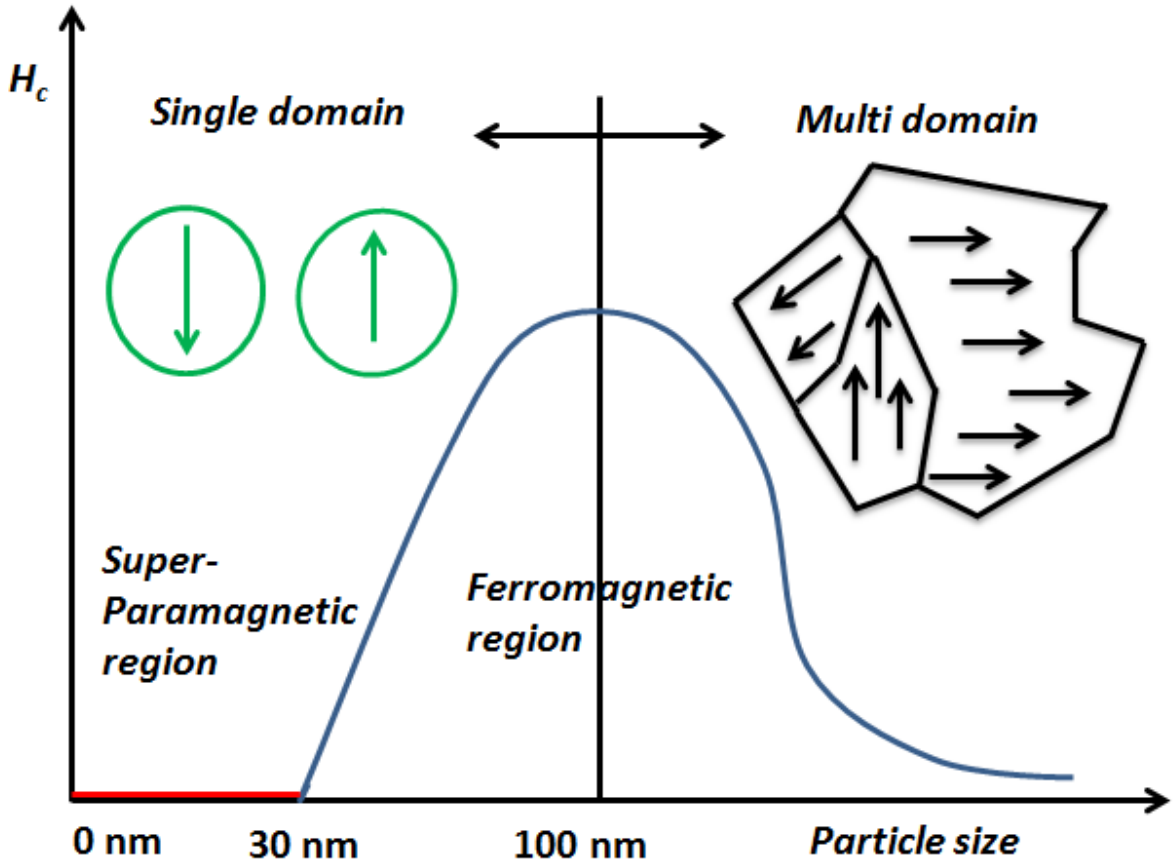

Figure 5: Sketch of the magnetic properties of magnetite nanoparticles as a function of nanoparticle size. X-axis: particle size, y-axis: coercivity (Hc).

Magnetite nanoparticles possess either ferrimagnetic or superparamagnetic behavior, strongly depending on particle morphology and size. Ferrimagnetic nanoparticles can either be single domain magnets or multi domain magnets. The dipoles within multi domain magnets show different orientations and therefore lowering the total dipole of the particles. Different particles show different hysteresis loop shapes (Figure 7). Superparamagnetic materials do not possess coercivity (H_c) and show no hysteresis loop. Conversely, stable single domain particles show a nicely shaped hysteresis loop through their coercivity (H_c). To gain this information, a sample is placed within an external homogenous magnetic field and gets magnetized. The sample and its inherent magnetic field vibrate. The magnetic flux

density changes in coils, which are placed around the sample. A current is induced, which is proportional to the particle's bulk magnetization. Hysteresis loops of the particles can be recorded and analyzed (Dunlop and Özdemir, 2001).

An external homogenous magnetic field is applied around a ferromagnet. Thus, the magnetization of the ferromagnet increases until its saturation. If the magnetic field is reduced to H = 0 ($A*m^{-1}$), the hysteresis curve does not follow the same route back (Figure 6). However, a remanent magnetization (MRS) remains, due to the fact that magnetic domains within the ferromagnet do not fully return to their disordered state. To demagnetize the ferromagnet, a reversed magnetic field has to be applied, which is known as coercivity (H_c). Hysteresis curves were recorded through varying the amplitude of the external magnetic field (Dunlop and Özdemir, 2001).

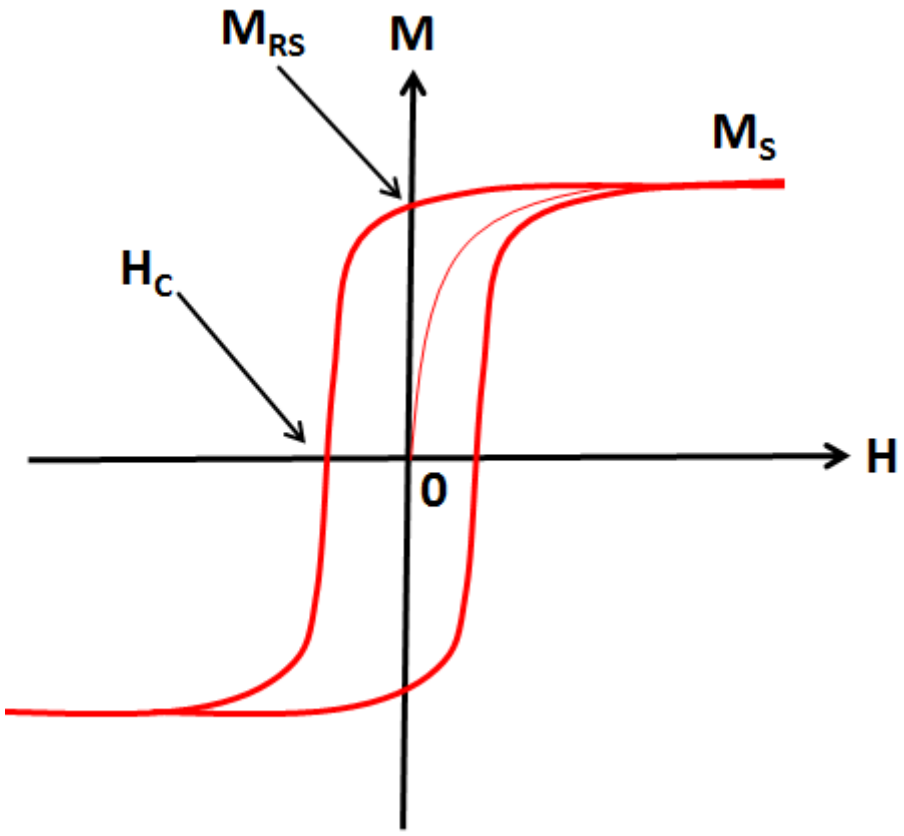

Figure 6: Hysteresis loop: A ferromagnet gets magnetized, starting at H=0, until its magnetization saturation (MS) is reached. If H is reduced to 0 A/m thereafter, the hysteresis curve does not follow the same route back and a remanent magnetization (MRS) remains. With an applied reversed magnetic field, known as coercivity (Hc), the ferromagnet can be demagnetized.

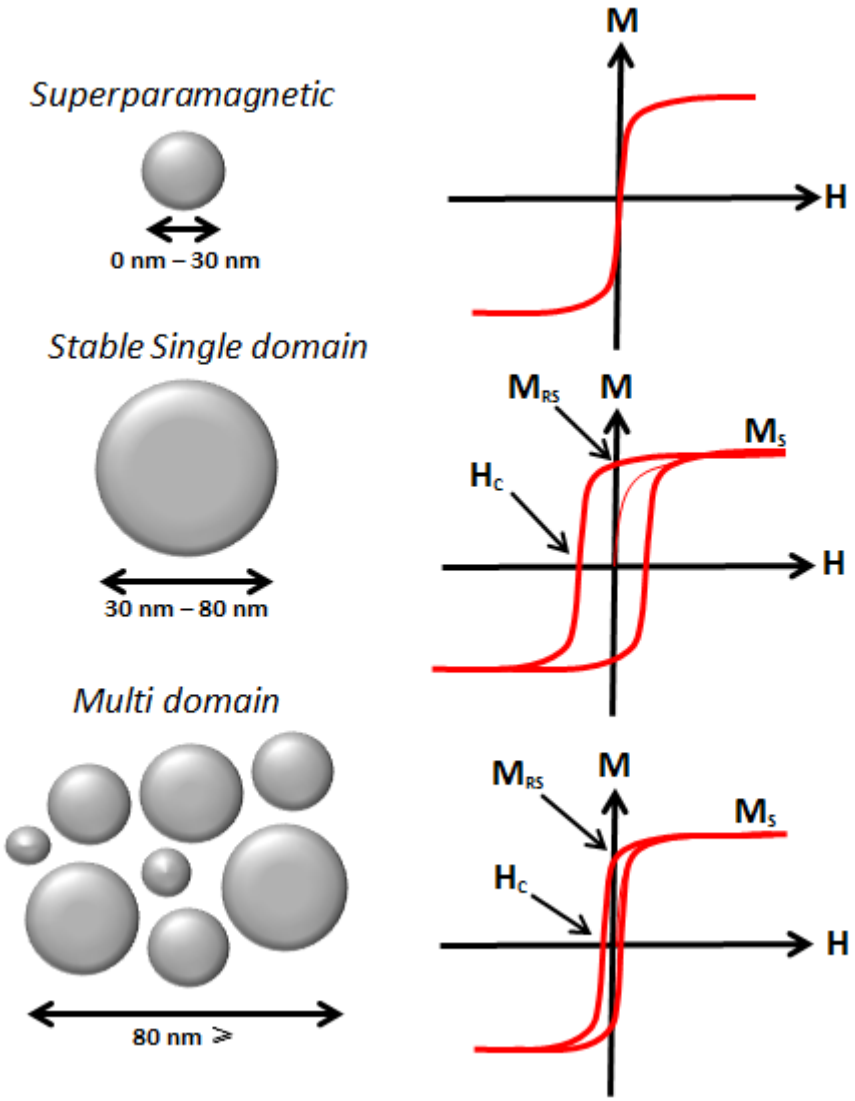

Figure 7: Hysteresis loops in comparison of different magnetic domains.

2.3.1 Experimental: Bulk Magnetic Characterization using a Vibrating Sample Magnetometer (VSM)

Nanoparticles were magnetically characterized using a Princeton Measurements Corporation (PCM) vibrating sample magnetometer (VSM) at room temperature. Particle samples were washed three times to minimize the concentration of impurities, e.g. precursor phases, after synthesis. The supernatant was removed and the pellet was resuspended in H_2O MilliQ. To avoid pH changes after synthesis, H_2O MilliQ was adjusted to a pH value of 11. Magnetic measurements were performed on the samples that were dried on a filter paper at ambient temperature under the hood. The sample powders were then immobilized by placing them into gently pressed gel caps. The magnetic properties of the samples were characterized at room-temperature hysteresis loops, which were measured between +1 and -1 T with 100 ms

averaging time to characterize the saturation magnetization (M_S), saturation remanent magnetization (M_{RS}) and coercivity (H_C) of the bulk sample. The hysteresis ratios, remanent to saturation magnetization (M_{RS}/M_S) and remanence coercivity (showing a slightly higher field to the opposite direction which is needed to demagnetize the sample), to coercivity (H_{CR}/H_C) reflect the composition, particle size and the chemical purity of the sample.

2.4 STRUCTURAL ANALYSIS

Nanoparticles of magnetite can grow to different sizes and have different morphologies due to environmental or synthetic conditions. In magnetite, the iron ions are distributed into the tetrahedral (Td) and octahedral (Oh) sites of the face centered cubic structure, stacking oxygen according to ($[Fe^{3+}]Td[Fe^{3++}Fe^{2+}]OhO^4$). Magnetite can easily oxidize to maghemite, which is its natural weathering product (Widdrat et al., 2014), (Schwertmann and Cornell, 2007). Maghemite is similar to magnetite in its crystallographic structure, in that it consists in the inverse spinel group with a cubic unit cell. The magnetite unit cell contains 32 cubic closely packed O^{2-} ions. One half of the octahedral positions are filled with eight Fe^{3+} ions and eight Fe^{2+} ions. Additionally, eight of the tetrahedral positions are filled with Fe^{3+} ions. Two different sublattices are formed regarding to the octahedrally and the tetrahedrally bound iron ions. Therefore, magnetite is a ferrimagnetic material (Cornell and Schwertmann, 2003). In case of maghemite, the unit cell consists of 21 1/3 Fe^{3+} ions and 32 O^{2-} ions and forms the same crystalline structure as magnetite with the exception of observed vacancies in the crystal lattice (ϒ–Fe_2O_3) ($[Fe^{3+}]Td[Fe^{3+5/3X1/3}]OhO^4$ (X stands for a cationic vacancy) (Jolivet et al., 2004). The two antiparallel sublattices of maghemite have a non-zero net magnetic moment, which leads to maghemite also being ferrimagnetic (Cornell and Schwertmann, 2003), (Schwertmann and Cornell, 2007), (Widdrat et al., 2014). Due to these similarities, magnetite and maghemite are hard to differentiate by analytical means: the lattice parameter for maghemite is e.g. 0.83419 nm, slightly reduced in comparison to that of magnetite, which is 0.83969 nm (Schwertmann and Cornell, 2007), (Widdrat et al., 2014). The reduction occurs due to the presence of the vacancies that replace the ferrous iron in the lattice. This difference enables the differentiation of these minerals only by high resolution techniques such as Wide Angle X-ray Scattering (WAXS), which is normally used for crystal lattice parameter and size determination (Faivre, 2016). Typically WAXS peaks for magnetite are shown in Figure 8 with an inset of the magnetite lattice.

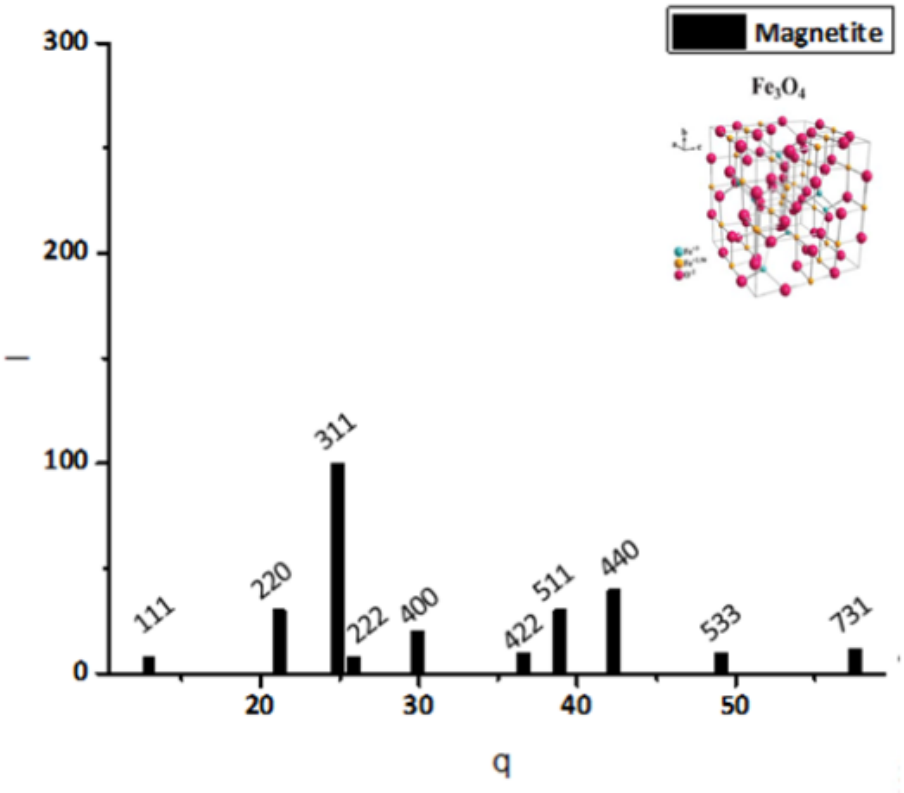

Figure 8: XRD peak positions of magnetite. The inset shows the magnetite unit cell.

2.4.1 Experimental: Wide Angle X-Ray Diffraction (WAXS)

Wide Angle X-ray Scattering (WAXS) measurements were performed at the µ-Spot beam line of the BESSY II synchrotron facility of the Helmholtz-Zentrum in Berlin, Germany. The energy was set up to 15 keV, which corresponds to a wavelength of λ = 0.82656 Å by a Si 111 monochromator. For measurements, a thin Kapton film (Breitlander GmbH, Hamm, Germany) was clamped on a special custom made sample holder (Schmitz, 2010). 10 µl of each sample solution were pipetted on the thin Kapton film, on which 54 samples can be placed within the sample holder. For lattice parameter determination, the samples were mixed with the internal α-quartz standard (standard Reference Material 1878a, NIST) prior to drying. After drying on the Kapton foil, the samples were measured with a 100 µm beam of the wavelength λ = 0.82656 nm. The diffraction data were acquired on a MarMosaic 225 detector (Mar USA, Evanston, USA), consisting of 9 independent CCD cameras. The detector resolution was 3072 x 3072 pixels, whereas the pixel size was 73.242 µm. For monitoring the x-ray diffraction XRD experiment, a Spec program (SPEC, 2010) was used, whereas exposure

times were varied between 5 s and 300 s, depending on the intensity of the signal. Each sample was measured three times. The sample to detector distance was set to 150 – 170 mm. DPDAK, a software for calculating the exact sample-to-detector distance, the instrumental peak broadening and the full width at half maximum (FWHM) was used. All three parameters were determined by fitting the (311)-peak with a pseudo-Voigt function (Eq. 7) and the crystallite size was determined with the Scherrer equation (Eq. 8) and the corrected FWHM (Faivre, 2016).

$$d_{hkl} = \frac{a}{\sqrt{h^2 + k^2 + l^2}} \qquad \textit{Eq. 7}$$

$$\frac{2\pi}{q} * \sqrt{11} \qquad \textit{Eq. 8}$$

2.5 THERMAL GRAVIMETRIC ANALYSIS (TGA)

The mass loss of a material can be measured using thermogravimetric analysis (TGA). The purity, composition, observed moisture contents, decomposition reactions and temperatures can be monitored with TGA. The sample is inserted into a furnace and its weight is monitored over time in order to get heated or cooled. Therefore the mass of the substance is monitored as a function of time or temperature. While heating a material, its weight can decrease or increase. A sample pan is used, which is supported by a precision balance. The dry sample is inserted in the pan, which is further placed within a furnace. During the experiment the pan gets heated or cooled and the mass is monitored. A purge gas controls the environment, which can be a reactive or inert gas and flows over the sample exiting through an exhaust (Vyazovkin, 2002). A schematic weight loss curve is shown in Figure 9.

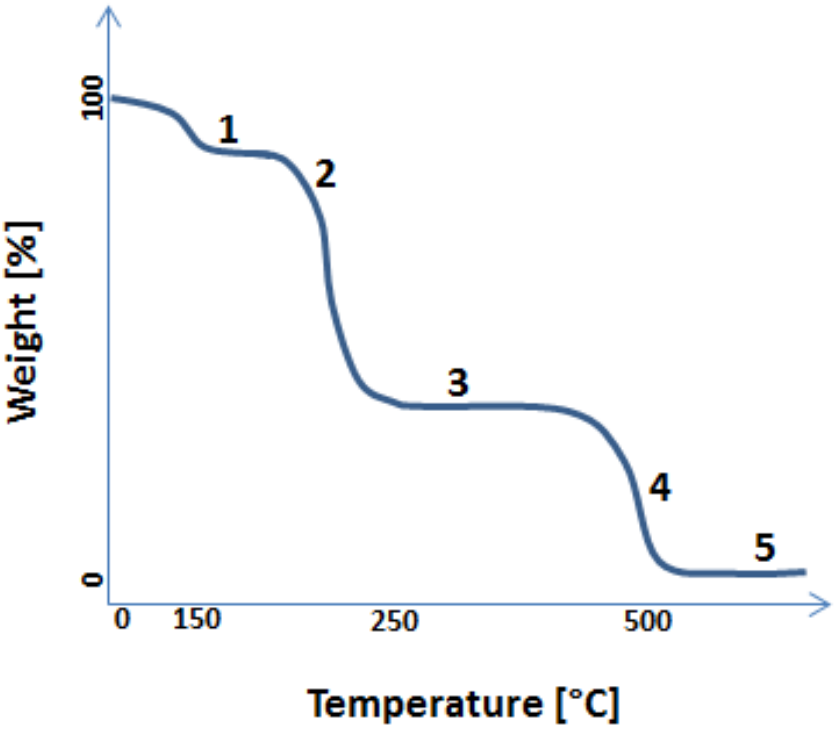

Figure 9: Typical schematic weight loss curve within a TGA experiment.

In Figure 9, a weight loss curve is shown which consist of several steps. In step 1, solvents, e.g. H_2O, get burned. Step 2 refers to decomposition of the materials. In step 3, the atmosphere switches from nitrogen to oxygen due to the burning process. In step 4, the composition of carbon is monitored and step 5 shows the inert inorganic residue of ash, fillers or gas products.

At lower or moderate temperatures around 150 °C the losses of composites, e.g. water, low molecular weight solvents, or gas desorption occurs (1). At temperatures between 150 °C and 250 °C, low molecular compounds such as additives get burned (2). Between 250 °C and 500 °C decomposition products occurs. Carbonization occurs at temperatures above 500 °C.

2.5.1 Experimental: TGA

TGA (SENSYS evo TGA-DSC, SETARAM Instrumentation, Caluire, France) was performed with approximately 1 mg of freeze-dried polyR-magnetite nanoparticle powder placed in an alumina crucible. Heat flow and weight loss were measured during programmed heating (25−500 °C at 2 °C/min) and nitrogen was used as the purge gas. Importantly, buoyancy

correction was made in order to subtract correctly the background and obtain quantitative data of heat flow and weight loss.

2.6 SMALL ANGLE NEUTRON SCATTERING (SANS)

Small-angle scattering (SAS) of x-rays (SAXS) and neutrons (SANS) describes the scattering of x-rays/neutrons by a sample which show structures within the nm-range (usually from 1 nm to 300 nm). X-rays are scattered by electrons and are therefore sensitive to the electron density distribution of a sample. Neutrons, on the other hand, interact mainly with the nuclei, so that they are sensitive to a sample's atomic and isotopic composition. In contrast to other high-resolution methods like HRTEM, SAS is non-destructive and can be carried out under physiological conditions (Dmitri and Michel, 2003), (Hollamby, 2013).

2.6.1. SCATTERING GEOMETRY AND SCATTERING INTENSITY

A typical SAS experiment is schematically illustrated in Figure 10. The sample is illuminated with a beam of defined direction and wavelength λ. These two characteristics define the wave vector $\vec{k_i}$ of the incident beam, with magnitude $k_i = \left|\vec{k_i}\right| = 2\pi/\lambda$. For neutrons: In a monochromatic configuration λ is set by 7 Å, while in a time-of-flight configuration λ is set by 1.75 – 16.5 Å. When the beam interacts with the sample, heterogeneities in the electron (x-ray) or atom (neutron) distributions within the sample give rise to scattered waves departing at various directions with respect to the incident beam (Roe, 2000), (Svergun and Koch, 2003), (Das and Doniach, 2008). The scattered waves are characterized by their wave vectors $\vec{k_s}$. We only consider elastic scattering, for which $k_s = k_i = 2\pi/\lambda$. Moreover, for isotropically structured samples like liquids or powders, the only relevant parameter characterizing the scattering process is the scattering angle, termed as "2θ" (Figure 10). In this case the scattering vector $\vec{q} = \vec{k_s} - \vec{k_i}$ has the magnitude $q = \left|\vec{q}\right| = \left|\vec{k_s} - \vec{k_i}\right| = \frac{4\pi}{\lambda}\sin\theta$. $I(q)$, is the scattered intensity as a function of this magnitude q. This is convenient, because each q-value, which defines a distance in reciprocal space, has its corresponding length scale $d = 2\pi/q$ in the real space. In other words, the q-dependent scattering intensity $I(q)$ describes a sample's degree of heterogeneity (in terms of electronic or atomic distributions, for x-rays and neutrons, respectively) on the length scales d that correspond to the probed

q-range. For example, for a sample that exhibits periodic density oscillations with period D, I(q) shows a sharp peak $q = 2\pi/D$. Such peaks arising from periodic structures are called Bragg peaks (Egami and Billinge, 2003). The structure of non-periodic samples can be reconstructed from measured curves I(q) as well.

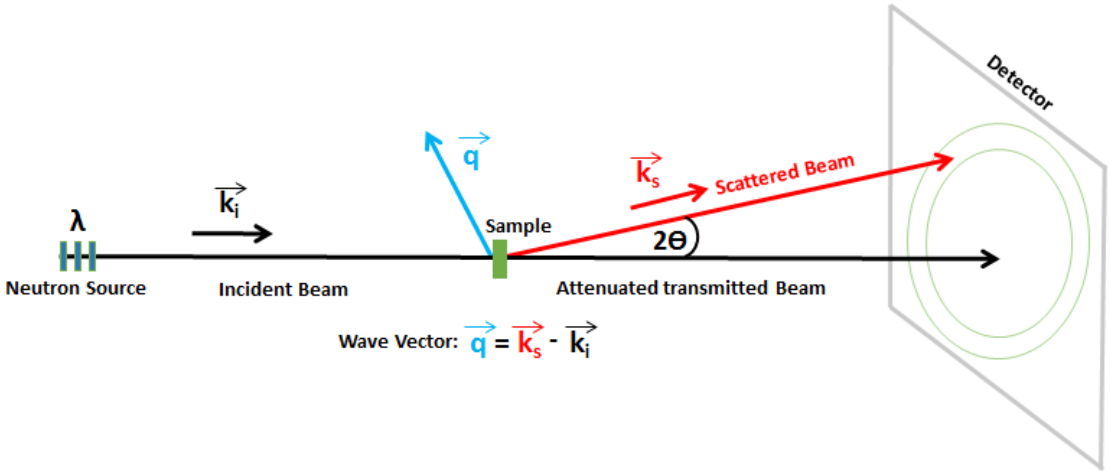

Figure 10: Scheme of the principle of Small Angle Neutron Scattering.

2.6.2 Model-Free Analysis of SANS Data

Within the application range of Porod's law small angle scattering intensities can be described as power laws in *q*, wherein exponents are related to the shapes of objects on the probed length scales corresponding to q:

$$I(q) \propto q^{-m} \qquad \textit{Eq. 9}$$

In the usual double-logarithmic representation of I(q), the exponent *m* manifests itself as the slope of the curve. A Porod slope *m* = 4 corresponds to round particles with smooth and sharp surfaces. A Porod slope *m* = 1 represents a cylinder and *m* = 2 represents disk-like particles (Figure 11).

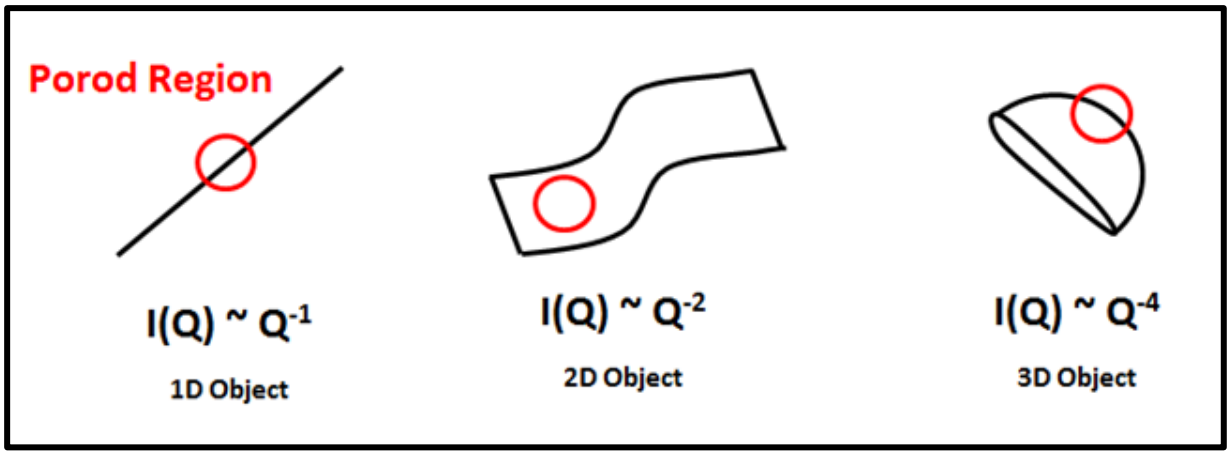

Figure 11: Scheme of Porod regions.

2.6.3 Contrast Variation in SANS

As described above neutrons are scattered by heterogeneities in the isotopic composition of a sample. On the length scale probed by SANS, which is larger than the individual atoms, a sample's local isotopic composition can be described in terms of the scattering length density (SLD) ρ:

$$\rho = \frac{\sum_i n_i b_i}{v}, \qquad \textit{Eq. 10}$$

where v is the size of the considered volume element, n_i is the number of isotopes of type i in that volume element and b_i is the characteristic coherent scattering length of isotope i. Importantly, protons and deuterons, the nuclei of light and heavy hydrogen atoms, ^{1}H and ^{2}H (deuterium, D) respectively, exhibit very different values of b (Table 1). This phenomenon can be exploited for the study of structures in an aqueous medium, where the latter can be prepared from H_2O, from D_2O, or from H_2O/D_2O mixtures, in order to highlight certain structures or to render them invisible. According to Eq. 11, magnetite (Fe_3O_4) has an SLD of $\rho_{Fe3O4} \approx 7.0 \times 10^{-6}$ Å^{-2} (Table 2). The scattering contrast of ordinary Fe_3O_4 is thus weak in a D_2O-based medium which has similar SLD ($\rho_{D2O} \approx 6.4 \times 10^{-6}$ Å^{-2}) but very strong in a H_2O-based medium of very different SLD ($\rho_{H2O} \approx -0.56 \times 10^{-6}$ Å^{-2}). Similarly, also the isotopes of other elements, notably of Fe in the context of the present work, have significantly different scattering lengths (Table 2). $\rho_{57Fe3O4}$ (Table 2) differs from ρ_{Fe3O4} and can be matched out in a suitable H_2O/D_2O mixture according to Eq. 11. x corresponds to the percentage of D_2O

which has to be added to its counterpart H_2O to guarantee an invisible rendering of $^{57}Fe_3O_4$, when measuring $^{57}Fe_3O_4$ in this match point solution.

$$\rho_{57Fe3O4} = x * \rho_{D2O} + (1 - x) * \rho_{H2O} \qquad \textit{Eq. 11}$$

A scheme of core-shell particles is shown in Figure 12a. Figure 12b shows matched cores of the core-shell particles measured for which in a certain H_2O/D_2O mixture the core is matched out due to the same SLD of the H_2O/D_2O mixture and the core. *Vice versa*, Figure 12c shows matched shells of the core-shell particles measured for which in a certain H_2O/D_2O mixture the shell is matched out due to the same SLD of the H_2O/D_2O mixture and the shell. Therefore, different parts of particles, e.g. organic shells and inorganic cores, can be alternate measured (Jackson, 2008).

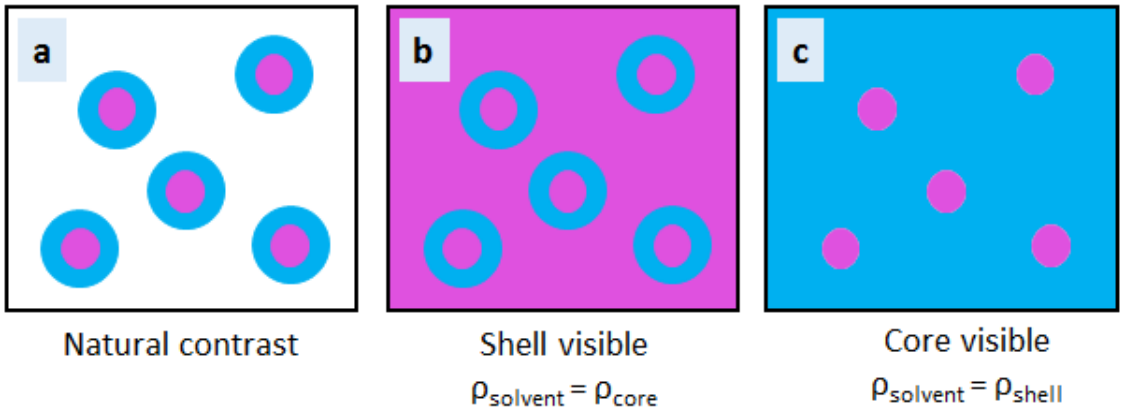

Figure 12: Scheme of the contrast variation effect on the measurable structure of a core-shell particle.

The match point of a specimen is defined using H_2O/D_2O mixtures in which the specimen is completely invisible in SANS measurements. One can either invisible render the organic or the inorganic part of a sample. As magnetite has a higher SLD than D_2O (Table 2), it is impossible to completely render magnetite. Thus, a Fe isotope has to be used for the polyR-magnetite nanoparticle synthesis to get an overall lower SLD for Fe_3O_4. ^{57}Fe was used during co-precipitation and the synthesis of $^{57}Fe_3O_4$ nanoparticles is described in chapter 2.1.6. Then, polyR-^{57}magnetite nanoparticles can be matched within a certain solvent ratio of D_2O: H_2O of 67,3 %: 32,7% according to Eq. 11.

Table 1: Scattering lengths of different atoms.

Atom	***H***	***^{2}H***	***O***	***^{56}Fe***	***^{57}Fe***
b [fm]	-3,739	6,671	5,803	9,45	2,3

Table 2: Molecular volumes, scattering lengths and corresponding scattering length densities of used samples.

Molecule	***V [cm^3]***	***b [fm]***	***ρ [A^2]***
H_2O			$-0{,}56052*10^{6}$
D_2O			$6{,}3351*10^{6}$
$^{56}Fe_3O_4$	$73{,}8*10^{-24}$	51,5	$6{,}987*10^{6}$
$^{57}Fe_3O_4$	$73{,}8*10^{-24}$	30,112	$4{,}08*10^{6}$

An additionally match point can be calculated to match out the organic part in a sample. The polyR of the polyR-magnetite nanoparticles can be matched within a certain contrast variation of the solvents in a ratio of D_2O: H_2O of 37.69 %: 62.31 % according to Eq. 11.

PolyR-magnetite nanoparticles were measured in H_2O and D_2O/H_2O match point solutions for polyR, whereas polyR-^{57}magnetite nanoparticles and pure ^{57}magnetite nanoparticles were measured in the match point solution of $^{57}Fe_3O_4$.

2.6.4 EXPERIMENTAL

SANS measurements were carried out at the KWS-1 diffractometer of JCNS outstation at the FMR II reactor in Garching, Germany. A monochromatic setup with lambda = 0.7 nm (and $\Delta\lambda/\lambda$ = 10 %) is applied. The KWS-1 experiment was performed using three configurations of 2 m, 8 m and 20 m sample to detector distances and corresponding collimation length of 8 m and 20 m. Wide angles and therefore large q ranges with low resolution are covered, using small sample to detector distances, whereas narrow angles and therefore small q ranges with high resolution are covered, using large sample to detector distances. The measurements covered a q-range of 0.02 to 3.5 nm^{-1}. The detector is a two-dimensional area sensitive detector. 350 µl of each sample solution was filled in quartz cuvettes and a

rotational sample holder was used to avoid any sedimentation of especially highly concentrated samples. The software QtiKWS (Pipich, 2013) was used for data reduction.

2.7 USING MAGNETITE NANOPARTICLES IN MEDICINE

Iron oxide nanoparticles exhibit interesting features for different applications in medicine. They are able to establish a locally perturbing dipolar field in the presence of a magnetic field, if they are exposed to an alternating magnetic field, they can generate thermal energy and they are easily manipulated by an external magnetic field gradient, whereas they experience a magnetic force, which results in magnetophoretic mobility. Iron oxide nanoparticles are widely used in diagnostics and therapy. There are some ongoing preclinical and clinical trials, including magnet resonance imaging (MRI) (Bourrinet et al., 2006), (Kooi et al., 2003), image-guided therapy (Susil et al., 2003), and hyperthermia (Wust et al., 2002), amongst others. New methods in drug targeting were introduced, which include new drug-loading strategies of magnetic drug carriers, drug release from magnetic nanosystems and hyperthermia. In this thesis the focus lies on iron oxide nanoparticles as suitable candidates for hyperthermia and novel MRI contrast agents. To create a nice nanoparticle system in the field of biomedicine, many factors have to be considered: size, monodispersity, shape, composition, colloidal stability, oxidation state, magnetic behavior, biocompatibility and cellular uptake among others (Ito et al., 2005; McBain et al., 2008), (Shimizu et al., 2007). Nanoparticle sizes should be located in the range between 20 and 50 nm for hyperthermia and below 10 nm for MRI contrast agents (Gazeau et al., 2008).

2.7.1 BIOCOMPATIBILITY OF MAGNETIC NANOPARTICLES

If nanoparticles are intended for use in biomedical applications, their biocompatibility with living cells has to be tested and evaluated to exclude potential toxicity (Black, 2005). Several toxicity tests for nanoparticles are available and some of them were used in this thesis to proof the biocompatibility of the polyR-magnetite nanoparticle system. Three biocompatibility assays were compared to investigate the viability of cells after treatment with nanoparticles (Matuszak et al., 2016). The continuous real-time monitoring with xCELLigence system was used, in order to determine cell indices, which reflected cell viability in real-time (Ke et al., 2011). In parallel with that, life imaging of cells, incubated with nanoparticles, was monitored. As a comparison to these two static methods, a dynamic flow

experiment was performed to evaluate the potential nanoparticle toxicity under flow conditions (Cicha et al., 2009). In the real-time monitoring, the cell index, which is a dimensionless parameter, is calculated through the relative change in the measured electrical impedance, which is a function of the cell viability, number, morphology, and adhesion strength (Matuszak et al., 2016). If no cell adheres to the electrode, the cell index is zero. If cells attached to the electrodes, the local ionic environment at the electrode/solution interface is affected and the electrode impedance increases, which is displayed as cell index values. The cell index is thus a quantitative measure of adherent cells due to the attachment of those cells on the electrodes. The cell interaction`s quality with the electrodes is additionally measured, e.g. increased cell spreading or adhesion strength. To evaluate effects of nanoparticles on HUVECs viability , parallel to real-time cell analysis, live-cell microscopy was performed in order to directly monitor morphological changes of the cells (Matuszak et al., 2016). As a comparison to the static cell viability experiments, dynamic flow experiments for evaluating the cell viability were also performed (Cicha et al., 2009).

2.7.1.1 EXPERIMENTAL: REAL-TIME CELL ANALYSIS

Real-time cell analysis experiments were performed using the xCELLigence system (RTCA DP Analyzer, Roche Diagnostics, Mannheim, Germany) was used. All media and cell culture reagents were purchased from Promo Cell (Heidelberg, Germany), Accutase™ was purchased from PAA Laboratories (Linz, Austria) and dispase from Life Technologies GmbH (Darmstadt, Germany). Human umbilical vein endothelial cells (HUVECs) were isolated from freshly collected umbilical cords kindly provided by the Department of Gynecology at the University Hospital Erlangen. HUVECs at passage 1 were used for all experiments. The experiments were performed in 16-well E-plates (ACEA Bioscience, CA, USA), in which the impedance was measured with the help of microelectrodes localized at the bottom of the wells. Background measurements were performed while adding 100 µl of sterile endothelial cell growth medium within the wells. Then, 50 µl of the previously prepared cell suspension was added by replacing 50 µl of the already added media. The cells were added at a concentration of $1x10^3$ at 30 minutes after start of the assay and the impedance was monitored using the xCELLigence system. The effects of polyR-magnetite nanoparticles on HUVEC viability were monitored. For this purpose, 100 µl of additional media, with or without particles were added after the first 24 hours of cell growth. Different controls and different nanoparticle

concentrations were added. Final nanoparticle concentrations of 0, 12.5, 25, 50, 100, 200 and 400 µg/ml were chosen. The cell growth was monitored every 10 minutes for 96 hours on hexaplicate samples.

2.7.1.2 EXPERIMENTAL: LIVE-CELL MICROSCOPY

HUVECs were seeded at a concentration of $1x10^3$ cells per well in 96-well plates in 100 µl medium each. 24 hours after seeding, 100 µl of medium with or without nanoparticles were added to the wells to the final concentrations of 0, 12.5, 25, 50, 100, 200 and 400 µg/ml. The cell growth was monitored with a live cell-imager (IncuCyte FLR microscope system, Essen Bioscience, MI, USA) for 96h hours. The same as above, the experiments were performed in hexaplicates (Matuszak et al., 2016).

2.7.1.3 EXPERIMENTAL: FLOW EXPERIMENTS WITH BIFURCATION MODEL

Bifurcation flow-through cell culture slides (y-shaped µ-slides, Ibidi®, Munich, Germany) were used for direct microscopic studies. Numerical flow simulations identified distinct regions of shear stress: The laminar shear stress region (10.2-10.8 dyne/cm^2 at a flow rate of 9.6 mL/min) throughout the straight main channel and the region of non-uniform shear stress at the outer walls of bifurcation (shear stress range from ~6.3 dyne/cm^2 to ~0.5 dyne/cm^2) (Cicha, 2016). HUVECs were seeded at a concentration of $7x10^5$/mL within the bifurcating slides and grown until confluence. After a cell monolayer grew within the slides, the cells were perfused using a programmed peristaltic pump (Ismatec, Wertheim, Germany). The slide channel was perfused with medium (with or without nanoparticles) at arterial shear stress for 18h. Two different nanoparticle concentrations (100 µg/ml and 400 µg/ml) of polyR-magnetite nanoparticles were used for the experiment. The slides were detached from the peristaltic pump system after 18 h and were washed with PBS buffer. Later on, they were fixed with 4 % formalin for 10 min at RT and the HUVECs cytoskeleton was stained using an Alexa488-phalloidin (PromoKine, Heidelberg, Germany). For cell nuclei counterstaining, a DAPI (Molecular Probes, Darmstadt, Germany) was used.

2.7.2 MAGNETIC RESONANCE IMAGING (MRI)

Compared to x-ray imaging, MRI can visualize soft tissue without any invasive or ionizing side effect. It provides atomically and functional images without any depth limitation in the organism and with a high spatial resolution. MRI contrast agents are used to further improve the contrast, e.g. to improve detection of pathologies. The mechanism of MRI contrast agents comprises their shortening of proton relaxation times through the magnetic interaction with their neighboring protons in the tissue and the following exchange with the bulk water, which propagates and amplifies the contrast effect. Generally speaking, the MRI signal is proportional to the local proton density and well-disposed by functions of transverse (T2) and longitudinal (T1) relaxation times of the tissue. The proton relaxation is speed up by contrast agents (Eq. 12).

$$Ri = Ri0 + ri[CA] \qquad \textit{Eq. 12}$$

Ri = 1/T1 and 1/T2 are relaxation rates which are observed in the presence of a contrast agent, Ri0 is the base line tissue relaxation rate, ri is the contrast agent relaxivity and [CA] is the contrast agent concentration. The relation applies to both, transverse, T2 and longitudinal T1, relaxation mechanisms. The signal, which is measured in the magnet resonance, is a nonlinear complex function of the contrast agent concentration. There are two types of contrast agents, whereas T1 weighted contrast agents exhibit positively contrast, resulting in bright signals. T2 weighted contrast agents show negative contrast, resulting in dark signals. T1 contrast is preferred to T2 contrast, due to better clarity, through their dark signal. T2 contrast agents may cause confusion with endogenous artifacts, fat, hemorrhage, blood clots or air. Still, both, negative and positive contrast agents are important to complement the information in MRI (Merbach and Tóth, 2001). Iron oxide nanoparticles are T2 weighted contrast agents. Gadolinium chelates are paramagnetic contrast agents mainly affects T1, which results in R2/R1 ratios close to 1 (Caravan et al., 1999). For tissues the ratio is $R_1 < R_2$ and a positive contrast is provided on T1 weighted images. Superparamagnetic iron oxide nanoparticles mainly affect T2, which results in higher R_2/R_1 ratios (Na et al., 2009). This leads to a higher effect and a negative contrast on T2 weighted images. In order to characterize the performance of a contrast agent, the relaxivity R2/R1 rates are analyzed (Faivre, 2016; Lee et al., 2015).

2.7.2.1 EXPERIMENTAL: MAGNET RESONANCE IMAGING AND CORRESPONDING RELAXIVITIES

A Bruker mq 40 contrast agent analyzer (0.94 T at 40 MHz) was used to measure T1 and T2 relaxation times at 39°C of aqueous dispersions of polyR-magnetite nanoparticles. The relaxation R1 and R2 [l/(mmol*s)] was determined using a linear relationship of the iron concentration c(Fe) in [mM] and the reciprocal of the relaxation time $1/T_{1,2}$ in [s^{-1}] Thus, the relaxivity $R_{1,2}$ was calculated via the slope of the obtained linear equation.

2.7.3 MAGNETIC HYPERTHERMIA

If diagnostic imaging presents a certain disease, the disease is usually treated with various types of therapeutics such as chemotherapy (Skeel and Khleif, 2011). Nonspecific drug molecules lead to tissue distribution with metabolic instability causing whole body toxicity and lower the therapeutic effect. An excellent alternative exists, which is known as magnetic hyperthermia, which is a selective, minimal cell damaging cancer therapy option (Dutz and Hergt, 2014), (Baronzio and Hager, 2008). When applying magnetic fields to injected magnetic nanoparticles, the reorientation of their magnetic moments can produced energy in terms of heat. As iron oxide nanoparticles are biocompatible, biodegradable and exhibit magnetic properties, they are the main candidates for thermotherapies. In magnetic hyperthermia, the specific loss power (SLP), or the specific absorption rates (SAR) describes the heat absorption, which is usually given in watt per gram units (W/g), whereas the mass density of the nanoparticles is considered (Eq. 13). The SLP is described as a temperature increase with time (dT/dt) (Kolhatkar et al., 2013).

$$SLP = \frac{CV}{m}\frac{dT}{dt} \qquad \textit{Eq. 13}$$

C is the specific heat capacity of the medium and m is the mass of the magnetic particles. SLP values are used to compare heating capacities of different magnetic materials. Novel nanomaterials are designed to increase a good hyperthermia performance. Magnetic materials magnetization orient preferentially along one or several axes, in which the magnetic energy is minimal (Hergt et al., 2006). This so-called magnetic anisotropy energy depends on the symmetry of the crystal structure and the shape of nanoparticles. SLPs are influenced by different properties of nanoparticles (see chapter 2.7.1), such as modifying geometry, composition, and magnetic anisotropy modification. A typical range of the SLP is

located between 100 to 200 W/g. The complexity of the biological environment highly influence the SLP values and the hyperthermia performance (Faivre, 2016). There are two delivery routes to the tumor, the intratumoral and intravenous injections, depending on the tumor type. Intratumoral injections are performed in solid tumors, whereas intravenous injections are used for primary tumors and metastasis. Several clinical trials are ongoing and large amounts of particles are required to reach cytolytic tumor temperature because of their poor heating efficacy (low SLP). In intravenous injections, the amount of delivered particles is very low (Faivre, 2016), (Dutz and Hergt, 2014), (Matus et al., 2016), (Laurent et al., 2011; Lee et al., 2015).

2.7.3.1 EXPERIMENTAL: HYPERTHERMIA

Magnetic properties of liquid samples were determined by mean of vibrating sample magnetometry (VSM; micromag 3900, Princeton Measurements, Princeton, USA). The heating performance of liquid samples was measured within a magnetic field calorimeter. In short, the magnetic nanoparticle samples are placed in a solenoid generating an alternating magnetic field of about 410 kHz and field amplitude of 25 kA/m. The resulting temperature increase of the sample due to the magnetization reversal losses is measured as function of heating time by a fiberoptic temperature sensor. Taking into account the particles concentration of the sample, the specific heating power of the particles is calculated from the recorded heating curves.

2.8 BIOCONJUGATION OF MAGNETITE NANOPARTICLES

New and interesting properties can be created when synthesizing nanoparticle assemblies exhibiting multifunctionalities. Many biomimetic materials were introduced recently, such as bacteria, peptides (Baumgartner et al., 2012), DNA (Byrom et al., 2014), proteins (Kurppa et al., 2007) or viruses (Olszewska, 2015), which were used for mineralization templates for a variety of nanoparticles (Fratzl and Weiner, 2010), (Paris et al., 2010). Hybrid structures of these organic templates and the inorganic nanostructures were assembled. A biological template is able to not only interact with one inorganic species, but also with many simultaneously (Huggins et al., 2014). In recent work, magnetosome chains of magnetotactic bacteria work as role models for nano-assemblies (Komeili et al., 2006). MamK is a magnetosome specific protein, which forms semi-flexible filaments (Kiani et al., 2015) within

magnetotactic bacteria. Its task is to stabilize chains of magnetite nanoparticles produced within the cell body (Carillo et al., 2013). It was shown that MamK forms filaments in *E.coli* and other host organisms (Pradel et al., 2006). MamK is a promising template for an anisotropic reconstruction of an artificial magnetosome chain. As solely magnetite nanoparticle chains tend to form rings, MamK acts for stabilizing anisotropic structures with its mechanical support (Kiani et al., 2015). Furthermore, it was shown that synthetic nanoparticle chains showed a better performance in biomedical applications, e.g. hyperthermia, than single nanoparticles (Alphandery et al., 2011). It was reported recently, that antibody-conjugated magneto-liposomes showed a good performance in tumor treatment (Gazeau et al., 2008). To conjugate nanoparticles to filamentous templates, they need certain functionalities for proper binding. Preferably, antibodies are used for decorating inorganic nanoparticles. In many cases, inorganic nanoparticles were synthesized in the presence of organic additives and therefore, consist of organic layers, such as core-shell or mesocrystal structures, which act as binding blocks between the inorganic nanoparticle and the antibody. Antibodies can bind to biological templates and guarantee a strong fixation between the biological template and the inorganic nanoparticle. Click chemistry is frequently used in antibody-and bio-conjugation techniques. 1-Ethyl-3-(3-dimethylaminopropyl)carbodiimid (EDC) -N-Hydroxysuccinimid (NHS) coupling is often used as a click chemistry method for binding molecules of interest on target structures (Hermanson, 2013a). The EDC/NHS reaction is the most frequently used crosslinking strategy, which was reported in recent years and a variety of bio-conjugation on nanoparticles was performed (Figure 13). Peptide-functionalized gold nanoparticles (Bartczak and Kanaras, 2011), fluorescent magnetic nanoparticles (Weissleder et al., 2005), bovine serum albumin conjugated superparamagnetic iron oxide nanoparticles for cell studies (Mikhaylova et al., 2004), functionalized magnetite nanoparticles with proteins for nucleus-targeting in diagnostics and therapeutics (Xu et al., 2008), and zwitterionic modification of magnetite nanoparticles using EDC/NHS for blood pool contrast agents (Xiao et al., 2012) were reported. The EDC NHS coupling is a carboxyl to amine cross linking reaction (Zhang et al., 2002). EDC reacts with the carboxylic acid group of the target structure and forms an intermediate. This intermediate is displaced from primary amino groups, which occurs within a nucleophilic attack. The primary amine forms bonds with the carboxyl groups and the EDC is released as a by-product. The reaction is carried out at best

at an acidic pH, which is in the most case impossible due to physiological conditions, e.g. binding of antibodies, or other biological molecules. Therefore, NHS is used to improve the efficiency. The EDC couples the NHS to the carboxylic groups and NHS esters are formed. They exhibit more stable intermediates and for that reason it is possible to conjugate the carboxylic groups to primary amines under physiological pH.

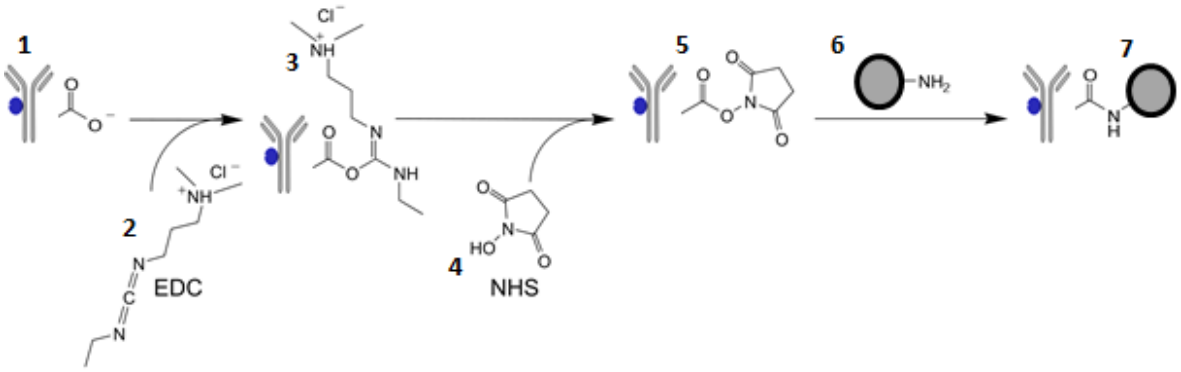

Figure 13: 1-Ethyl-3-(3-dimethylaminopropyl) carbodiimide (EDC) -N-Hydroxysuccinimide (NHS) coupling: (1) The carboxyl groups of antibodies are cross-linked with (2) EDC to form an (3) intermediate through a nucleophilic attack and primary amines from bonds with carboxyl groups. The efficiency is improved when adding (4) NHS to the reaction. The EDC couple the NHS to carboxylic groups and a (5) NHS ester is formed. (6) The conjugation to primary amines of the additives of the (7) magnetite nanoparticles at physiological conditions is possible.

2.8.1 Experimental: PolyR-magnetite nanoparticle antibody-conjugation

Chain structures of polyR-magnetite nanoparticles were conjugated with either anti-mCherry antibodies (+ Alexa Fluor® 488 dye), purchased from Novus Biologicals, or Immunogold (40 nm) conjugate monoclonal anti-His6-Tag antibodies, purchased from British Biocell International. Therefore a reaction was performed whereas 1-Ethyl-3-(3-dimethylaminopropyl) carbodiimide hydrochloride (EDC) and N-Hydroxysuccinimide (NHS), purchased from Sigma Aldrich, were used. First, 45 µl of the antibody in solution was mixed with 10 µl of an EDC (100 mM)/NHS (5mM) solution and afterwards 45 µl of polyR-magnetite nanoparticle solution (1.39 mg - 6.95 mg) was added. The total volume of the reaction was

100 µl and incubation times between 1 to 2 h were chosen. Afterwards, the samples were washed using a magnet to separate antibody decorated magnetite nanoparticles from unbound antibodies (Jehle et al., 2016).

2.8.2 EXPERIMENTAL: PROTEIN FILAMENT DECORATION WITH ANTIBODY COATED MAGNETITE NANOPARTICLES

MamK_mCherry_His_6 filaments (Carillo, 2014) were incubated with beforehand anti-mCherry antibody conjugated polyR-magnetite nanoparticle chain structures. Therefore MamK_mCherry_His_6 filaments were incubated with 10 µL of anti-mCherry antibody conjugated polyR-magnetite nanoparticles, for 10 min at RT (Jehle et al., 2016). A magnet was used to remove the largest aggregated while the supernatant was collected and mixed with 20 µL H_2O MilliQ. The procedure was repeated and 10 µL of the supernatant were dropped on a Petri dish (µ-Dish35mm, high glass bottom, Ibidi®) for further analysis (chapter 2.8.3).

2.8.3 EXPERIMENTAL: FLUORESCENCE MICROSCOPY WITHIN AN APPLIED MAGNETIC FIELD

PolyR-magnetite nanoparticle chains bound to MamK_mCherry_His_6 filaments were imaged by fluorescence microscopy. The excitation was chosen at 565 nm (pE-100, CoolLED), a 60 x water immersion objective was applied (NA1.2, Nikon) and the emission was recorded through a longpass filter (600nm) using a sCMOS camera (2560x2160 pixels, Neo sCMOS, Andor). The images consisted of 1280x1080 square pixels of 140 nm in sizes. Either a rotating field (~ 3.5 mT) was applied for solely fluorescent particle imaging, or a magnet was placed, in order to activate the particles bound to the filaments, in the sample position and an image was recorded. The magnet was then moved around the sample area by 90 degree and a second image was recorded.

3. Results & Discussion

3.1 PolyR-magnetite nanoparticle: structure, magnetic properties and formation mechanism

3.1.1 Syntheses of magnetite nanoparticles in the presence of additives

Co-precipitation was performed to synthesize magnetite nanoparticles in the presence of polyR as well as without as a control. Photographs of the respective particle solutions are shown in Figure 14. The inset in Figure 14a shows a photograph of an aggregated particle solution, which was precipitated in the absence of additives. In particular, the sedimented black compounds are observable at the bottom of the flask. The inset in Figure 14b shows a photograph of a colloidally stable solution, which was precipitated in the presence of polyR. No aggregation or sedimentation occurs and the solution remains stable at RT over more than 1 year. Corresponding TEM images are shown for particles without additives (Figure 14a) and with polyR (Figure 14b).

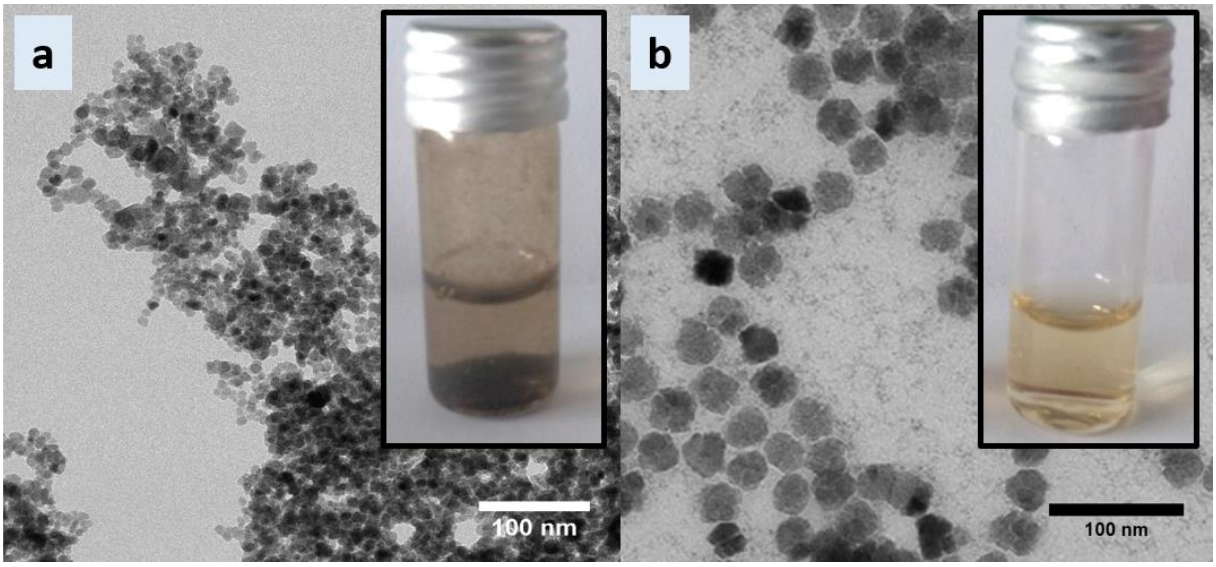

Figure 14: (a) Magnetite nanoparticles after 1 h synthesis without using additives. The inset in a shows a picture of a non-colloidal magnetite nanoparticle solution with sediment particles. (b) PolyR-magnetite nanoparticle solution after 1 h of synthesis. The inset in b shows a picture of a colloidal stable polyR-magnetite nanoparticle solution.

Magnetite nanoparticles, which were precipitated in the absence of any additive, have a broad spectrum of sizes and morphologies when deposited on TEM grids (Figure 14a) (Baumgartner et al., 2013a), (Baumgartner et al., 2013b). In comparison, polyR-magnetite nanoparticles show high monodispersity and are larger in size when deposited on TEM grids (Figure 14b, Figure 15). PolyR-magnetite nanoparticles are observed in TEM studies after the first 20 min of co-precipitation (Figure 15a). They exhibit “flower-like” structures and it seems that each particle consist of several smaller entities (Figure 14b, Figure 15a, b). Additionally, very tiny nanoparticles appear on the grid, which are most probably precursor nanoparticles. The formed polyR-magnetite nanoparticles occur in two-dimensional clusters or self-organize into chains when deposited on TEM grids (Figure 15b, c). It is possible to align these chain structures using a strong permanent magnet and visualize them in TEM (Figure 15d). The particle chains observed in TEM measurements increase in length over time but they also form closed-ring structures.

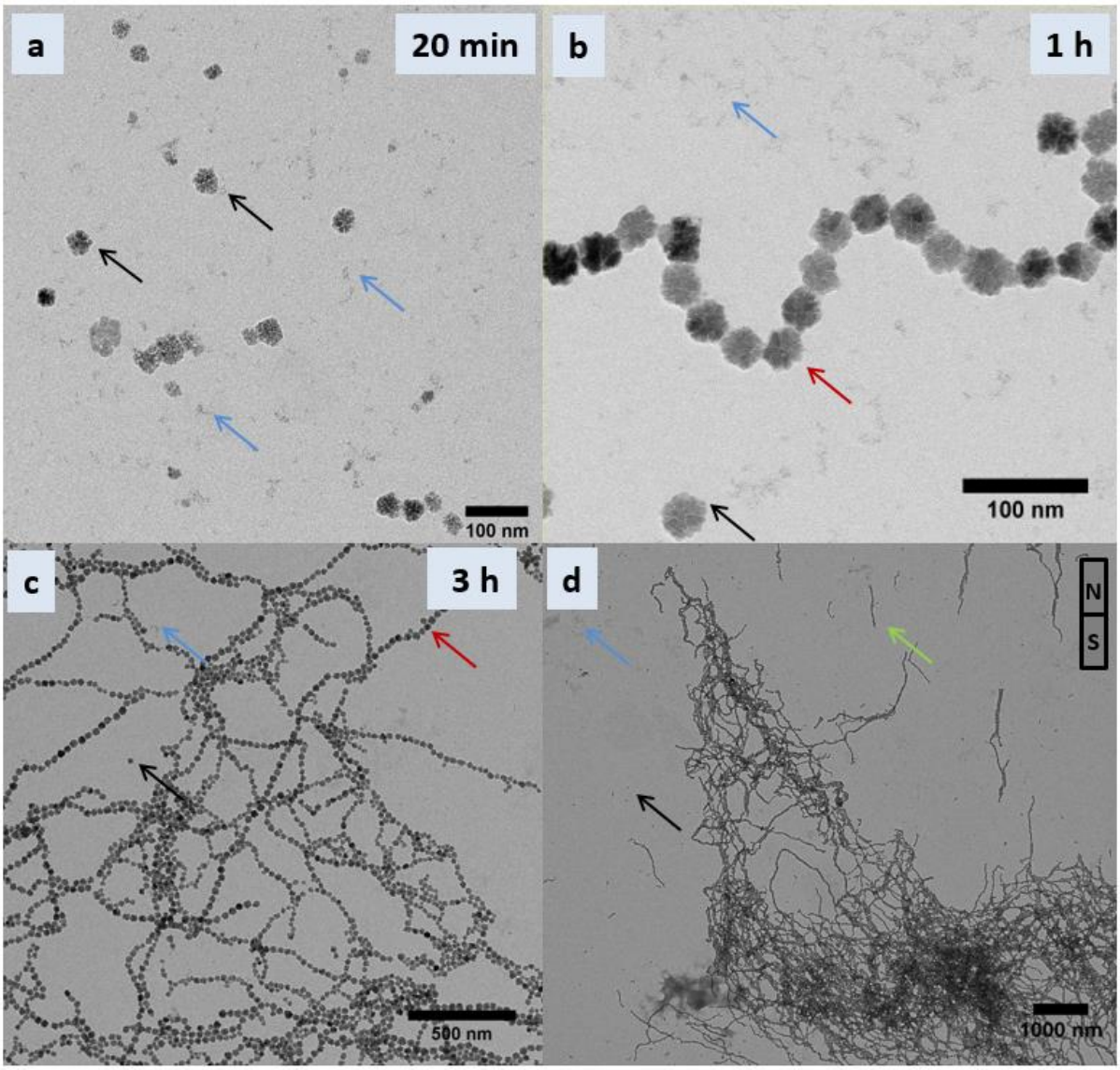

Figure 15: TEM images of polyR-magnetite nanoparticles after (a) 20 minutes, (b) 1 h and (c) 3 h of synthesis. (d) TEM image of aligned stable polyR-magnetite nanoparticle within a strong magnetic field. The arrows indicate precursor particles (blue), polyR-magnetite nanoparticles (black), chain assemblies of polyR-magnetite nanoparticles (red) and chain assemblies of polyR-magnetite nanoparticles aligned within a strong magnetic field (green).

3.1.2 SIZE DISTRIBUTION AND COMPOSITION OF POLYR-MAGNETITE NANOPARTICLES

WAXS data of polyR-magnetite nanoparticles were recorded, mean diameters were extracted and the iron phase was determined through single peak analysis of the WAXS spectrum using the software DPDAK by implementing the Scherrer equation (see chapter 2.4). The WAXS spectrum in Figure 16a shows additional salt peaks with NaCl being a side

product of the chemical reaction (see chapter 2.1.2). The lattice parameter is *a* = 8.3853 +/- 0,0001 Å, which proofs that the material is magnetite (see chapter 2.4). In TEM size analysis, using the software ImageJ, only 100 particles were measured, whereas in WAXS data analysis bulk dimension was determined. Interestingly, the mean diameter of these nanoparticles does not change over time and no further particle growth is obtained after a mean size of 31.4 ± 2.7 nm (Figure 16b). In comparison to WAXS data, TEM observations confirm that the measured size distribution of polyR-magnetite nanoparticles are monodisperse, with a mean diameter of 38.9 nm ± 3.7 nm (inset to Figure 17b). The size distribution of the polyR-magnetite nanoparticles is similar to that of magnetosomes from magnetotactic bacteria, which are often used as a reference for monodispersity (Thomas-Keprta et al., 2000).

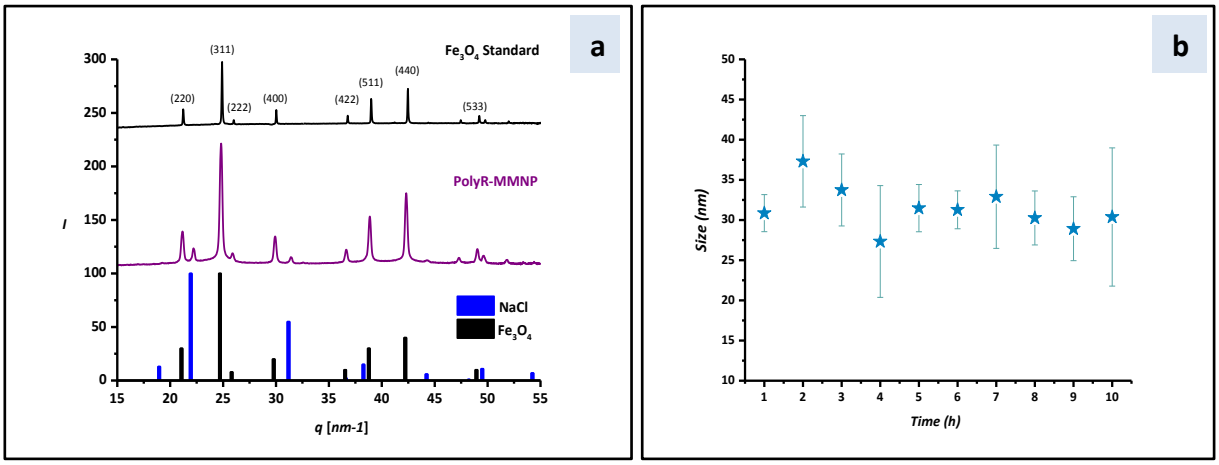

Figure 16: WAXS analyses: (a) Diffraction profile of Fe_3O_4 standard, polyR-magnetite nanoparticles and theoretical diffraction peaks of Fe_3O_4 and NaCl. (b) Evolution of the particle size during synthesis of polyR-magnetite nanoparticles as measured by the Scherrer equation (1h to 10 h of synthesis).

3.1.2.1 Discussion

After co-precipitation of magnetite nanoparticles in the presence of polyR, colloidal stable and monodisperse particles were formed, which did not grow larger than 40 nm in diameter. Naked magnetite nanoparticles are highly negatively charged in alkaline medium during co-precipitation and results in agglomeration, as it was shown for pure magnetite nanoparticles after 1 h of co-precipitation, thus the aggregation strongly depends on the pH.

Agglomeration is reducing the energy associated with the high surface area to volume ratio of nanosized particles. With increasing pH, the surface charge density is decreasing. If pH values are higher than the point of zero charge of magnetite (Milonjić et al., 1983), iron oxides exhibit negatively charges (Tombacz et al., 2006). Therefore, naked iron oxide nanoparticles are highly chemically active, whereas chemically stabilization by coating or grafting techniques is frequently used. Thus, we used polyR, which has a strong basic character with a $pK_a > 12$ (Barreira and Silva, 2003), within co-precipitation. The guanidine group of the positively charged polyR is supposed to electrostatically interact with the highly negatively charged (oxyhydr)oxide (Hajdú et al., 2009). In comparison to naked magnetite nanoparticles, our highly monodisperse polyR-magnetite nanoparticles show colloidal stability, due to a stabilization effect of the polypeptide. It was seen in recent studies, that polymers are chemically anchored or physically adsorbed on magnetic nanoparticles. Polymers can form single layers on nanoparticles and create repulsive forces to guarantee a balance between magnetic forces and Van der Waals attractive forces, which are normally acting in between nanoparticles (Wu et al., 2008). Thus, repulsion stabilizes nanoparticles and prevents agglomeration in solution as shown for polyR-magnetite nanoparticle solutions. Furthermore, naked magnetite nanoparticles tend to oxidize after synthesis when exposed to air and transform in their weathering product maghemite (Widdrat et al., 2014). It is important to store magnetite nanoparticles appropriate after synthesis or stabilize them with organic molecules, thus organic molecules act as shields against outer influences, like oxidation (Wu et al., 2008), (Maity and Agrawal, 2007). PolyR may prevent magnetite from oxidation, thus the iron phase of polyR-magnetite nanoparticles was confirmed to be magnetite considering WAXS analysis.

Interestingly, polyR-magnetite nanoparticles do not grow over time. In comparison, precipitated magnetite nanoparticles without additives, show continuous growth over time (Baumgartner et al., 2013a). Obviously, polyR also stabilizes the particles until a certain size and lead to a growth arrest, which is not yet explored. Therefore, our particles exhibit high monodispersity in contrast to naked magnetite nanoparticles (Wu et al., 2008). The obtained polyR shielding could also be a reason for the growth arrest of each particle.

3.1.3 POLYR-MAGNETITE NANOPARTICLES ARE MESOCRYSTALS

The following measurements were performed with our collaborators Éva Tompa and Mihály Pósfai in the department of Earth and Environmental Sciences, University of Pannonia, Hungary and András Kovács and Rafal E. Dunin-Borkowski at the Ernst Ruska Centre for Imaging and Spectroscopy with Electrons in Jülich, Germany. In bright-field (BF) TEM images it can be seen that amorphous material, most likely polyR, surrounds the crystals (Figure 17b). The particles have irregular and flower-like shapes. The 40 nm polyR-magnetite nanoparticles have angular outlines with reentrant angles, suggesting that they are composed of sub-units, observable in BF TEM (Figure 17b). High-resolution TEM (HRTEM) images confirm that each 40 nm polyR-magnetite nanoparticle is composed of smaller sub-units, which is indicated by the distinct contrast (typically bright) along their boundaries and by the presence of different HRTEM contrast in the parts that make up the entire polyR-magnetite nanoparticles and have variable thicknesses in the electron beam direction (Figure 17c).

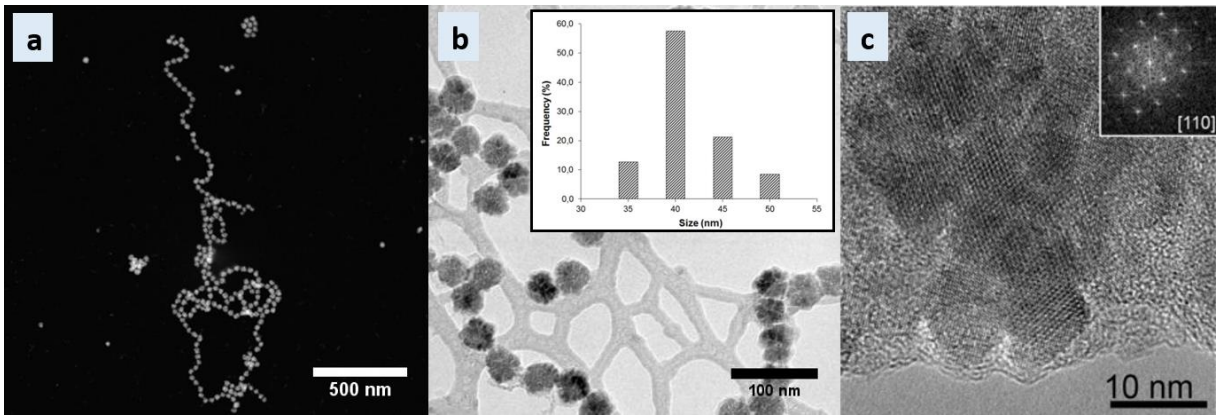

Figure 17: (a) High-angle annular dark-field (HAADF) scanning TEM (STEM) image and (b) BF TEM image of polyR-magnetite nanoparticles assembled in chains. The particles show light and dark contrast in (a) and (b), respectively. The web-like feature in the background in (b) is caused by the lacey C support film on the grid. The inset in (b) shows the particle size distribution, as measured from TEM images, using the software ImageJ. (c) HRTEM image of a polyR-magnetite nanoparticle recorded with the electron beam parallel to the [110] direction of magnetite. The Fourier transform of the particle is shown in the inset and indicates that, even though the particle consists of several smaller sub-units, it is similar to the diffraction pattern of a single crystal.

Electron tomographic reconstructions reinforce the irregular shapes of the particles. Hence, slices were extracted from the tomographic reconstructions and reveal ~1-nm gaps within the particles, at the boundaries of their sub-units (Figure 18).

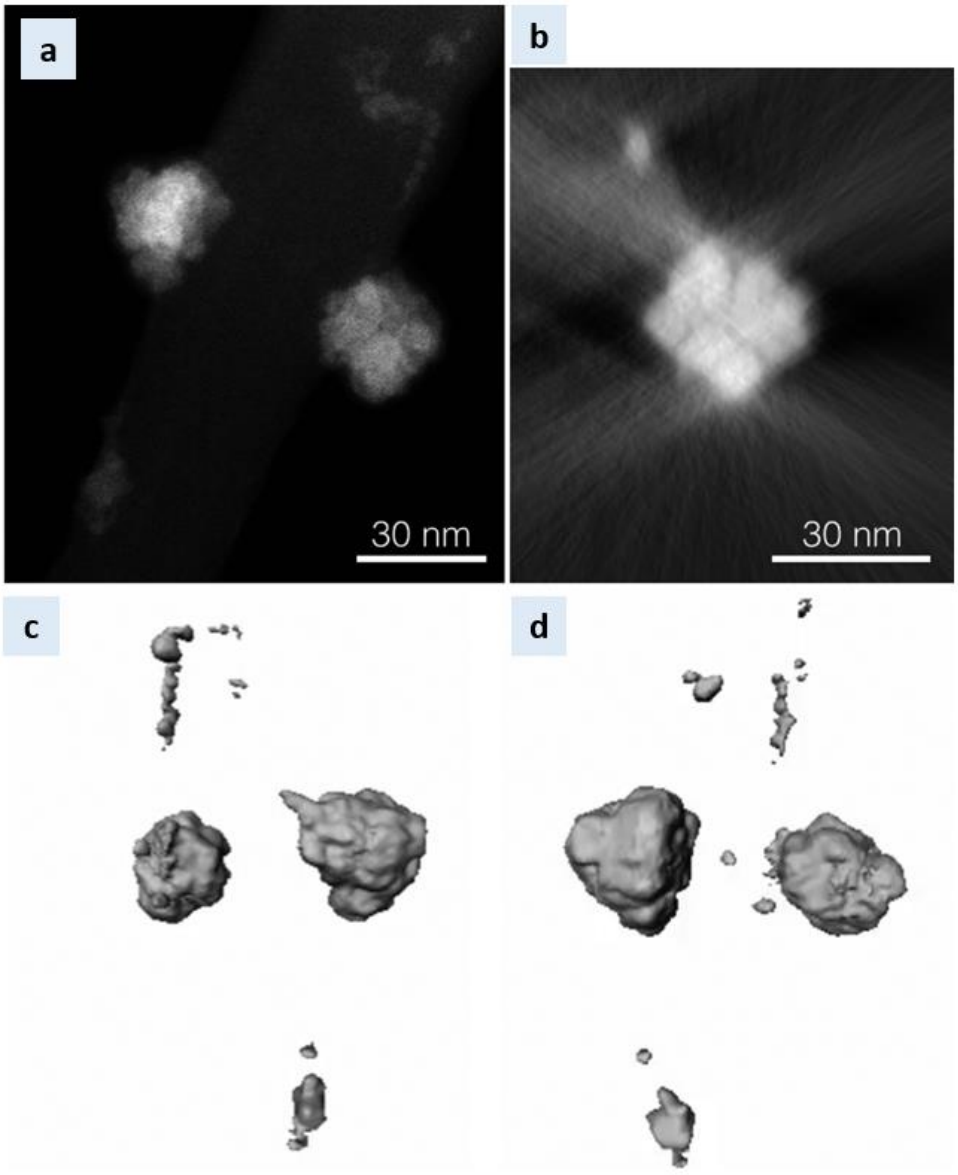

Figure 18: (a) HAADF STEM image of two larger polyR-magnetite nanoparticles and additional smaller ones on carbon support. (b) Slice of the polyR-magnetite nanoparticle extracted from the tomographic reconstruction indicate the ~1-nm-gap between its sub-units. (c, d) Three-dimensional reconstruction of polyR-magnetite nanoparticles showed from two different angles.

Both SAED patterns obtained from individual particles (Figure 19) and Fourier transforms of their HRTEM images (inset of Figure 17c) are similar to single-crystal-like diffraction patterns for the entire 40 nm particles, which suggest a uniform crystallographic orientation of the sub-units (in spite of the gaps between them).

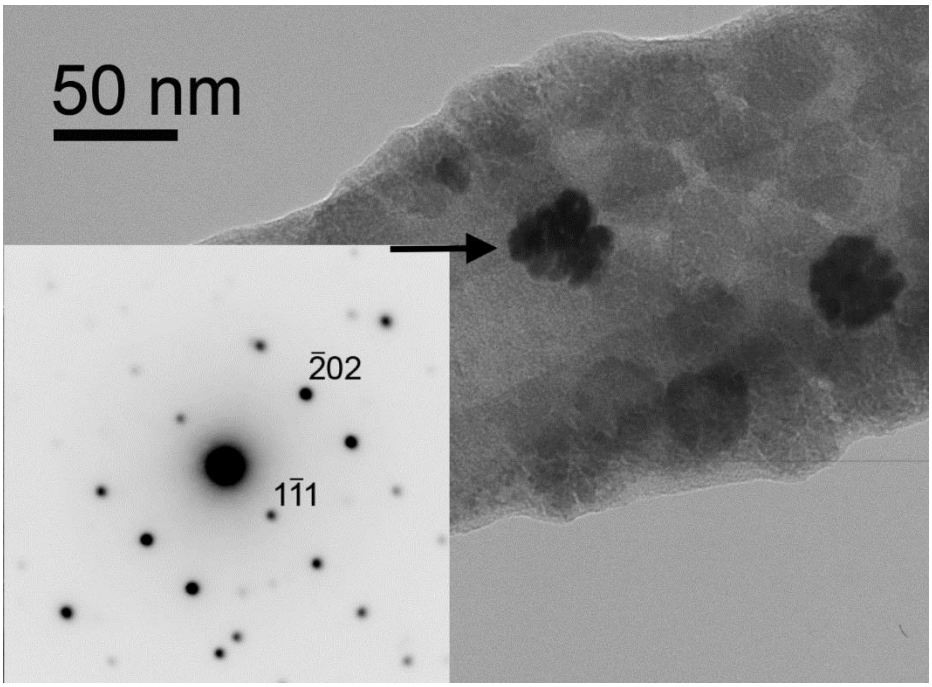

Figure 19: Bright-field TEM image of a cluster of polyR-magnetite nanoparticles on a carbon substrate. The inset in the lower left shows a single-crystal-like SAED pattern of the polyR-magnetite nanoparticle (showed with an arrow), recorded with the electron beam parallel to the [121] crystallographic direction of magnetite.

3.1.3.1 DISCUSSION

Most likely, polyR-magnetite nanoparticles are formed in a three-stage process during co-precipitation. Primary particles with sizes of 2 nm are firstly formed during synthesis and clearly differ from polyR-magnetite sub-units (9 ± 3 nm), which means that the nanoparticle formation does not arise by simple stabilization of primary particles by polyR, they are supposed to first form and then aggregate into magnetite sub-units, as observed in experiments without additives (Baumgartner et al., 2013b). The latter size fits well with the sizes of the sub-units, which were observed in the larger 40 nm particles. It can be

speculated that the 9 nm sub-units aggregate along similar crystallographic orientations and magnetic mesocrystals are formed through oriented attachment with the help of polyR, in a similar process of what has been recently described for goethite (Yuwono et al., 2010). This aggregation of nanoparticles with similar crystallographic orientations leads to the single-crystal-like structure.

A mesocrystal is an assembly of umpteen small crystals of similar shape and size mostly in the nanometer-regime, forming a micrometer-sized superstructure (Cölfen and Antonietti, 2008), (Sturm and Cölfen, 2016), (Yao et al., 2013). These special structures are mainly formed with the help of organic molecules and are typically found in biological systems, such as calcium carbonate mesocrystals formed in sea urchin spines (Seto et al., 2012). Sea urchin spines consist of co-oriented mesocrystals, which assembles from nano bricks (Yang et al., 2011). Additionally synthetic mesocrystals were created in recent years, as well as magnetic mesocrystals. An electrochemical corrosion synthesis route was published recently, which describes the production of mesocrystalline microdisks (Yao et al., 2013). These microdisks show hierarchical architecture and reach 30 µm in size, which is thousendfold larger than our polyR-magnetite mesocrystals. However, they consist of many layers composed of 20 nm nanoparticles, which self-assemble into the superstructured microdisks (Yao et al., 2013). Last year, another magnetite mesocrystal was described, synthesized by using the solvothermal treatment of ferrous chloride in ethylene glycol and 300 nm microspheres were formed. They consist of average crystalline sizes of 23 nm, which are forming a dense assembly within one microsphere. Similar to our polyR-magnetite mesocrystals, they display single-crystalline-like structures. The neighboring primary particles have the same orientation, which remind us of the sub-units in polyR-magnetite nanoparticles (Wan et al., 2015).

3.1.4 POLYR-MAGNETITE NANOPARTICLES HAVE A STABLE SINGLE DOMAIN MAGNETIC BEHAVIOR

As discussed in the previous chapter, 40 nm polyR-magnetite nanoparticles, based on 10 nm sub-units which are supposed to be SP, were obtained, whereas each 40 nm particle should exhibit a magnetic SSD behavior. Therefore, the magnetic properties of polyR-magnetite nanoparticles were measured. The following measurements were performed with our collaborators Dr. Monika Kumari and Prof. Dr. Ann M. Hirt at the Institute of Geophysics,

ETH-Zürich, Switzerland and Prof. Dr. András Kovács and Prof. Dr. Rafal E. Dunin-Borkowski at the Ernst Ruska Centre for Imaging and Spectroscopy with Electrons in Jülich, Germany. As mentioned earlier, polyR-magnetite nanoparticles show a magnetic response when placing them within an applied magnetic field (figure 15 d). The analyzed bulk magnetic properties of polyR-magnetite nanoparticles show a thin hysteresis loop, with a coercivity Hc of 4.2 mT and a ratio of saturation remanent magnetization (Mrs) to saturation magnetization (Ms) of 0.29 (Figure 20a). The hysteresis loop reaches saturation at an external field of 200 mT when the high-field slope was removed for the paramagnetic behavior. The first order reversal curve (FORC) distribution shows a spread along the coercivity axis from zero to approximately 20 mT and the presence of small closed contours in the vicinity of the origin are shown (Figure 20b). The presence of smaller particles is demonstrated through the fact that the distribution is narrow and very close to the origin. A significant contribution from multi-domain particles would be indicated by a broader FORC distribution at the origin. Moreover, the decomposition of FORC measurements into reversible and irreversible components of induced magnetization indicates that about 25% of the magnetic behavior of the samples occurs due to the superparamagnetic particles, whereas the rest of the polyR-magnetite nanoparticles comprising SSD magnetic behavior (Figure 20c) (Kumari et al., 2014).

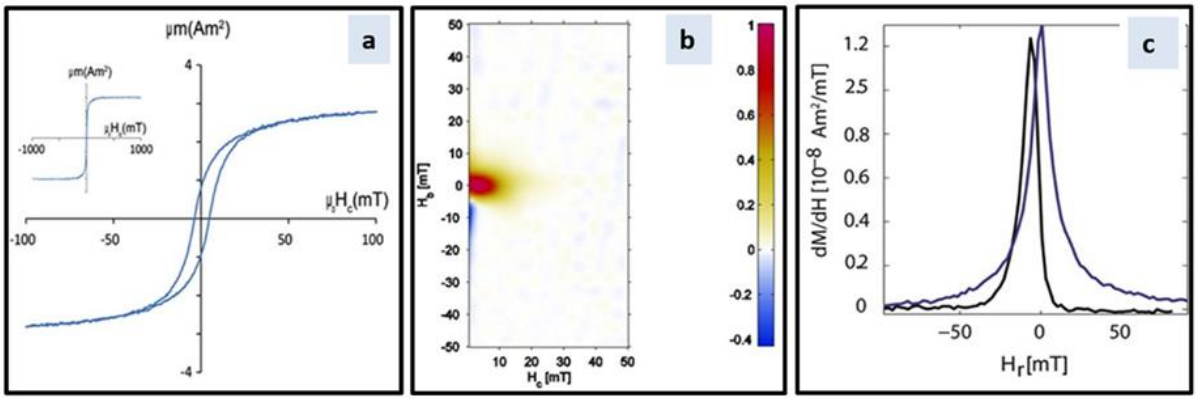

Figure 20: Bulk magnetic characterization of polyR-magnetite nanoparticles. (a) Hysteresis loops with the inset showing the saturation attained at high field; FORC diagram with a smoothing factor of 2; (c) derivative of the magnetic moment of the reversible (blue curve) and irreversible (black curve) part of the induced magnetization of polyR-magnetite nanoparticles.

Furthermore, off-axis EH was used in TEM to study the magnetic induction within and around individual polyR-magnetite nanoparticles arranged in rings and chains. The sub-structuring of polyR-magnetite nanoparticles and their interactions between are determined and thus, the influence on their magnetic properties. A representative magnetic induction map of a ring of six particles shows that each polyR-magnetite nanoparticle contains of a single magnetic domain (Figure 21a). An additional magnetic induction map of a chain structure is shown in Figure 21b. The configuration shows that most of polyR-magnetite nanoparticles contain single magnetic domains, within the magnetic induction direction. This is indicated by the overall direction of the chain. Additionally, one can see that two of the largest polyR-magnetite nanoparticles are most likely in the multi domain state (MD), due to differences in the directions of the contour lines and colors.

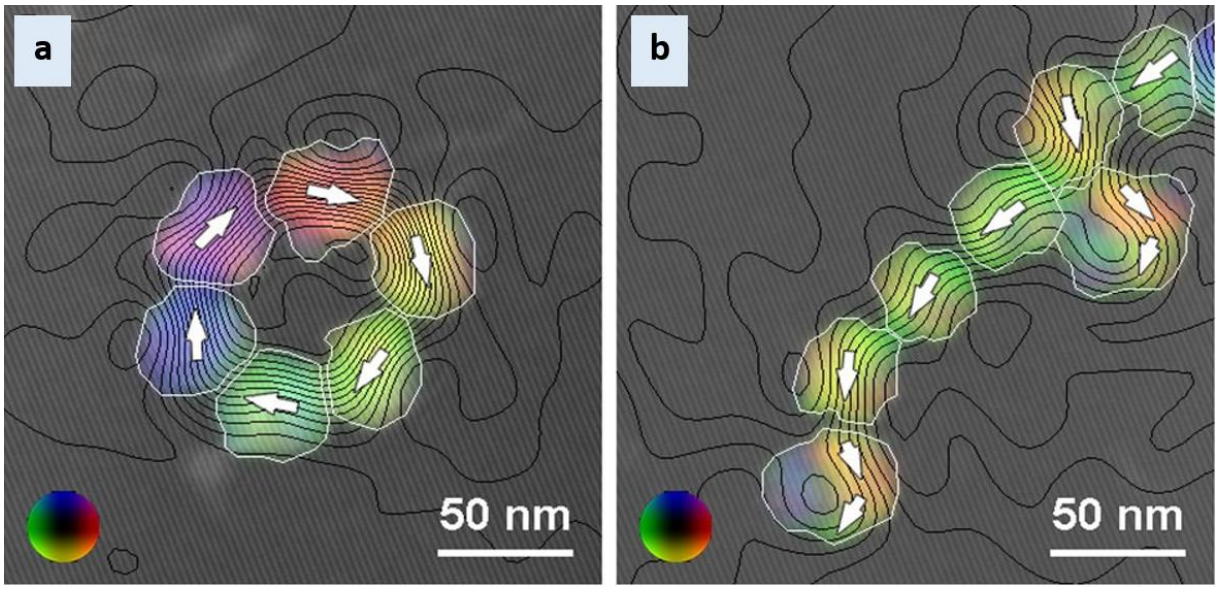

Figure 21: Magnetic induction maps recorded in magnetic-field-free conditions using off-axis electron holography from (a) a ring and (b) a chain of polyR-magnetite nanoparticles. The contours and colors show the strength *and direction of the projected in-plane magnetic flux density, respectively and are superimposed on a combination of the mean inner potential contribution to the phase and an off-axis electron hologram. A color wheel is shown as an inset at the lower left corner of each image, whereas each color refers to the direction of magnetization of each particle. The phase contour spacing is 2π/256 radians in each image. The white arrows indicate the direction of the magnetic induction in each particle. The thin white lines show the outer edge of each polyR-magnetite nanoparticle.*

3.1.4.1 DISCUSSION

Interestingly, our polyR-magnetite nanoparticles are of mesocrystalline nature, where small sub-units create a large crystal and thus, this crystal superstructure is dictating its crystallographically properties. Hence, the question arises, if also the magnetic properties are driven by the superstructure or created by sub-units? A magnetic nanocrystal cluster formed by sub-particles were presented some years ago (Ge et al., 2007). These particles exhibit thermally blocked states and are based on sub-units that are potentially too large to display SP behaviour, whereas the larger 174-nm superstructured particles themselves are too large to show SSD magnetic behaviour, additionally the particles are composed of misaligned 10.9 nm nanocrystals. Their superstructure diffracts like a single crystal in a similar fashion as our polyR-magnetite nanoparticles, thus the magnetic properties differ. PolyR-magnetite nanoparticle bulk samples consist of 25 % SP and 75 % SSD behavior according to FORC measurements, which indicates that also the magnetic properties are determined by the size of the superstructure rather than of its components. A single-crystal-like structure is created through aggregation along similar crystallographic orientations and additionally favors by the magnetic properties of the material in the form of exchange coupling, which was also shown for hematite, which is less magnetic than iron oxide (Frandsen et al., 2005). The magnetic properties of hematite are dominated by those of the sub-units, thus spindles consist of a porous structure. PolyR-magnetite particles were additionally measured with EH to proof that each magnetic mesocrystal exhibit SSD behavior, which was confirmed for almost all polyR-magnetite crystals in the magnetic induction maps. The individual sub-units within each particle interact magnetically, even though gaps of 1 nm separate the sub-units from each other as it was observed in ET. Interestingly, some of the larger polyR-magnetite nanoparticles exhibit multi domain (MD) magnetic behavior due to EH measurements. These particles could provide information about the minimum size that is necessary to form a MD particle. It can be suggested, that the magnetostatic interactions with the neighbor crystals are not significantly influencing as the particles have similar magnetic states independent of their position. The threshold between SSD and MD behavior was predicted to be located between 70 nm without interactions and up to 200 nm for chains of interacting grains (Fabian et al., 1996; Muxworthy and Williams, 2009). Similar to magnetosome chains (Kiani et al., 2015), all particles exhibit SSD behaviour, thus the mesocrystalline polyR-magnetite nanoparticle`s

permanent magnetic dipoles interact with each other and result in chain formation of the nanoparticles. Inorganically synthesized magnetite of similar particle size typically forms chains instead of dense clusters (Xuan et al., 2007). In general, nanoparticle chain-like assemblies are limited and often collapse into clusters or closed-ring structures, the so-called flux-closure rings (Hu et al., 2008).

3.1.5 MESOCRYSTAL "GLUE": THE ORGANIC PART OF POLYR-MAGNETITE NANOPARTICLES

Small gaps in between the sub-units were detected in HRTEM images and electron tomography and could be potential placeholders for the remaining polyR. To gain information about the organics localization could provide a better understanding of the mesocrystal formation, its control over structural and magnetic properties according to its superstructure and potentially interactions between sub-units. Elemental maps are constructed from EDXS spectrum images and show the elemental composition of polyR-magnetite nanoparticles, which is composed of Fe and O (Figure 22b, c). In addition to the 40-nm particles, Fe and O signals occur as well as for primary particles that are dispersed on the TEM grid (for example, in boxed area on the right in Figure 22d). These small features probably represent the precursor iron oxide particles that first form in the synthesis process. Additionally, the presence of C in the polyR-magnetite nanoparticles (Figure 22e), obtain from parts of polyR-magnetite nanoparticles that extends above holes in the lacey carbon supporting substrate and thus can be analyzed without the contribution of any carbon-bearing background (Figure 22d).

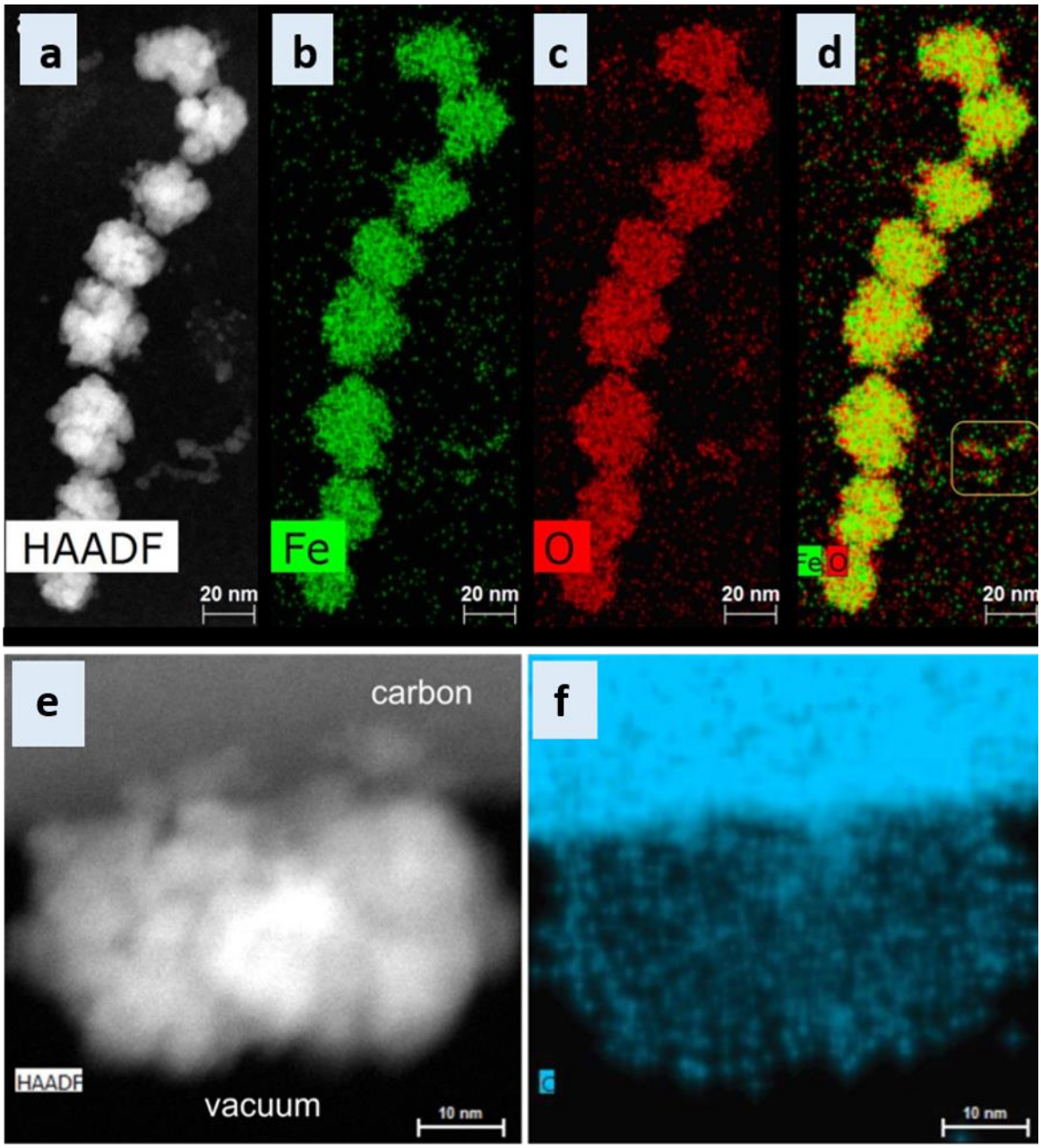

Figure 22: Compositional analysis of a chain of eight particles. (a) HAADF STEM image; (b) Fe, (c) O, and (d) Fe+O elemental maps obtained from EDXS spectrum images. The boxed area in (d) contains smaller particles that are also composed of Fe and O. Compositional analysis of a single magnetite particle that is attached to the side of the lacey carbon support film, with its lower part in vacuum. (e) HAADF STEM image and (f) C elemental map obtained from EDXS spectrum images.

However, the carbon is detected on the particle, the question is not yet solved if carbon is additionally filling the prior mentioned gaps. To get an idea of the overall carbon within polyR-magnetite nanoparticles, TGA experiments were performed. PolyR-magnetite nanoparticles were measured in very little amounts after freeze drying (1 mg). However, an

assumption can be made that polyR-magnetite nanoparticles consist of approximately 10 % of organic in comparison to the inorganic part (Figure 23).

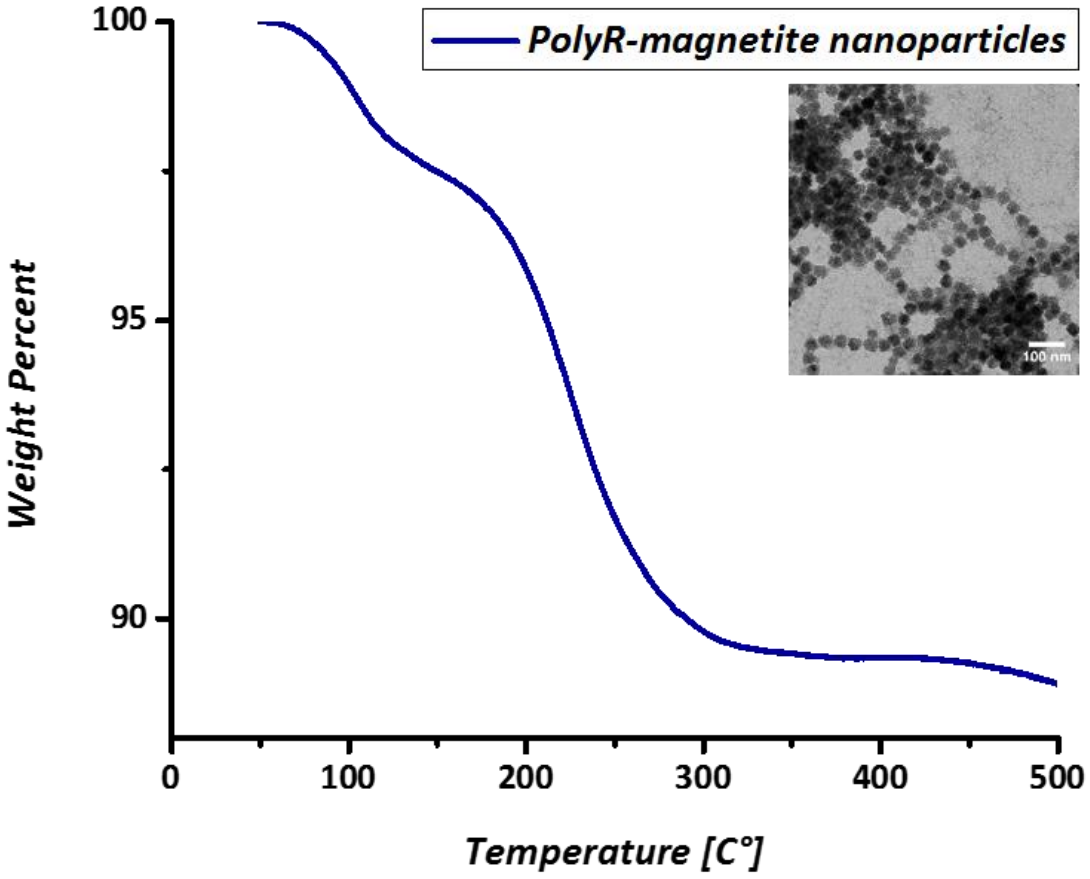

Figure 23: TGA results of polyR-magnetite nanoparticles: 10 % of organic was lost, which means that polyR-magnetite nanoparticles consist of 10 % poly-l-arginine. The inset shows a TEM image of polyR-magnetite nanoparticles used for TGA analysis.

3.1.5.1 SMALL ANGLE NEUTRON SCATTERING STUDIES OF POLYR-MAGNETITE NANOPARTICLES, POLYR-^{57}MAGNETITE NANOPARTICLES AND ^{57}MAGNETITE NANOPARTICLES

Further structural analysis measurements and presented data were performed using SANS, with the help of our colleague Dr. Emanuel Schneck in the department of Biomaterials, MPIKG, Germany and of our collaborators Dr. Vitaliy Pipich and Dr. Baohu Wu at the KWS-1 diffractometer of JCNS outstation at the FMR II reactor in Garching, Germany. SANS experiments can resolve the sub- and superstructure of the particles and are sensitive to the

internal organic distribution. A specialty of this scattering method is a procedure called contrast variation (Banc et al., 2016). PolyR-magnetite nanoparticles were synthesized replacing the iron source by other stable isotopes: $^{57}FeCl_2$ and $^{57}FeCl_3$ (PolyR-^{57}magnetite nanoparticles). This enables to change the scattering length densities of the material, which subsequently can be matched with prior calculated solutions of a D_2O and H_2O mixture. Notably, polyR-^{57}magnetite nanoparticles exhibit smaller mean sizes in diameter of 23.9 nm ± 4 nm than polyR-magnetite nanoparticles. When analyzing polyR-^{57}magnetite nanoparticles in TEM, the mesocrystalline structure of polyR-^{57}magnetite nanoparticles (Figure 24b) remains and the chain formation is similar to polyR-magnetite nanoparticles (Figure 24a). Additionally, ^{57}magnetite nanoparticles without additives were synthesized using the same iron isotope as a control (Figure 24). ^{57}Magnetite nanoparticles (Figure 24d) show slightly smaller mean size of 6.9 nm ± 1.7 nm than magnetite nanoparticle controls (Figure 24c) with mean sizes of 10 nm ± 2.8 nm (Figure 25).

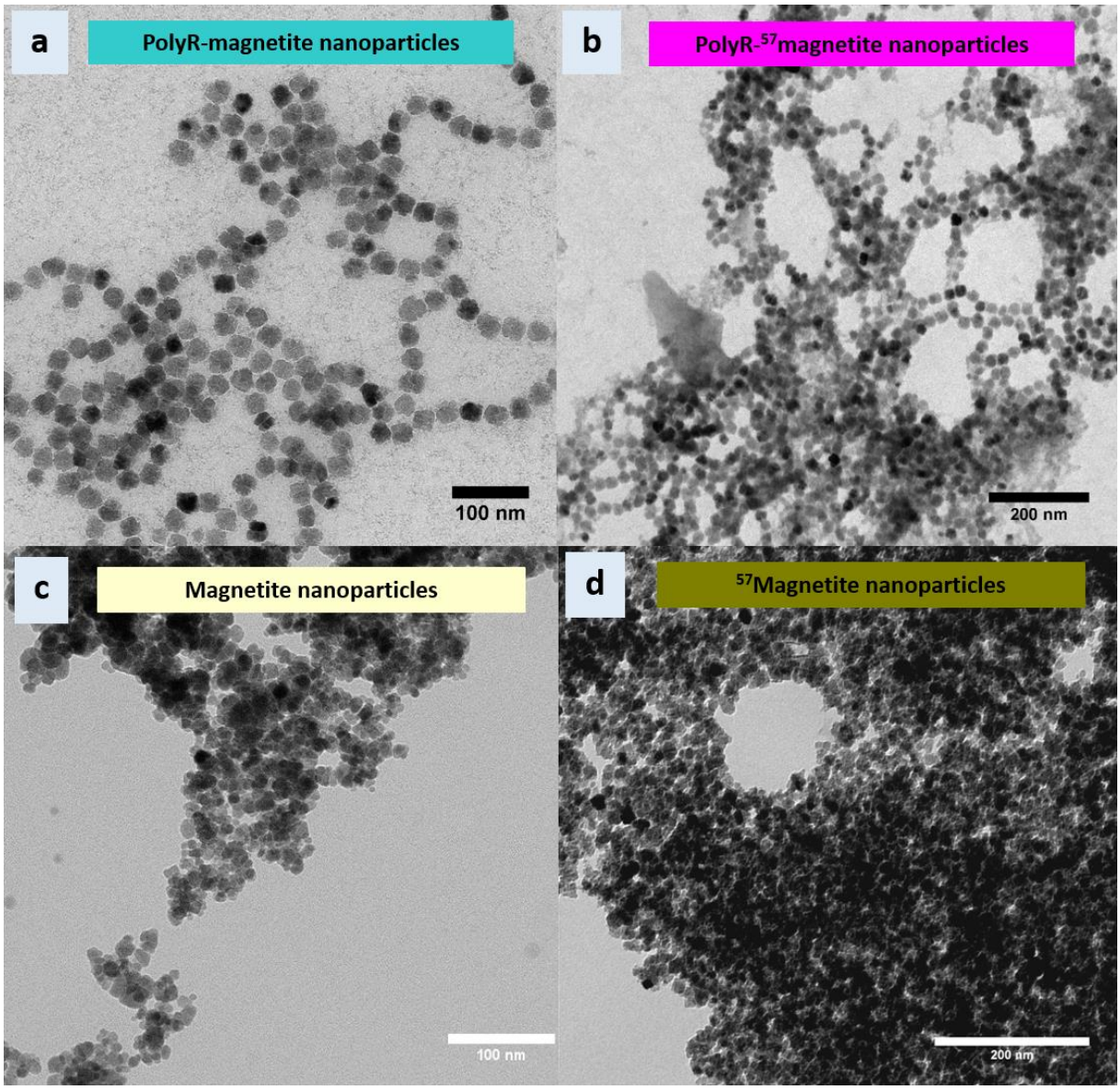

Figure 24: TEM images of different polyR-magnetite nanoparticles and naked magnetite nanoparticles precipitated with different iron isotopes. (a) PolyR-magnetite nanoparticles, (b) polyR-^{57}magnetite nanoparticles, (c) magnetite nanoparticles and (d) ^{57}magnetite nanoparticles.

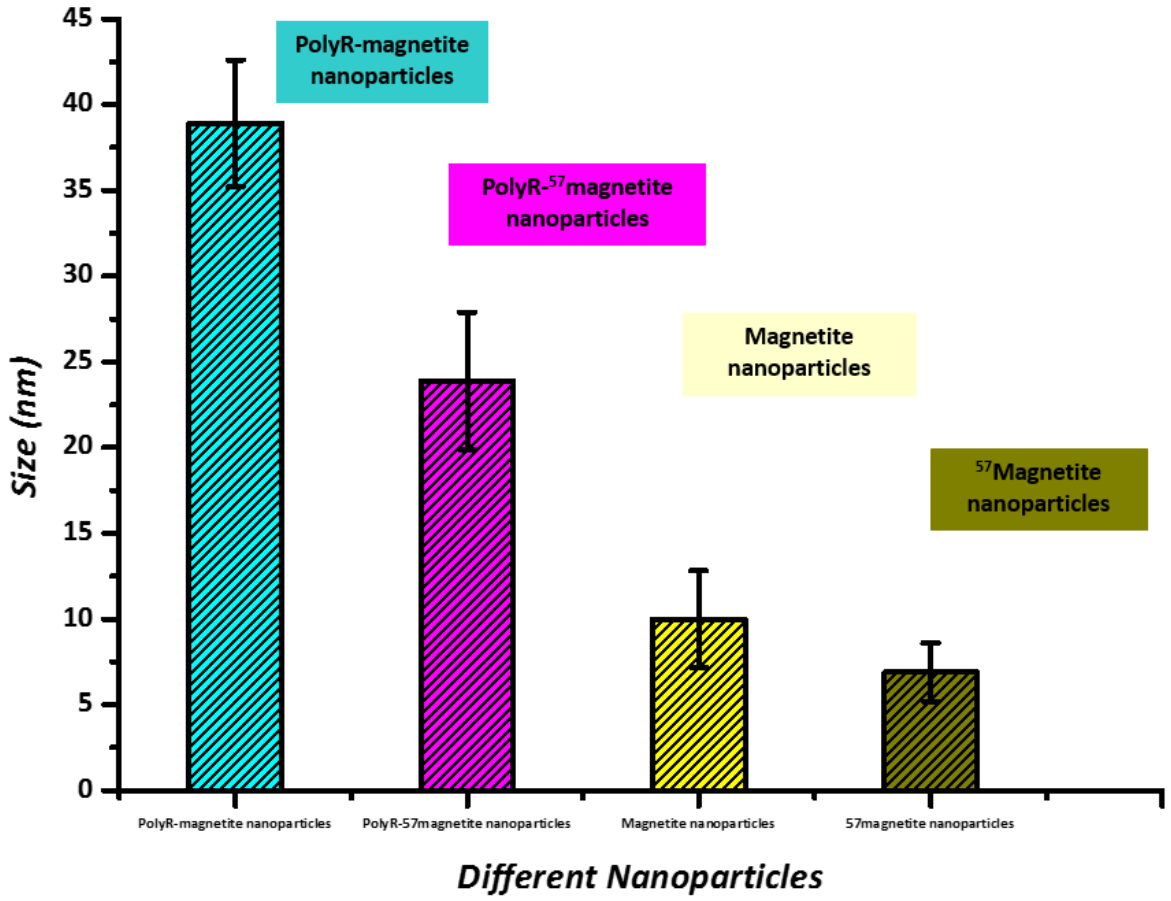

Figure 25: Size distribution of four different magnetite nanoparticle types referring to the TEM images to previous Figure 24. All sizes were measured using the software ImageJ and the mean of 100 nanoparticles each was calculated.

PolyR-magnetite nanoparticles in different solutions were measured by SANS and the results are compared in the following.

SANS SLOPE OF POLYR-MAGNETITE NANOPARTICLES IN H_2O

Figure 26 represents SANS profiles of concentrated polyR-magnetite nanoparticles in H_2O with Q-ranges from 0.01 to 2 nm^{-1} corresponding to a structure range from 3 to 600 nm. The SANS data in Figure 26 show several distinct Q-regimes, which are well described by a multiple level structure. The scattering following the Q^{-4} power law at less than 0.025 nm^{-1} implies large aggregate/clusters on a length scale larger than 250 nm. The scattering approximately following the Q^{-1} power law between 0.03 and 0.1 nm^{-1} implies a cylinder-like structure on the length scale between 60 nm and 200 nm. Above $Q \approx 0.1$ nm^{-1}, the power

law transforms into a Q^{-4} decay. The solid line is a theoretical fit based on a cylinder model using the software SasFit. The fit parameters (effective cylinder radius = particle radius x √(2/3): 12 nm and infinite cylinder length, are consistent with previous results obtained by electron microscopy. Therefore, the real particle radius is ~ 14.6 nm, which results in diameters of ~ 30 nm. Most interestingly, above $Q \approx 0.3$ nm^{-1} the power law transforms from ~ Q^{-4} into a Q^{-3} and indicates a mass fractal structure, which shows the presence of polypeptide within the magnetite nanoparticles. The scattering of a mesocrystal without organics in its gaps would scatter more like separate particles and would show a platform in the slope. An organic-filled mesocrystal shows a power law scattering ranging from Q^{-2} to Q^{-3}. Interestingly, a weak but significant and reproducible peak at around $q = 0.7$ nm^{-1} (see arrow in Figure 26) indicates the existence of some periodic ordering on a length scale of about 9 nm in diameter. This length scale coincides with the apparent size of the sub-units identified by EM, and thus corroborates the above interpretation.

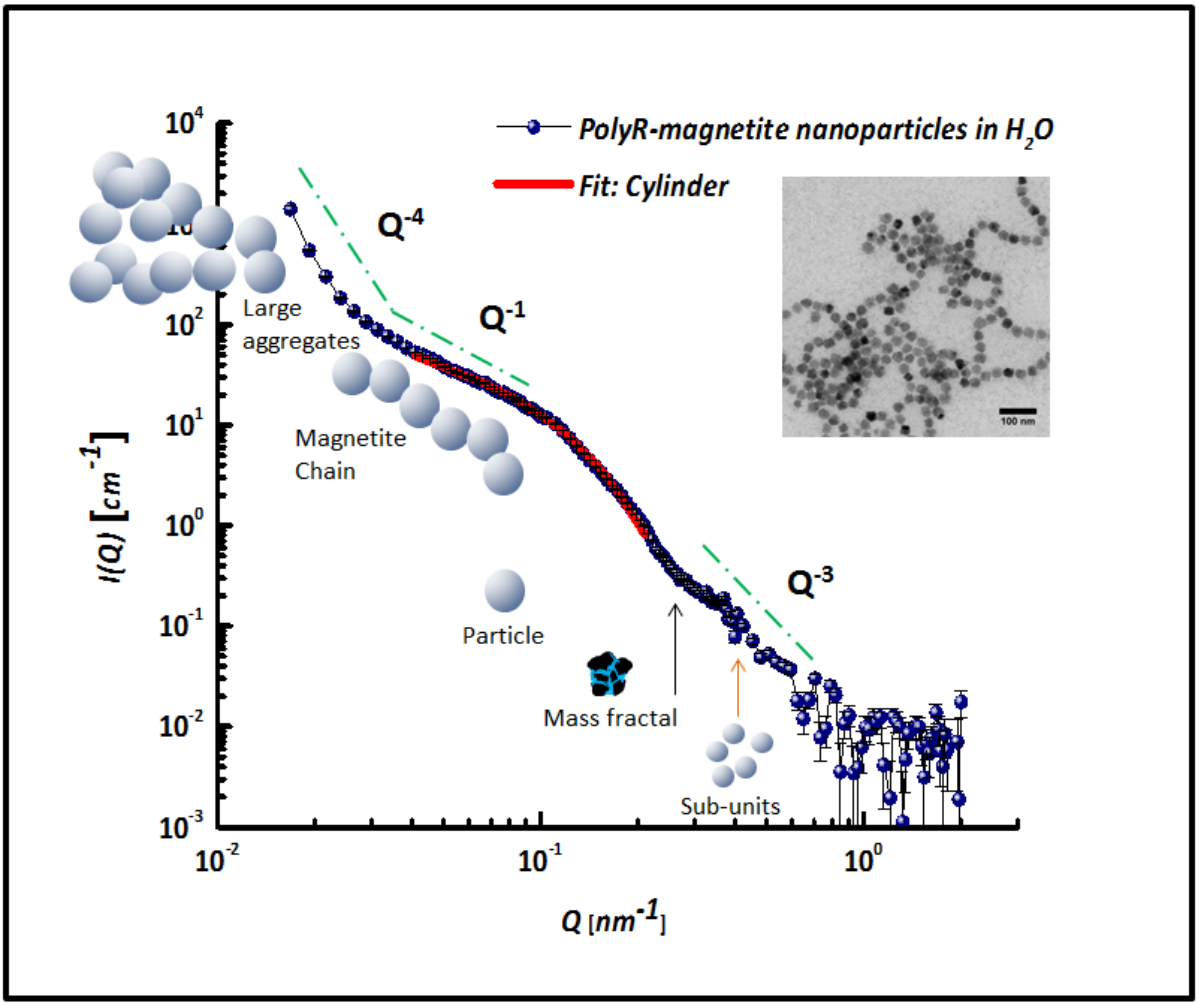

Figure 26: SANS macroscopic cross section I versus the scattering vector Q for highly concentrated polyR-magnetite nanoparticles in pure water. Different Q regimes can be obtained (dashed green lines). The inset shows a TEM image of the measured polyR-magnetite nanoparticles. The dashed lines (red) represent a fit of a Cylinder using SasFit. The black arrow indicates the mass fractal and the orange arrow indicates sub-units.

SANS SLOPE OF POLYR-^{57}MAGNETITE NANOPARTICLES IN D_2O

Figure 27 represents the SANS profile of concentrated polyR-^{57}magnetite nanoparticles in D_2O in the same q-range than seen in Figure 26. The SANS data in Figure 27 show several distinct Q-regimes which are well described by a multiple level structures similar than for polyR-magnetite nanoparticles in Figure 26 with the exception that the effective cylinder radius of 6.5 nm is smaller, which corresponds to the real particle radius of ~ 8 nm, corresponding to the nanoparticle mean diameters of ~ 16 nm. Smaller mean sizes were additionally confirmed through TEM (Figure 25). This is in good agreement with the fit in

Figure 26, whereas larger diameters were calculated according to large particles precipitated without ^{57}Fe. However, when measuring the isotope particles in D_2O, no sub-units are seen anymore.

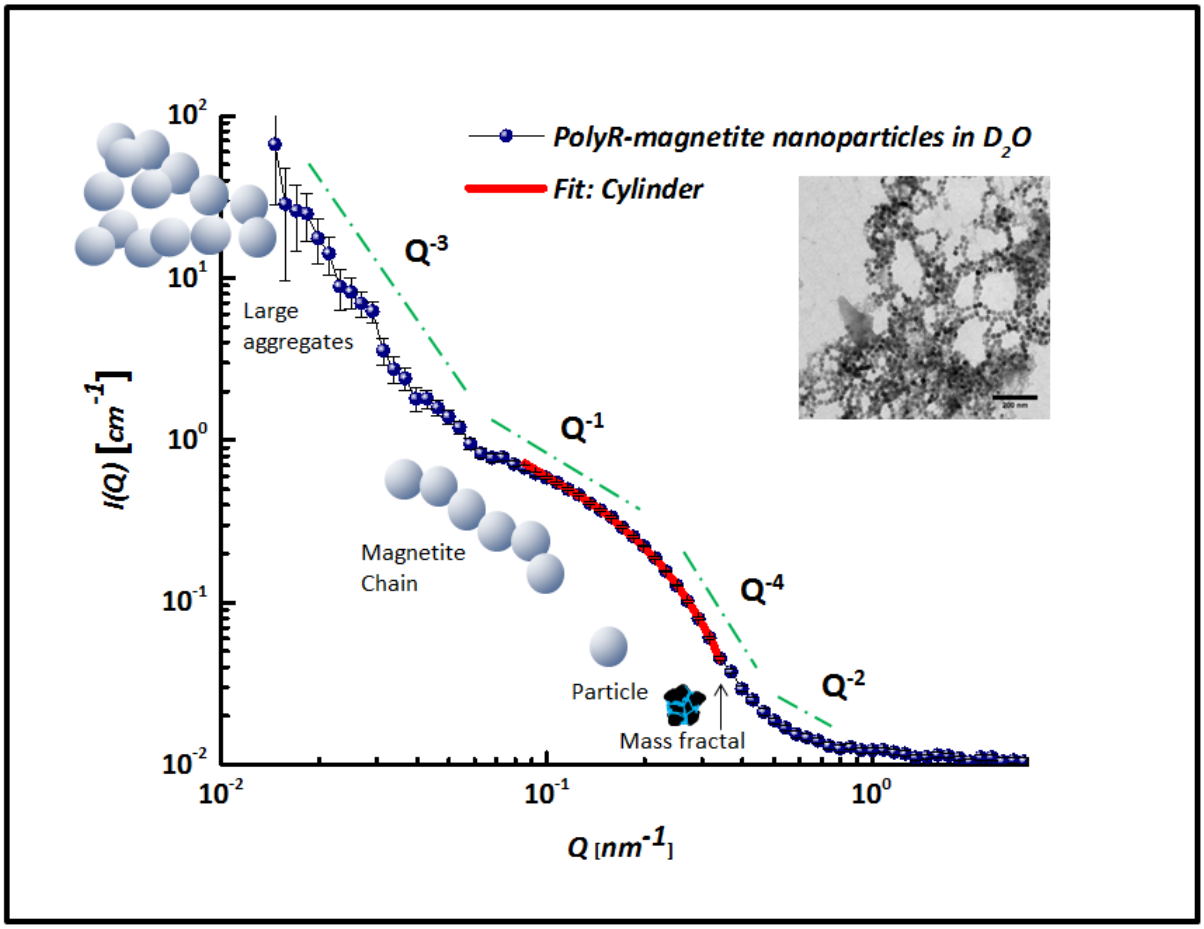

Figure 27: SANS macroscopic cross section I versus the scattering vector Q for highly concentrated polyR-^{57}magnetite nanoparticles in D_2O. Different Q regimes can be obtained (dashed green lines). The inset shows a TEM image of the measured polyR-^{57}magnetite nanoparticles The black arrow indicates the mass fractal.

SANS SLOPES OF POLYR-^{57}MAGNETITE NANOPARTICLES IN H_2O COMPARED TO ^{57}MAGNETITE NANOPARTICLES IN $^{57}Fe_3O_4$ MATCH POINT SOLUTION

PolyR-^{57}magnetite nanoparticles in $^{57}Fe_3O_4$ match point solution (D_2O: H_2O of 67,3 %: 32,7%) were measured, and compared with pure ^{57}magnetite nanoparticles in the same match point solution. One can see a change from Q^{-2} (Figure 28a), corresponding to the slope of polyR-^{57}magnetite nanoparticles, and to Q^{-3} (Figure 28b), corresponding to ^{57}magnetite nanoparticles. Thus, the intensity signal remains, although the inorganic fraction of the particles of both samples were supposed to be invisible rendered. The inserts in both figures (Figure 28) correspond to the expected visible fraction within the match point solution, whereas a signal should be only detected in Figure 28a.

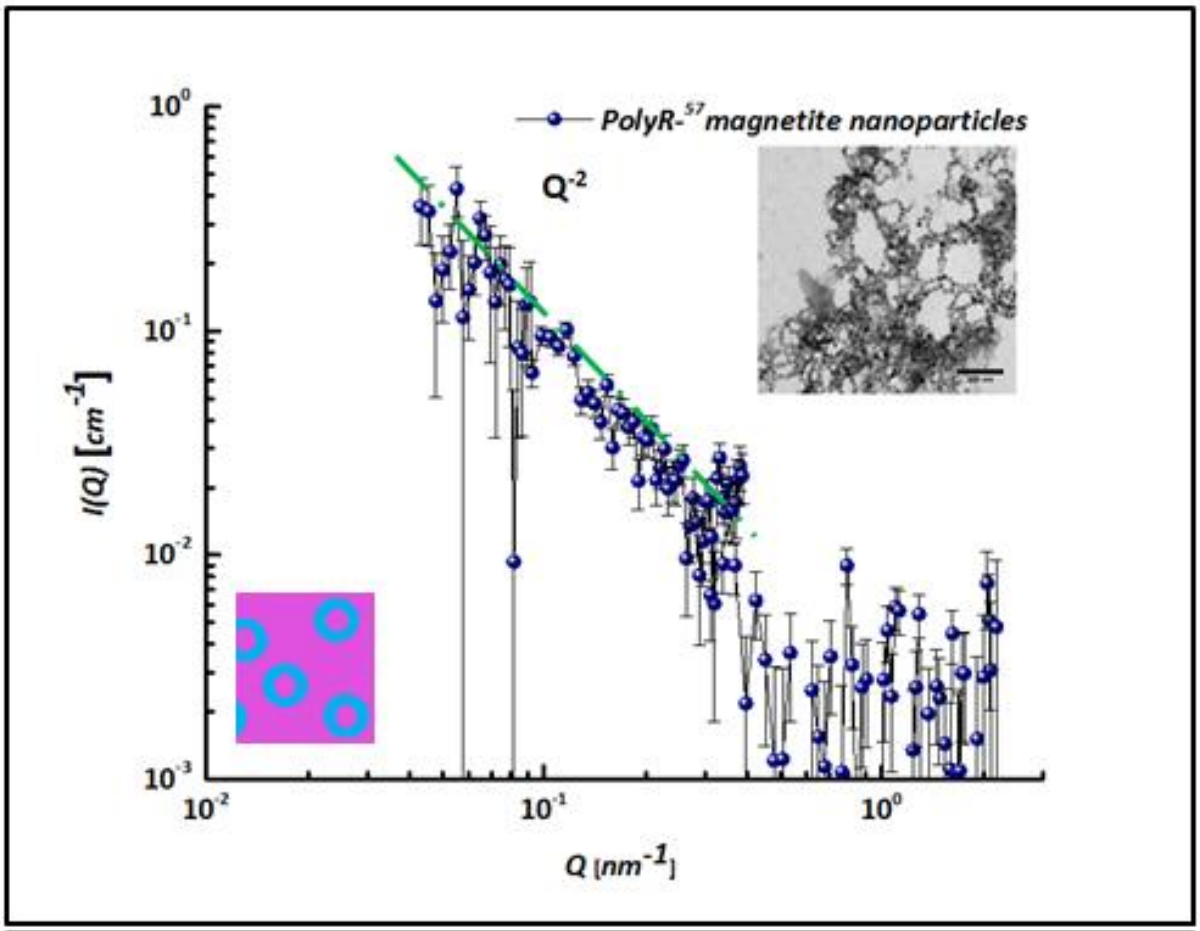
PolyR-57magnetite nanoparticles
Q-2
I(Q) [cm-1]
Q [nm-1]
10^0
10^-1
10^-2
10^-3
10^-2
10^-1
10^0

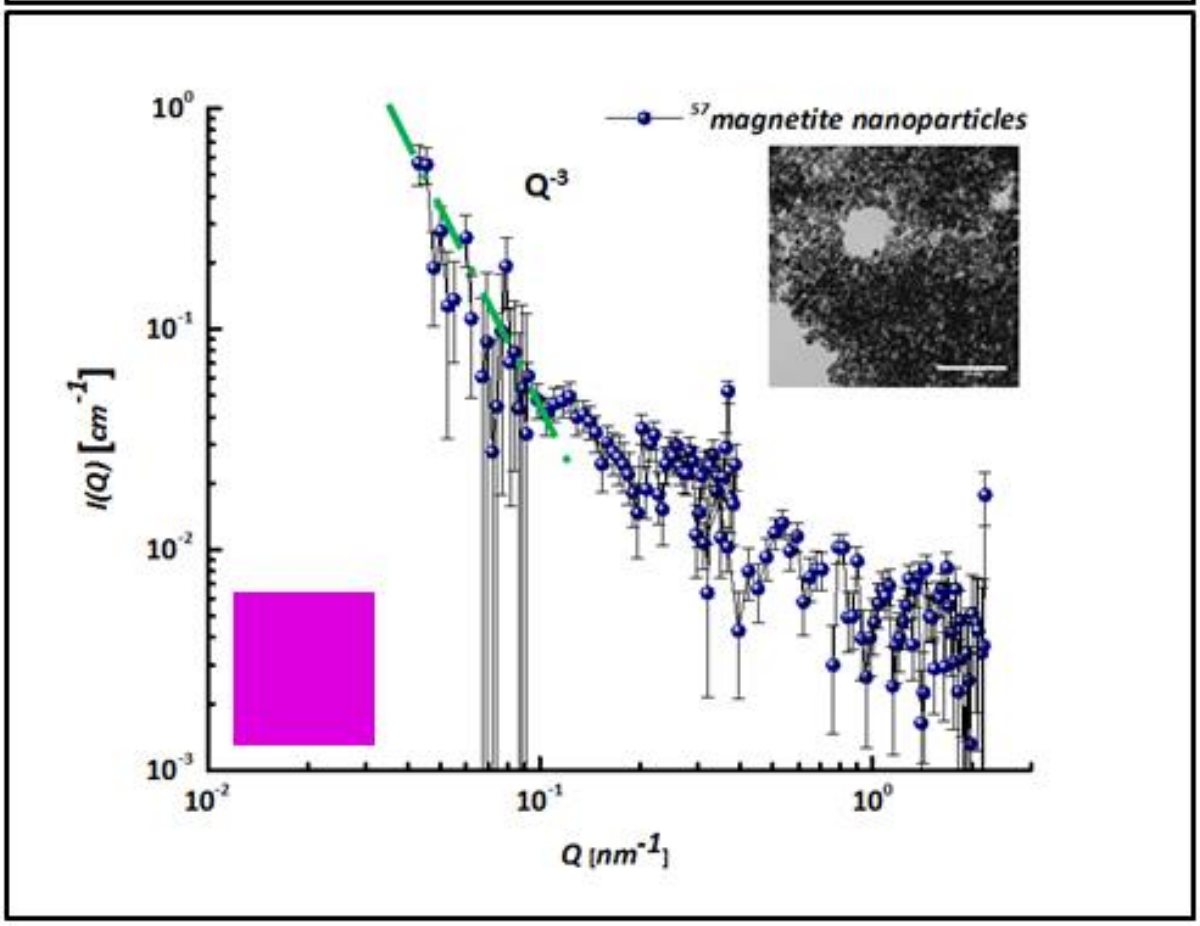
57magnetite nanoparticles
Q-3
I(Q) [cm-1]
Q [nm-1]
10^0
10^-1
10^-2
10^-3
10^-2
10^-1
10^0

Figure 28: (a) SANS macroscopic cross section I versus the scattering vector Q of highly concentrated polyR-^{57}magnetite nanoparticles in $^{57}Fe_3O_4$ match point solution (D_2O: H_2O of 67,3 %: 32,7%). The inset shows a TEM image of the measured polyR-^{57}magnetite nanoparticles. (b) SANS macroscopic cross section I versus the scattering vector Q of pure ^{57}magnetite nanoparticles in $^{57}Fe_3O_4$ match point solution. The inset shows a TEM image of the measured pure ^{57}magnetite nanoparticles. Different Q regimes can be obtained (dashed green lines). (Schemes according to both contsrast matches (see Figure 12) are shown in the boxes on the lower left sides of each slope).

3.1.6 DISCUSSION

To get an overall idea about the organic distribution and localization within polyR-magnetite mesocrystals, different methods were used, such as HRTEM, EDXS analysis and TGA. HRTEM results indicate that polyR is surrounding the mesocrystals and furthermore, small gaps are recorded within mesocrystal sub-units, which are most likely filled with polyR. An inhomogeneous distribution of carbon signals was seen within the polyR-magnetite nanoparticles according to EDXS analysis. The data indicate that polyR is located within the particles according to the C signal. However, one has to be careful, that the C signals refers to either polyR but could also indicate a C-bearing contamination arising from interaction between the very small and intense electron probe and also the particle surface cannot be excluded. Referring to literature, EDXS is often used to gain information of certain organic compounds, such as silanes (Ma et al., 2003), or chitosan (Kievit et al., 2009), located on inorganic nanoparticles, e.g. magnetite. Superparamagnetic polymer nanofibers were introduced by (Tan et al., 2005), whereas the C-signal of the polymer was shown using EDXS. However, these nanosystems exhibit organic material only on the surface, whereas our polyR-magnetite nanoparticles do not show core-shell behavior and therefore it is more complicated to distinguish between outer and internal organic structure. As we have seen in HRTEM, it is obvious that the organic content is minimal compared to the inorganic part of the mesocrystal as only thin organic layers were detected. Therefore, TGA was performed in order to obtain the total amount of organic in contrast to inorganic fraction. Our polyR-magnetite nanoparticles consist of a ratio of 90 % inorganic to 10 % organic typically for mesocrystals, which exhibit up to 30 % of organic (Cöelfen and Antonietti, 2008). Since, we do not gain information of the organic internal structure through the prior mentioned methods, the question still arises if polyR directly interacts in between the sub-units or just

stabilizes the mesocrystal as a surrounding layer in a similar fashion to core shell particles (Laurent and Mahmoudi, 2011). Furthermore, an overall measurement of all structural components of our nanosystem was performed using SANS and corresponding contrast matching experiments were investigated. In a recent paper, magnetosomes of magnetotactic bacteria were measured using SANS. It was shown that measured magnetosomes from the bacterium *Magnetospirillum gryphiswaldense* exhibit magnetic core-shell particles with a core radius of around 22 nm and a shell of around 3 nm thickness (Hoell et al., 2004), which is consistent to a SANS structural analysis of magnetosomes shown in an older publication, where core diameters of around 30 to 40 nm with shell thicknesses of around 4 nm were measured (Krueger et al., 1990). Comparing to magnetosomes, our polyR-magnetite nanoparticles are also surrounded by organic molecules but additionally they consist of 1 nm gaps within their sub-units, which was shown in ET. Is it possible to see organic within these gaps? Last year (Siglreitmeier et al., 2015) published an interesting study, whereas different size-regimes of a multifunctional hybrid material were analyzed using SANS. The structure consists of an organic nacre matrix filled with gelatin, in which magnetite nanoparticles were synthesized. They observed linear structures, indicating chain constructs of particles at a power law of Q^{-1} in a low-Q regime (<0.01 nm^{-1}). We observed similar chain structures, whereas our polyR-magnetite nanoparticle chains are detected in a Q regime between 0.03 and 0.1 nm^{-1}, referring to shorter chain lengths (60 to 200 nm), in conformity with TEM results. Longer chain structures tend to form aggregates, which are detected in a low-Q regime (<0.01 nm^{-1}) at power laws of Q^{-3} to Q^{-4}. These structures are observed at high sample concentrations. When measuring diluted polyR-magnetite nanoparticle samples, no aggregated structures are observed. But, we have to take into account, that highly diluted samples do not show strong scattering, whereas we could not obtain comparable data from diluted polyR-magnetite samples. (Siglreitmeier et al., 2015) additionally showed that the individual magnetite nanoparticles located in the nacre matrix indicate a mass fractal structure at a power law of Q^{-3}, which refers to a branching or cross-linking three-dimensional structure. Similar to their study, we can confirm to see a mass fractal structure at larger Q regimes (>0.1 nm^{-1}) as well, whereas the scattering is determined from individual magnetite mesocrystals. The mass fractal corresponds to particles which are not highly dense packed confirming that the gaps between sub-units are filled with organic. A scheme (Figure 29) shows the differences between solely sub-units

with empty gaps corresponding to a platform in the SANS slope and sub-units with polyR filled gaps corresponding to Q-regimes between Q^{-2} and O^{-3}, consistent with our result. Most likely we can educe from the mass fractal structure, that we found the missing link of our polyR-magnetite mesocrystals. We suggest that the polyR is not solely surrounding but also incorporating polyR-magnetite mesocrystals.

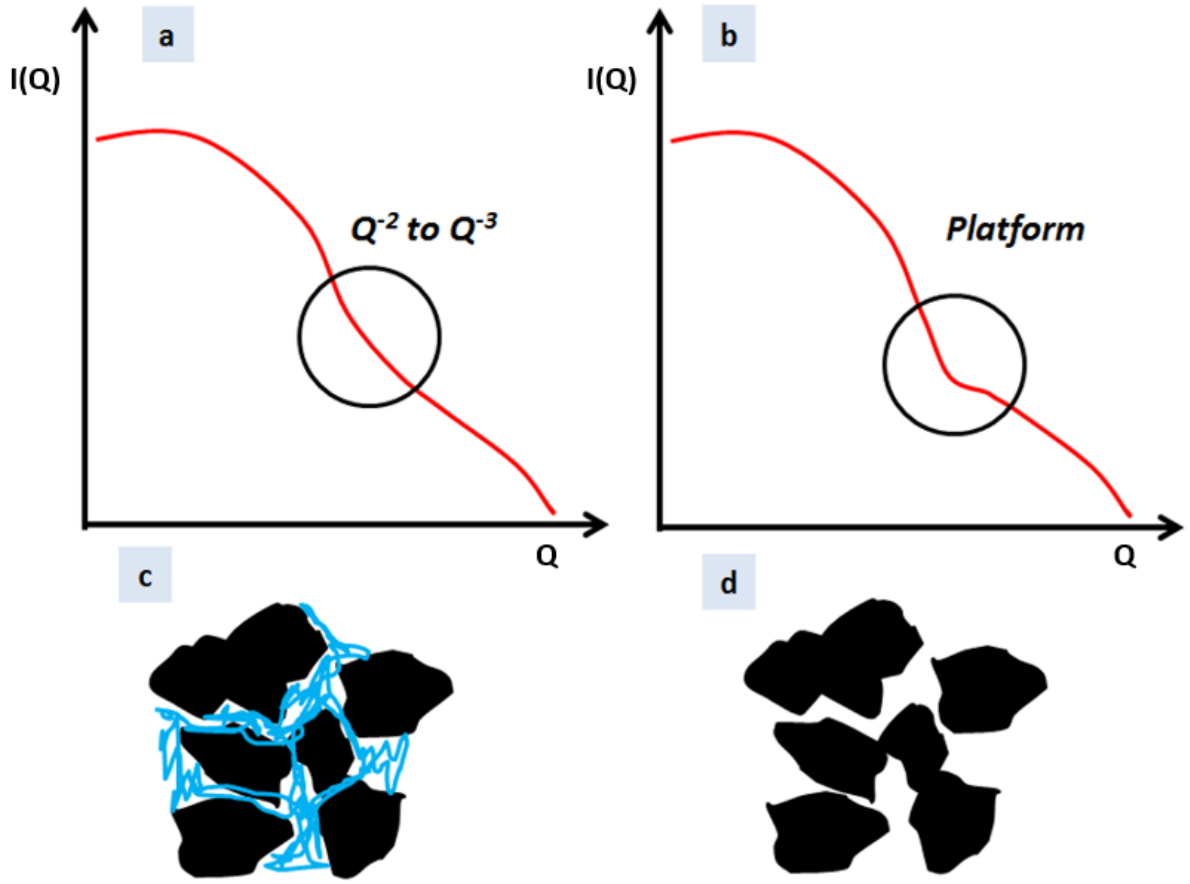

Figure 29: Difference between multiple scattering at the middle Q range is shown. (a) Scattering at (c) a schematic polyR-magnetite mesocrystal with incooprated polyR shows a power law scattering (Q^{-2} to Q^{-3}). (b) Scattering at (d) a schematic polyR-magnetite mesocrystal without polyR (only gap, particles are more seperated) show a platform. Scattering at a mesocrystal with polymer shows a power law scattering (Q^{-2} to Q^{-3}).

Similar to the study of (Siglreitmeier et al., 2015), whereas the match point of gelatin (28 % D_2O) to only detect inorganic structures was used, we conversely tried to invisible render the inorganic part of polyR-magnetite particles. Thus, pure magnetite has a similar SLD to D_2O (Zhao et al., 2016), and therefore exhibits the highest possible SLD, magnetite cannot be invisible rendered. As it is described in chapter 2.6.3, an iron isotope (^{57}Fe) was used to produce polyR-^{57}magnetite nanoparticles and ^{57}magnetite nanoparticles, which exhibits a smaller SLD than D_2O. Interestingly both, polyR-^{57}magnetite nanoparticles and ^{57}magnetite nanoparticles, showed smaller mean diameters than polyR-magnetite nanoparticles. A reason for that could be the magnetic isotope effect, which was described recently (Amor et al., 2016). However, the mesocrystalline structure of the particles remains. Therefore, the match point of $^{57}Fe_3O_4$ (67.3 % D_2O) was used to solely detect the organic compounds within polyR-magnetite nanoparticles.

PolyR-^{57}magnetite nanoparticles were measured additional in pure D_2O. The structure was consistent with our forehand measured polyR-magnetite nanoparticles in H_2O, whereas no sub-units are detected. As the polyR-^{57}magnetite nanoparticles are significantly smaller by trend, they may be composed of fewer sub-units, so that periodicity is less pronounced. Additionally, the contrast is weaker and the peak is simply not seen because of smaller polyR-^{57}magnetite nanoparticles with fewer sub-units.

A residual intensity is still seen when measuring polyR-^{57}magnetite nanoparticles in ^{57}magnetite-matched water. This can either be due to a visible presence of organics or because the match is not perfect. To identify the reason, pure ^{57}magnetite particles were also measured, and still got the same intensity. This means that the organics are not visible in SANS and the signal arises from an imperfectly matched sample. Anyhow, an upper limit for the amount of organics can be defined with this result, containing of little material, confirming the TGA results. However, it was possible to show the organic fraction with the prior mentioned mass fractal. One has to take into account that first SANS analysis was performed using independent Porod analysis on different slope regimes. SasFit was only used to fit parts of the slope to quantify radii of nanoparticles. A concrete model will be implied in the future, which should help to conclude the overall structure of the nanosystem.

3.2 POLYR-MAGNETITE NANOPARTICLES AS POTENTIALLY MEDICAL TOOLS

PolyR-magnetite nanoparticles were tested for their capabilities in different medical applications, such as possible candidates for MRI contrast agents and their performance in hyperthermia. To prove if polyR-magnetite nanoparticles are in general biocompatible for prior mentioned medical applications, static and dynamic cell viability assays were performed as following.

3.2.1 ENDOTHELIAL EFFECTS OF POLYR-MAGNETITE NANOPARTICLES

The following measurements were performed at the University Hospital Erlangen, Germany in collaboration with Dr. Iwona Cicha and Jasmin Matuszak. The biocompatibility of nanoparticles has to be tested for various applications, such as MRI and hyperthermia as mentioned in chapter 3.2.2 and 3.2.3. As endothelial cells comprise the first-contact vascular cells for nanosystems intended for intravascular applications, the effects of magnetic nanoparticles on their viability were tested. For this purpose, Human Umbilical Vein Enthodelial Cells (HUVECs), which is well-known model system for the human endothelium (Onat et al., 2011), (Nordling et al., 2014) were incubated with polyR-magnetite nanoparticles and the contrast agent Resovist® (Reimer and Balzer, 2003) as a control.

3.2.1.1 STATIC CELL VIABILITY ASSAYS

A well-established real-time cell analysis method for nontoxicity studies (xCELLigence) was used for monitoring cell viability. The cell index (see chapter 2.7.1) of untreated, healthy endothelial cells increases continuously over time as seen in Figure 30. When HUVECs were treated with polyR-magnetite nanoparticles, the particles were well tolerated up to concentrations of 50 µg/ml. No significant differences in growth curves were indeed detected in comparison to the control samples. In HUVECs, treated with 100 µg/ml of polyR-magnetite nanoparticles, an inhibition of cell growth was detected with a significantly reduced cell index already after 24h (Figure 30). These values indicate that although the polyR-magnetite particles do not induce cell death at 100 µg/ml, they have a considerable inhibitory effect on cell growth and/or attachment strength at this concentration. The treatment with 200 and 400 µg/ml of polyR-magnetite nanoparticles resulted in a strong and

significantly decrease of the cell index at 24 h, 48 h and 72 h even below the initial values, which is indicating toxicity and cell death (Figure 30). The reference agent, Resovist® seems to induce a slight growth inhibition at 100µg/ml after 72h (appendix Figure 45) and resulted in growth arrest in HUVECs at 200 and 400µg/ ml.

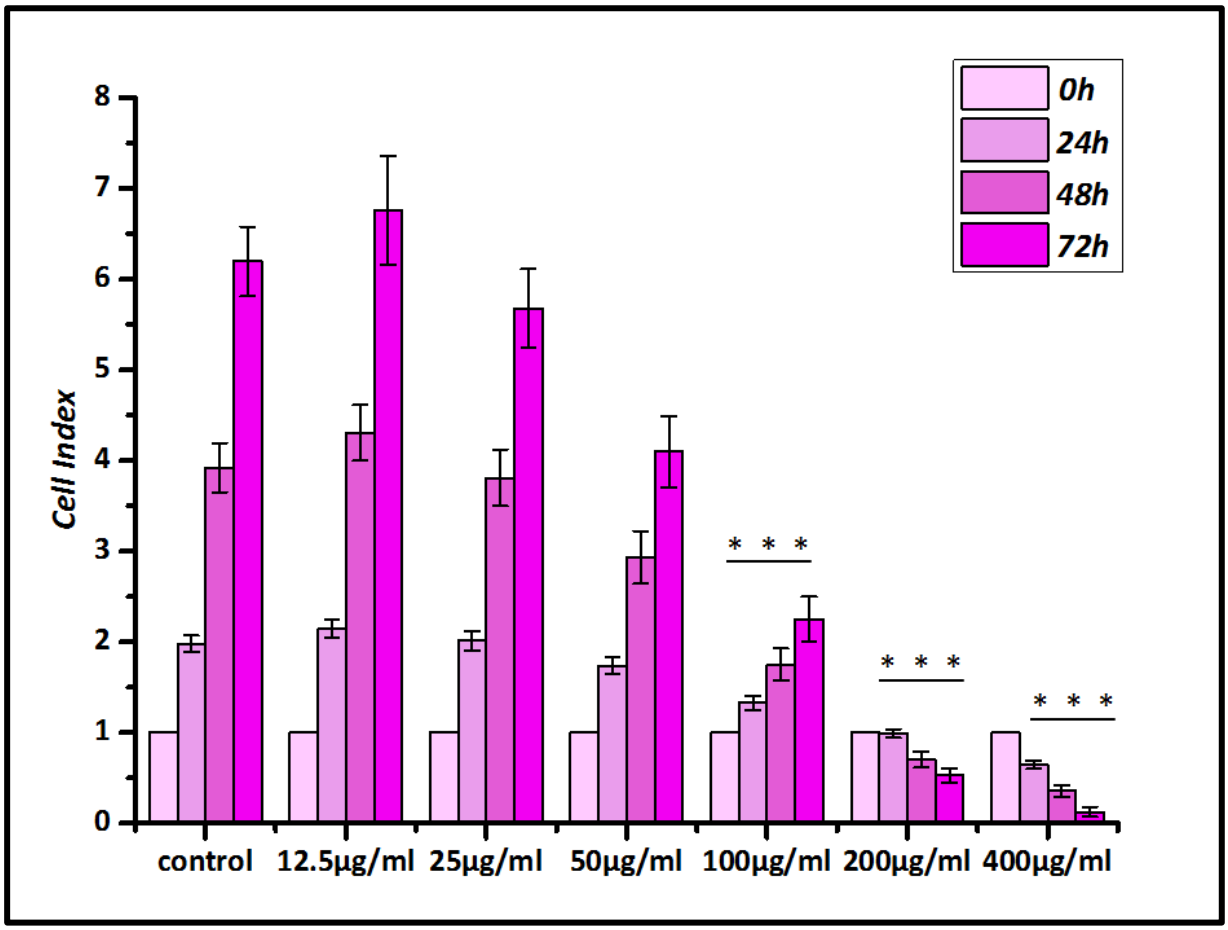

*Figure 30: Biological effects of polyR-magnetite nanoparticles on endothelial cells grown in static conditions by real-time cell analysis. HUVECs were seeded 24h before nanoparticle application. After these initial 24h, particles in different concentrations were added and cell index was monitored up to 72h post application. Cell Index is displayed as x-fold of untreated controls. Data are expressed as mean ± SEM,***p<0.001 vs. corresponding control (One-way Anova); n=3*

To validate the real-time cell measurements, live-cell microscopy was performed using the IncuCyte® system. No difference in confluence, which is the number of adherent cells relating to the surface portion which is covered by cells, of polyR-magnetite nanoparticle treated cells to the control was observed at concentrations up to 100 µg/ml during the

treatment up to 72 h (Figure 31). A decrease in confluence was discovered for 200 and 400 µg/ml. However, cell elongation is observed at 50 µg/ml and more pronounced at higher concentrations, which is not observable in Resovist®-treated cells (appendix Figure 46), although it has to be taken into account that high particle concentrations of magnetic nanoparticles can disturb live-cell imaging and therefore make it difficult to estimate morphological changes. Combining the results of real-time cell analysis and live-cell imaging, it can be estimated, that the decrease of cell index at 100 µg/ml for polyR magnetite nanoparticles is not due to decreased proliferation but cell adherence, due to no changes in confluence observed with IncuCyte. The effect of cell elongation is most likely affecting the cell index as prior described.

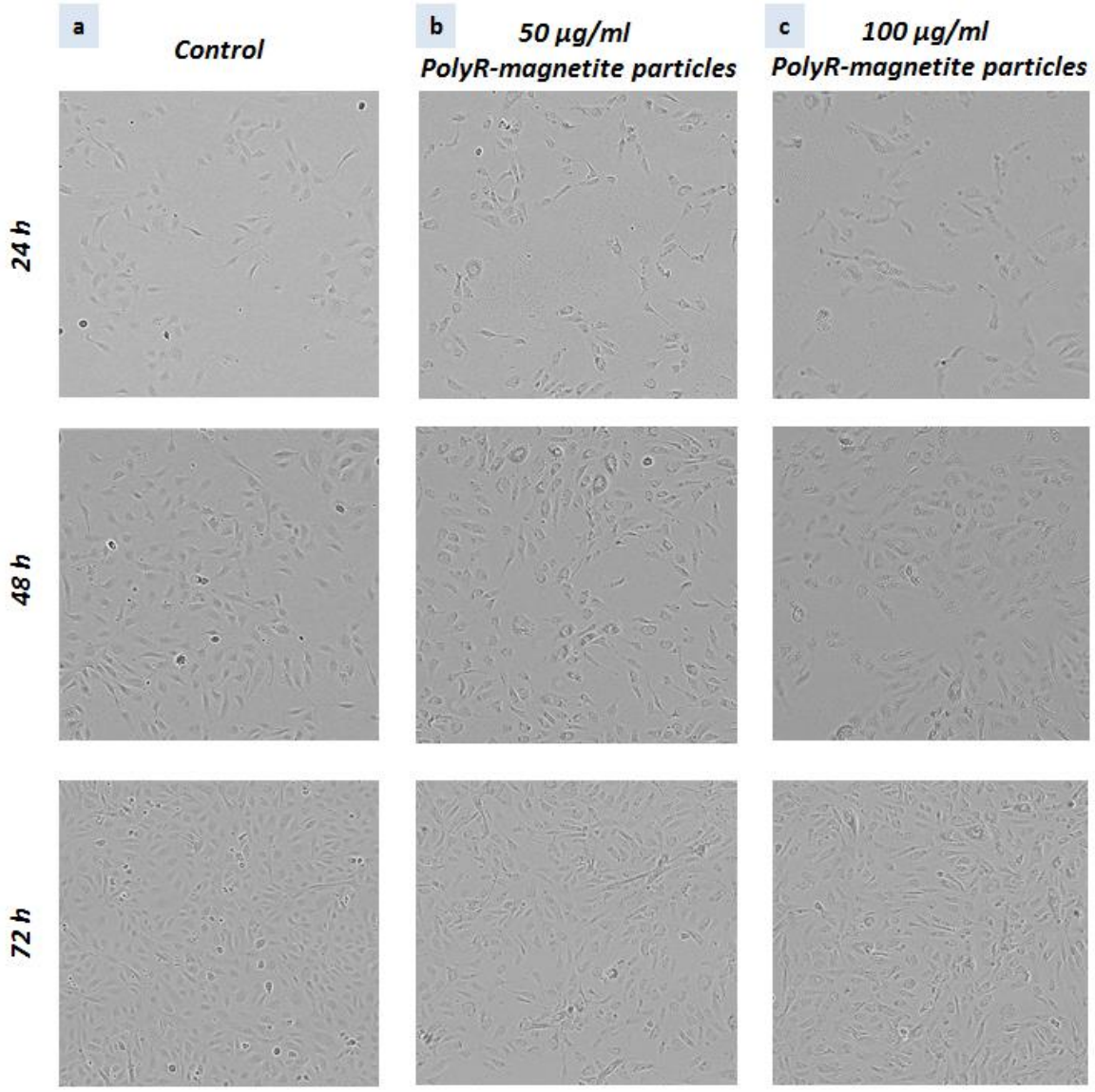

Figure 31: Live-cell microscopy of HUVECs treated with polyR-magnetite nanoparticles: Phase contrast images of HUVECs were taken after 24 h, 48 h and 72 h post particle addition. (a) HUVECs control, treated without any nanoparticles, (b) HUVECs treated with 50 µg/ml and (c) HUVECs treated with 100 µg/ml polyR-magnetite nanoparticles. Representative images of n=3 experiments are shown.

3.2.1.2 DYNAMIC CELL VIABILITY

Toxic effects of circulating substances in dynamic experiments *in vitro* can manifest themselves as endothelial cell shrinking and detachment. The viability and the confluence, as well as the cell morphology and cell-cell contacts upon nanoparticle treatment can be analyzed by immunofluorescent staining. In laminar conditions, polyR-magnetite nanoparticles were better tolerated than in non-uniform conditions in general. As compared with the dynamic control experiments without any circulating nanoparticles (Figure 32a), treatment of HUVECs with 100 µg/ml had no effect on cell numbers or morphology under laminar or non-uniform conditions (Figure 32b). Perfusing the cells with 400 µg/ml polyR-magnetite nanoparticles resulted in a significant decrease of cell numbers under laminar flow. This effect was further pronounced under non-uniform shear stress conditions, where cell detachment areas were observed (Figure 32c). This is additionally confirmed with the confluence data for non-uniform and laminar conditions shown in Figure 33.

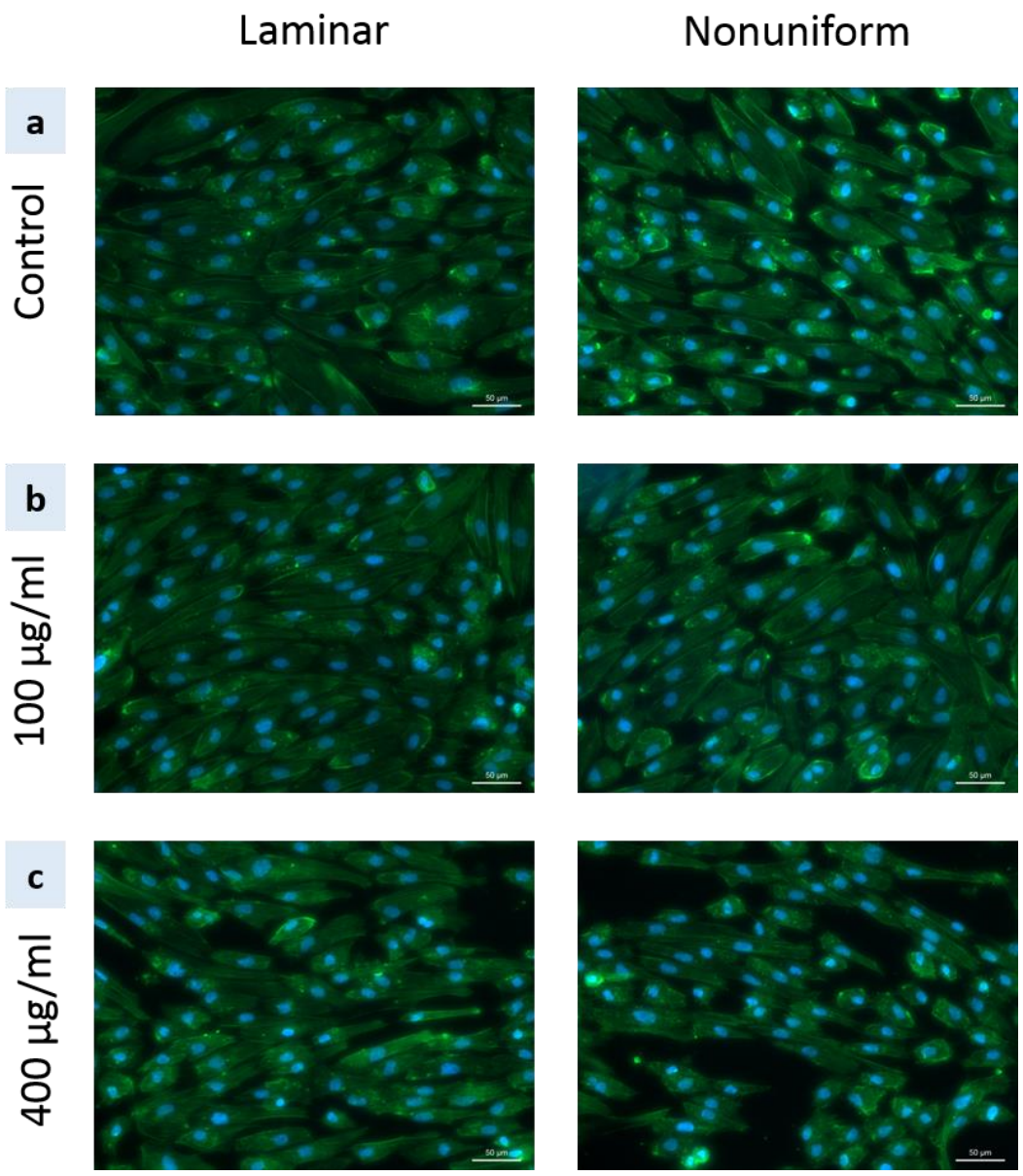

Figure 32: Effects of circulating polyR-magnetite nanoparticles on enthodelial cell grown under flow conditions. HUVECs were grown in bifurcating slides until confluence and perfused with polyR-magnetite nanoparticle-containing medium for 18 h. The representative laminar and non-uniform regions are shown after fluorescent staining. Nuclei are visualized using a Hoechst 33342 (blue) staining, whereas F-actin is visualized with Alexa 488-conjugated phalloidin (green). Representative images of n=3 experiments are shown.

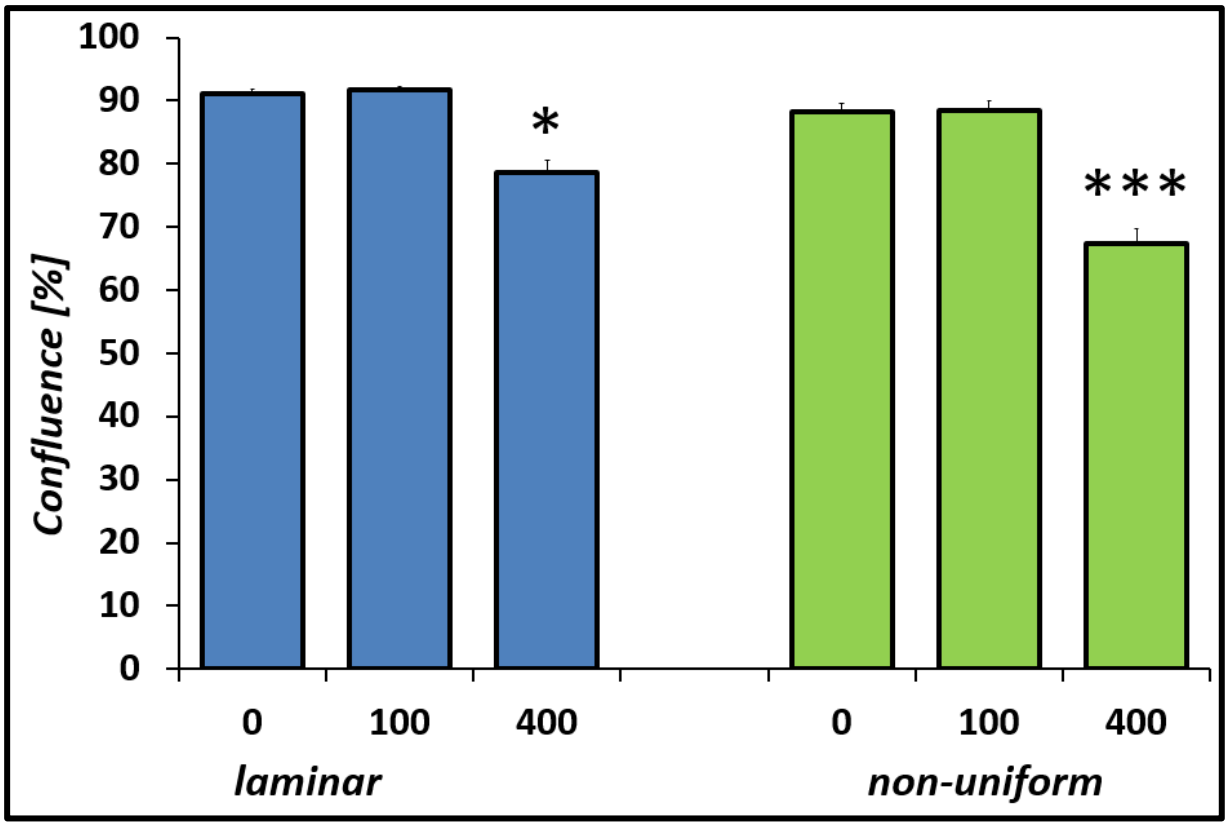

*Figure 33: The graphs show the semi-quantitative analysis of confluence in nonuniform (green) and laminar (blue) according to the fluorescent images of Figure 32, using ImageJ software. n=3, Data are expressed as mean ± SEM, *p<0.05, ** p<0.01, ***p<0.001 vs. corresponding control (one-way Anova).*

3.2.1.3 Discussion

When injecting nanoparticles into the body for diagnosis or therapy, safety has to be guaranteed. PolyR-magnetite nanoparticles exhibit large surface area to volume ratio and therefore, such kind of particles are considered as chemically reactive in comparison to bulk materials (Lee et al., 2015). Undesirable reactions could occur *in vivo*, which depend on the materials composition. Therefore, polyR-magnetite nanoparticles were tested in static and dynamic conditions on a cellular system *in vitro* and did show effects on cells, such as influence in cell adherence and therefore decreasing cell viabilities under static conditions. The proliferation of cells was not affected and cytotoxic effects were only reported when using high nanoparticle concentrations (200 to 400 µg/ml). Consequently, it is shown that polyR-magnetite nanoparticles are non-toxic to a certain concentration in static conditions

and they are comparable to the standard contrast agent Resovist®. However, the experiment for Resovist® was performed only once, thus it has to be interpreted critically.

Dynamic cell experiments were performed, which mimic conditions in blood vessels. The flow of blood and its viscosity constantly creates shear stress within blood vessels. Endothelial cells, being constantly exposed to shear stress, actively respond to biological stimuli, but the type of response differs depending on the shear stress pattern acting on the cells. The laminar flow protects the endothelial cells from harmful stimuli, whereas the non-uniform flow induces the endothelial activation through the created shear stress. The enthodelial uptake of untargeted nanoparticles highly depends on the magnitude and presence of shear stress (Cicha, 2016). Here, it is important to highlight that polyR-magnetite nanoparticle biocompatibility is significantly improved under dynamic conditions as compared to static conditions. Whereas 400 µg/ml were highly toxic under static conditions, only a minor decrease in cell numbers was observed at this concentration under flow. Similarly, no endothelial growth inhibition was observed upon the exposure to 100 µg/ml of circulating polyR-magnetite nanoparticles.

As iron oxide nanoparticles are generally considered to be biocompatible, polyR-magnetite nanoparticles can be included in the list and stated as biocompatible. Earlier *in vivo* experiments showed that isotope labeled iron oxide nanoparticles accumulate in the liver and spleen in rats (Lee et al., 2015). Normally, excess iron ions are incorporated into ferritin proteins for iron detoxification and storage in iron pools. Iron ions are used for various biological processes, such as hemoglobin formation. PolyR-magnetite nanoparticles could be further tested in *in vivo* studies to guarantee safety issues. Flow experiments, which investigate the effects of circulating nanoparticles on endothelial cells, allow monitoring of the real cell response in a physiological-like setting (Cicha, 2016). Additionally, polyR-magnetite nanoparticles are positively charged and showed high cell uptake, which would be also suitable for magnetically hyperthermia and direct tumor therapy. When coating polyR-magnetite nanoparticles with specific antibodies, they could be transported easily due to their strong uptake into tumor cells and attach specific recognition sites of tumor cells (Lee et al., 2015). In chapter 3.3, polyR-magnetite nanoparticle-antibody-conjugates are introduced, which could be the next step to a fruitful biomedical application.

3.2.2 POLYR-MAGNETITE NANOPARTICLES FORM UP AS MRI CONTRAST AGENTS

According to dynamic light scattering (DLS) measurements, polyR-magnetite nanoparticles comprises a hydrodynamic radius of 98 nm (intensity-weighted), which corresponds nicely with the forehand in TEM measured mean nanoparticle diameter of around 38 nm (see chapter 3.1.2). The different radii in DLS originate from the measured solvation layer surrounding the nanoparticles. Moreover, the DLS signal of the different size fractions is weighted by d_h^6, so a small fraction of even large aggregates may overestimate the mean d_h. The hydrodynamic radius does not change significantly over time which indicates good colloidal stability. Colloidal stability is an important feature for MRI contrast agents (see chapter 2.7.1). In Figure 34 the relaxation times T1 and T2 were plotted in a ratio of 1/T1 and 1/T2 and the relaxivity values (R1 & R2) were evaluated through the resulting linear slope. PolyR-magnetite nanoparticles exhibit relaxivity values of R1 = 8.5 and R2 = 145.7 l/mmol*s which yields a R2/R1 ratio of 17.0.

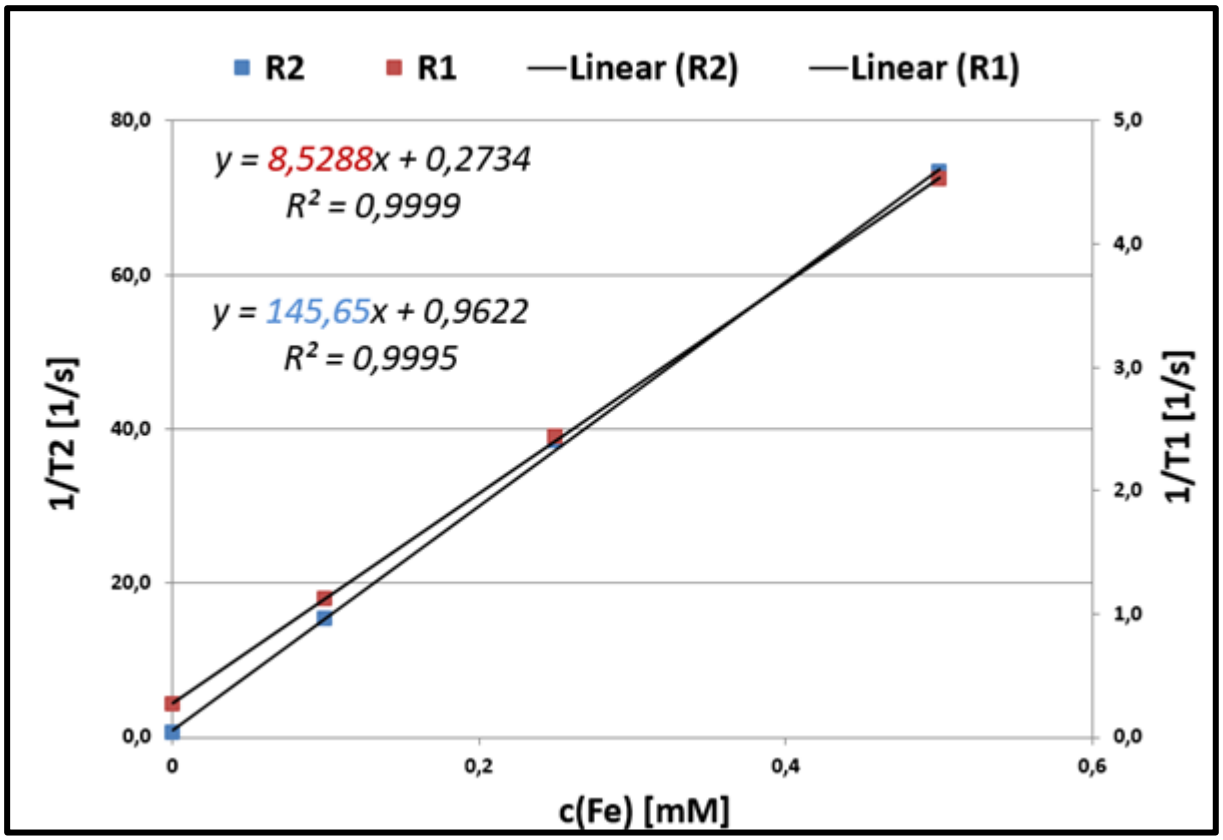

Figure 34: Relationship of the iron concentration c(Fe) in [mM] and the reciprocal of the relaxation time 1/T1,2 in [s-1]. The relaxivities R1 and R2 were calculated via the slope of the obtained linear equation.

3.2.2.1 DISCUSSION

PolyR-magnetite nanoparticles show T2 contrast agent behavior, which is in good agreement that iron oxide nanoparticles are well known for their negative contrast (see chapter 2.7.1). When comparing the results to Resovist ®, a well-known iron oxide based contrast agent which was used in human, but no longer available on the market, Resovist® exhibits relaxivity values of R1 = 20.0 and R2 = 219.3 mM^{-1} s^{-1} which yields a R2/R1 ratio of 11.0 (Taukulis et al., 2015). It is shown, that even though, Resovist® shows larger R1 and R2 relaxivities, the R2/R1 ratio is higher in polyR-magnetite nanoparticles, which is most important for a suitable MRI contrast agent. Furthermore, polyR-magnetite nanoparticles showed comparable biocompatibility to Resovist® (chapter 3.2.1), whereas both are not influencing cell viability when treating endothelial cells with 100 µg/ml. Compared to Ferridex®, another available contrast agent, which exhibit a R2 relaxivity of around 100 mM^{-1} s^{-1}, polyR-magnetite nanoparticles show even higher R2 values (Clement et al., 1998). Interestingly, polyR-magnetite nanoparticles show similar R2/R1 ratios to recently reported L-DOPA stabilized iron oxide nanoparticles (Taukulis et al., 2015). These synthetic samples are SSD, with a significant SP contribution. They range between 16.4 and 19.7 in R2/R1 ratios as well as polyR-magnetite nanoparticles are located in same ranges. Additionally, biogenic samples were recorded recently and showed a very good relaxivity performance. Magnetosomes from *Magnetospirillum gryphiswaldense* were isolated and purified, whereas the magnetosome membrane was still enveloping the nanoparticles, and relaxivities were measured. The magnetosomes exhibit R1 relaxivity values up to 11 mM^{-1} s^{-1} and R2 relaxivity values up to 541.5 mM^{-1} s^{-1} (Taukulis et al., 2015). PolyR-magnetite nanoparticles exhibit far worse R1 and R2 values and show additional worse R2/R1 values of 17. Hence, polyR-magnetite nanoparticles are located in a similar size regime of magnetosomes, but they differ in composition and structure. MRI contrast agent's performance strongly depends on the particle size, composition, state of oxidation and surface state. Therefore, the thickness of the organic coating as well as the organic within the internal particle structure are important. Magnetosomes owe a magnetosomal membrane, which composition is not yet fully discovered. Hence, they do not show a good biocompatibility in comparison to their synthetic antagonists shown by (Taukulis et al., 2015), which composition is well known. Additionally, polyR-magnetite nanoparticles are well known in their composition and they are well characterized, which is described in detail in chapter 3.1, therefore it is suggested

that they remain potentially candidates for MRI contrast agents. Biocompatibility tests of polyR-magnetite nanoparticles are shown in chapter 3.2.1. Our particles do not induce early cell death, whereas they cannot be directly compared with magnetosomes, as they were not applied in dynamic cell studies. Another advantage of polyR-magnetite nanoparticles is that they are already stabilized within the synthesis procedure. In comparison to the prior mentioned synthetic iron oxide nanoparticles, which were electrostatically stabilized after synthesis using L-DOPA (Taukulis et al., 2015), polyR-magnetite nanoparticles are colloidal stable right after synthesis and comprise monodispersity. One has to report that a variety of interesting structures, which great relaxivity performance were published in the recent years. One of the most interesting synthetic contrast agent applicants are water-dispersible ferrimagnetic iron oxide nanocubes encapsulated in PEG-phospholipids, which yield R2 relaxivities up of 761 mM^{-1} s^{-1} and proved to be highly biocompatible. Nevertheless, these new materials were not synthesized in ambient conditions. Hence, they were produced using high temperature synthesis up to 290 °C followed by purification steps and additional encapsulation (Lee et al., 2012). In contrast to that, polyR-magnetite nanoparticles were synthesized using the convenient co-precipitation procedure. MRI contrast agents are not only suitable if they show good R1, R2 relaxivities or R2/R1 ratios. Many additional factors, such as colloidal stability, cellular uptake, blood half-life, cytotoxicity, among others, are important to collude for a nice biomedical nanosystem in clinical use (Lee et al., 2015). In addition, *in vitro* and *in vivo* biocompatibility assays need to guarantee a safe system in medical trials. In ongoing preclinical studies a variety of potential new contrast agents are tested (Lee et al., 2015).

3.2.3 PERFORMANCE OF POLYR-MAGNETITE NANOPARTICLES IN HYPERTHERMIA

To evaluate polyR-magnetite nanoparticles for their possible application in magnetic hyperthermia, the specific loss power (SLP) of polyR-magnetite nanoparticles was measured and yields 208 W/g, recorded at 410 kHz, (altering field frequency) and 25 kA/m (magnetic field strength).

3.2.3.1 DISCUSSION

As the SLP is proportional to the saturated magnetization, it depends strongly on the saturation magnetization and the magnetic anisotropic constant of the nanoparticles (see chapter 2.7.2). Magnetic nanoparticles dissipate heat in response to an altering magnetic field with suitable frequency and amplitude. Magnetic relaxation loss can result in heating, such as magnetic particles relax either with the Néel and/or the Brownian mechanism. The magnetic moment is locked according to the crystal axis and the particle wants to rotate in order to align with the field, explained by the Brownian mechanism, whereas the magnetic moment rotates within the crystal described by the Néel mechanism. Thus, in both cases, magnetic work is transferred into internal energy, which is actually heat, conveys to its surrounding environment. The SSD magnetite nanoparticles released energy is corresponding to a hysteresis loop and it is described that the dissipated heat of a magnetite nanoparticle is contingent upon its size and composition but furthermore upon the frequency and temperature of the applied field (Chiu-Lam and Rinaldi, 2016).

Since, the SLP highly depends on field strength and frequency, one has to be careful when comparing different SLP of different particles systems from literature, as they are not always recorded with the same magnetic field strengths and frequency, thus our polyR-magnetite nanoparticles solely exhibit a SLP of 123 W/g when using 210 kHz instead of 410 kHz and 25 kA/m, which is half of the magnetic field frequency and correspond to almost half the of SLP rate.

To achieve a high SLP, a highly monodispersity of particles has to be guaranteed, which is definitely the case for polyR-magnetite nanoparticles. The polyR-mesocrystals consist of mean particle diameters of ~ 38 nm, which is in good agreement with preferably mean diameters for hyperthermia between 20 and 50 nm (Gazeau et al., 2008). On the other hand, it was shown that intact bacteria cells of *Magnetospirillum magneticum* strain AMB-1 exhibit

SLP values around 800 W/g, whereas the purified magnetosomes reaches values up to 1 k W/g at 410 kHz and 10 kA/m (Rudolf et al., 2006). Even though our polyR-magnetite nanoparticles were recorded with the same field frequency but with within a stronger magnetic field strength, they still owe lower SLP than magnetosomes. Magnetosomes are located in the same size regime than polyR-magnetite nanoparticles and consist of similar magnetic properties, such as SSD magnetic behavior. They are similarly structured in chain formation and show highly monodispersity. Hence, magnetosomes do not exhibit mesocrystalline structures of their individual nanoparticles as prior discussed in chapter 3.2.1. Dartmouth particle's, similar to mesocrystalline polyR-magnetite nanoparticle size and shape, were shown recently, and exhibit SLP values of 120 W/g at 16 kA/m (Shubitidze et al., 2015), which shows almost half of the obtained SLP of mesocrystalline polyR-magnetite nanoparticles, thus also the magnetic field strength is halved. Additionally, 11 nm maghemite nanoflowers were synthesized using the time consuming polyol method under heat. SLP values of 1175 W/g at 700 kHz and 21.5 kA/m were recorded. Interestingly, these nanoflowers show good SLP, thus their small sizes in comparison to e.g. magnetosomes, though magnetosomes were just measured at 410 kHz and 10 kA/m. It would be interesting to measure magnetosomes at the same magnetic field frequencies and strengths to really compare these results. Pure 11 nm co-precipitated maghemite nanoparticles solely owe the SLP of 110 W/g at 700 kHz and 21.5 kA/m (Hugounenq et al., 2012). Prior mentioned PEG-conjugated nanocubes, used for possible MRI contrast agents, were also tested regarding their SLP and achieved up to 1792 W/g. Nanocubes were further coated with chitosan-DOPA residues and reached a SLP up to 2614 W/g (Bae et al., 2012). This yields in a 30 times higher SLP than Feridex® (Bae et al., 2012). However, their synthesis method is not ideal. Our polyR-magnetite nanoparticles achieve 2.5 times higher SLP than Feridex® with 83 W/g (Bae et al., 2012). In recent years, a variety of nanoparticles were tested for hyperthermia, especially maghemite and magnetite nanoparticles. The first particles are already clinically approved in Europe for the treatment of glioblastoma. Therefore, magnetite nanoparticles encapsulated in cationic liposomes were used (Lee et al., 2015). Cationic additives are good choices for biomedical applications. Due to the negatively charged cell membranes, particles with positively charged coatings are prone for the cell uptake. PolyR-magnetite nanoparticles are highly positive charged and therefore nice candidates for *in vitro* and *in vivo* studies. Additionally, polyR-magnetite nanoparticles exhibit chain formation. It was

shown recently, that magnetosomes perform better in hyperthermia, due to their chain structures than single nanoparticles (Alphandery et al., 2011). The smaller the chosen field amplitudes were defined, the larger chain sizes should be chosen for a sufficient heating effect (Serantes et al., 2014). Therefore, the therapy effect can be tuned with particle chain lengths. The polyR-magnetite nanoparticle chain length is tunable with polyR-magnetite nanoparticle growth over time.

3.3 FORMATION OF ORDERED MATERIALS BASED ON POLYR-MAGNETITE NANOPARTICLES

PolyR-magnetite nanoparticles are covered by polyR (Figure 35), which is an possible linker for different antibodies using click chemistry and create a new building block for multifunctional assemblies as reported recently (Jehle et al., 2016). Two different antibodies (one consists of an anti-His_6-Tag recognition site and the other consist of an anti-mCherry recognition site) for bio-conjugation onto polyR-magnetite nanoparticles were chosen. Both antibodies belong to the family of immunoglobulins (IgG antibodies), containing antigen binding sites (anti-His_6-Tag and anti-mCherry), protein A binding regions, light and heavy chains with their corresponding light-chain and heavy-chain hypervariable regions. They consist of hinge regions, intra-chain and inter-chain disulfides and exhibit glycosylation sites between their heavy chains (Hermanson, 2013b). Hence, one can imagine that these numerous functional groups of the IgG antibody exhibit various possibilities for bio-conjugation. A crosslinking reaction was performed via EDC and NHS carbodiimide coupling of the amino groups of polyR-magnetite nanoparticles to the carboxyl groups of the IgG heavy chains (Grabarek and Gergely, 1990). In case of polyR-magnetite nanoparticles, the poly-arginine guanidino groups bound to the magnetite particles, thus, excess guanidine-groups and additionally primary amines supposed to be presented on particle surfaces for further conjugation.

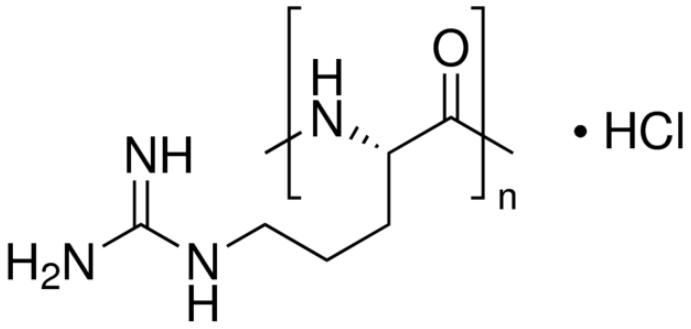

Figure 35: Poly-l-arginine (PolyR) (Sigma-Aldrich)

3.3.1 ANTI-HIS$_6$-TAG ANTIBODY CONJUGATED POLYR-MAGNETITE NANOPARTICLES

Immunogold conjugate monoclonal anti-His$_6$-Tag antibodies were conjugated to polyR-magnetite nanoparticles, using EDC/NHS coupling. PolyR-magnetite nanoparticles with closely located Immunogold nanoparticles are observed when deposited on TEM grids (Figure 36a, b). PolyR-magnetite nanoparticles can be easily distinguished from immunogold nanoparticles in TEM measurements as they form chain structures and comprising mesocrystallinity. Even though, Immunogold nanoparticles have the same size than polyR-magnetite nanoparticles, they differ strongly in their appearance, as they show a stronger mass contrast in TEM. The close location of both, magnetite and Immunogold nanoparticles indicates a possibly antibody coupling between polyR-magnetite nanoparticles and Immunogold conjugate monoclonal anti-His$_6$-Tag antibodies. After washing, using a strong magnet, Immunogold nanoparticles were solely found close to polyR-magnetite nanoparticle chains. Unbound rest-immunogold particles were detected in the supernatant.

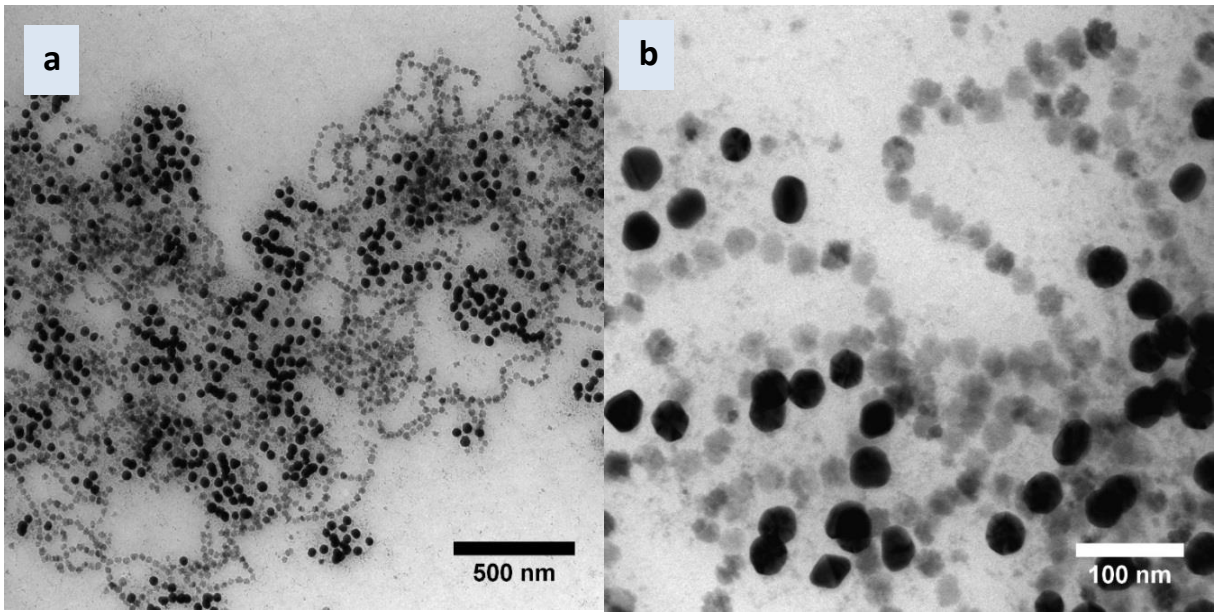

Figure 36: TEM images in different magnifications of polyR-magnetite nanoparticle pellets, incubated with Immunogold conjugate monoclonal anti-His6-Tag antibodies (40nm) using the EDC/NHS coupling.

3.3.2 ANTI-MCHERRY ANTIBODY CONJUGATED POLYR-MAGNETITE NANOPARTICLES

The following BF and HAADF STEM measurements were performed by our collaborators Prof. Dr. Richard Wirth and Anja Schreiber at the GFZ (German Research Center for Geoscience/Helmholtz Centre) in Potsdam, Germany. Anti-mCherry antibodies (+Alexa488) were conjugated to polyR-magnetite nanoparticle chains as reported for Immunogold conjugate monoclonal anti-His_6-Tag antibodies (see chapter 3.3.1) using EDC/NHS coupling. Due to the fluorescent dye Alexa 488, which is bound to the anti-mCherry antibody, the antibody decorated magnetite nanoparticles can be detected using fluorescence microscopy. When applying a magnetic field, the rotation of PolyR-magnetite nanoparticles (Figure 37a) and the additional fluorescence signal of the bound anti-mCherry antibodies (+Alexa488) while rotating is detected (Figure 37b).

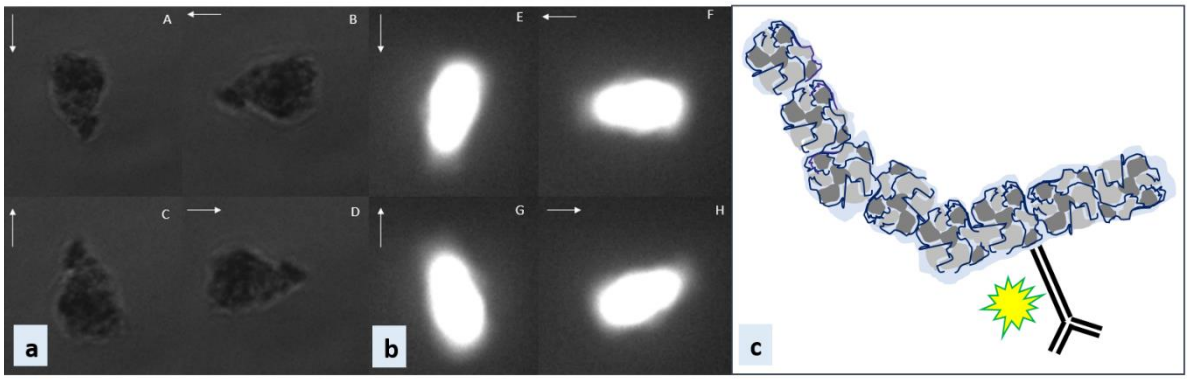

Figure 37: Actuation of polyR-magnetite nanoparticle fluorescence antibody constructs. (a) Rotating polyR-magnetite nanoparticles within an applied magnetic field (3.5 mT). (b) Recording of the fluorescence signal of anti-mCherry antibodies+Alexa488 conjugated to polyR-magnetite nanoparticles while rotating them in the applied magnetic field (3.5 mT). The emission was recorded through a longpass filter using a sCMOS camera. (c) Scheme of an anti-mCherry antibody (+Alexa488) - polyR-magnetite nanoparticle - chain conjugate.

MamK_mCherry_His_6 filaments were purified using an immobilized metal ion affinity chromatography, after the recombinant fusion protein MamK_mCherry_His_6 was expressed in *E.coli* (Carillo, 2014). Whereas MamK is an actin-like filament isolated from magnetotactic bacteria and assembles the scaffold for magnetosome chains (see chapter 2.1.4). Anti-

mCherry antibodies (+Alexa488) were conjugated to polyR-magnetite nanoparticle chains, which bound to MamK_mCherry_His_6 filaments due to the anti-mCherry interaction with mCherry (Jehle et al., 2016 46). PolyR-magnetite nanoparticles are observed in close proximity to MamK_mCherry_His_6 filament bundles (Figure 38a, b), when deposited on TEM grids. A distribution of polyR-magnetite nanoparticles along the filament is not observed due to their assembly in chain structures (Figure 39a).

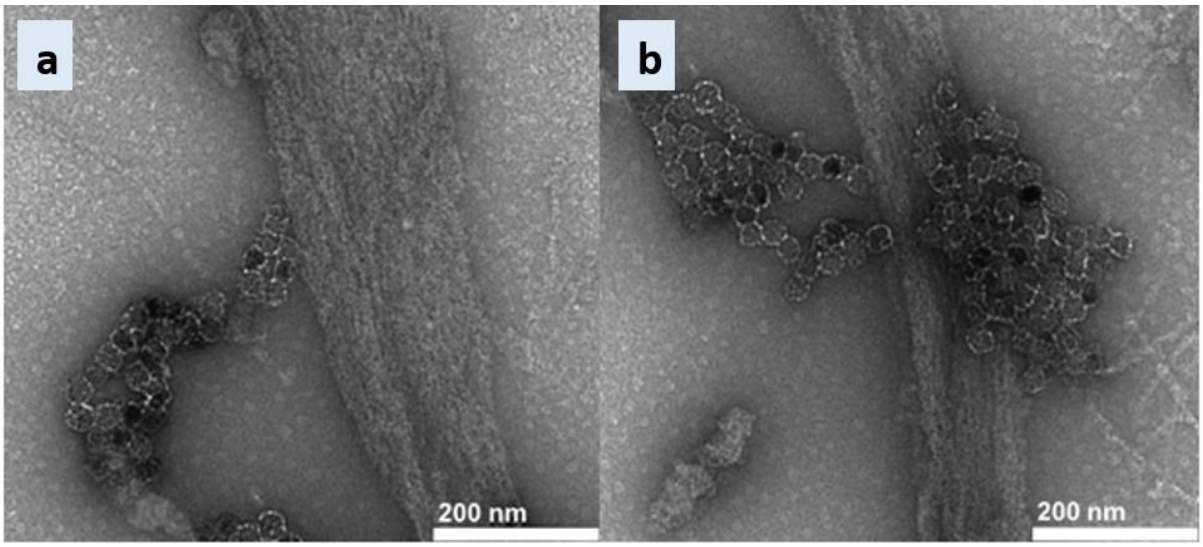

Figure 38: (A & B) TEM images of MamK_mCherry_His_6 filament bundles incubated with polyR-magnetite nanoparticles functionalized with anti-mCherry antibodies.

Additionally, a HAADF STEM image of polyR-magnetite nanoparticle chains decorated with anti-mCherry antibodies attached to MamK_mCherry_His_6 filaments is shown (Figure 39b). EDXS shows intense peaks of iron (Fe) and thereby the presence of polyR-magnetite nanoparticle chains to be attached to MamK_mCherry_His_6 filaments is confirmed (Figure 39c). The additional peaks of copper (Cu), carbon (C) and uranium (U) originate from the carbon film on the copper TEM grids and used uranyl acetate for staining.

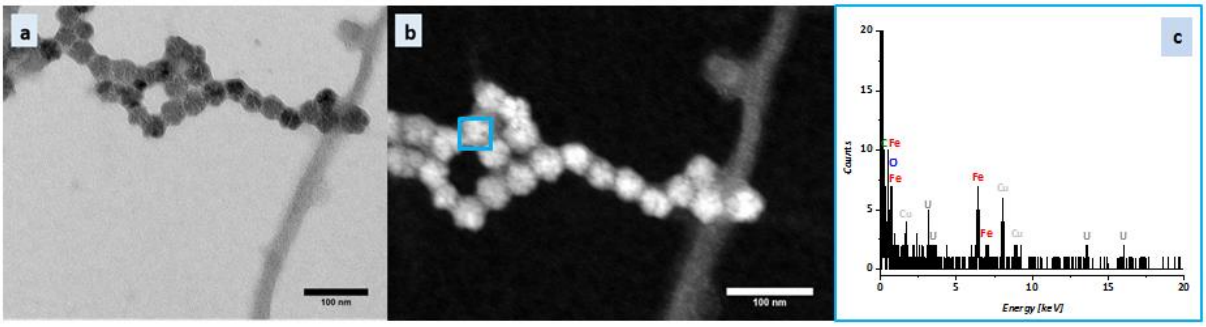

Figure 39: (a) BF TEM images of MamK_mCherry_His$_6$ filament bundles with attached chain-structures of polyR-magnetite nanoparticles prior decorated with anti-mCherry antibodies. (b) HAADF STEM image of chain-structures of polyR-magnetite nanoparticles prior decorated with anti-mCherry antibodies attached to MamK_mCherry_His$_6$ filaments were analyzed using EDXS (blue area). (c) EDXS analysis of the boxed area in (b) shows element specific peaks. X-axis: Energy of detected X-ray quanta in keV. Y-axis: Signal intensity in counted X-ray quanta (counts). Modified from (Jehle et al., 2016) with permission of Advanced Materials Interfaces.

In order to activate MamK_mCherry_His$_6$ filaments prior decorated with chain-structures of polyR-magnetite nanoparticles, a magnet was placed closed to the sample and an image was recorded (Figure 40a). The magnet was moved around the sample area by 90 degrees and the images in Figure 40b were recorded after. It is possible to observe the rotation of filaments due to prior binding of polyR-magnetite nanoparticles.

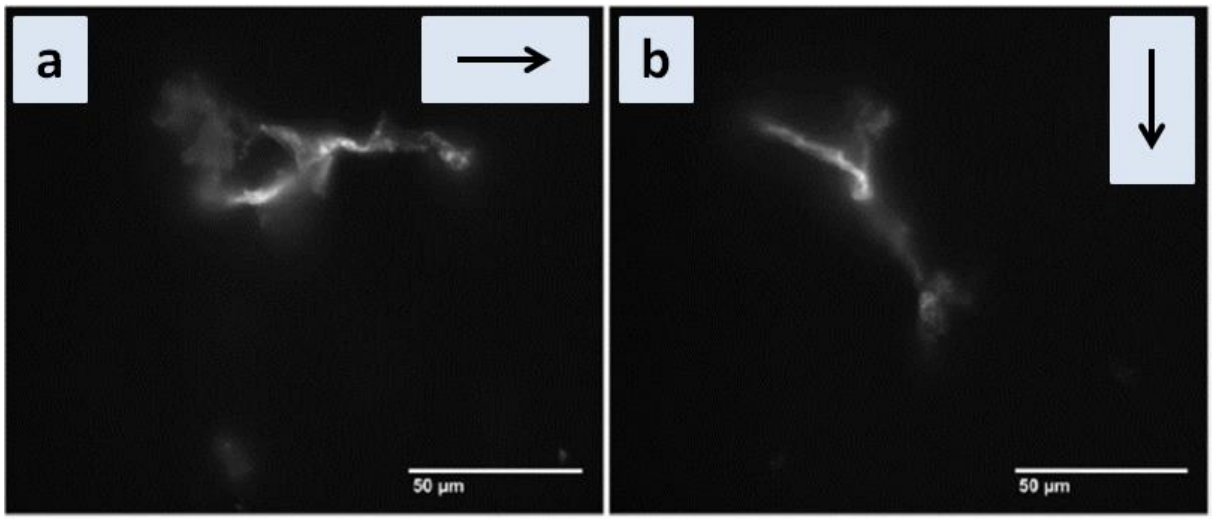

Figure 40: Actuation of polyR-magnetite nanoparticle decorated with anti-mCherry antibodies (+Alexa488), attached to MamK_mCherry_His6 filaments. The multifunctional biomimetic assembly

was subjected to a rotating magnetic field of around 15 mT and imaged by fluorescence microcopy using excitation at 565 nm. The emission was recorded using a longpass filter of 600 nm with a sCMOS camera. The arrows show the applied magnetic field directions (Jehle et al., 2016). Modified from Jehle (Jehle et al., 2016) with permission of Advanced Materials Interfaces.

3.3.3 DISCUSSION

The EDC/NHS reaction to either conjugate Immunogold (40 nm) conjugate monoclonal anti-His_6-Tag antibodies or anti-mCherry antibodies (+ Alexa Fluor® 488 dye) on poly-l-arginine regions of polyR-magnetite nanoparticles was performed. PolyR-magnetite nanoparticles and Immunogold nanoparticles from Immunogold conjugate monoclonal anti-His_6-Tag antibodies appear in close proximity to each other, visualized through TEM imaging. Furthermore, after separation of magnetic particles with a strong magnet, Immunogold nanoparticles were still observed close to the magnetic nanoparticles. Additionally, the antibody-nanoparticle construct of anti-mCherry antibodies (+Alexa488) conjugated to polyR-magnetite nanoparticles, was verified through a fluorescent signal of rotating polyR-magnetite nanoparticles within an applied magnetic field. Due to the nanoparticle`s gained fluorescence of anti-mCherry antibodies (+Alexa488), they provide additional functionality besides their magnetic properties.

Additionally, the anti-mCherry-polyR-magnetite nanoparticles were used to conjugate onto polymerized MamK_mCherry_His_6 filaments (Jehle et al., 2016). MamK_mCherry_His_6 filaments offer a template, on which different kind or nanoparticles can be attached. Due to the new gained recognition side of polyR-magnetite nanoparticles functionalized with anti-mCherry antibodies, polyR-magnetite nanoparticles exhibit a suitable fusion partner to the mCherry recognition sites of the filament. Furthermore, as the filament also consist of a hexahistidine tag, anti-His_6-Tag antibodies decorated polyR-magnetite nanoparticles conjugated with anti-His_6-Tag antibodies could act as a further possible fusion partner for the filament. However, anti-mCherry-conjugated polyR-magnetite nanoparticle chains do not properly align on the filament.

A reason could be unspecific binding of antibodies to polyR-magnetite nanoparticles or to each other through inappropriate crosslinking within the EDC/NHS reaction. Thus, the antigen binding site (anti-mCherry) could be blocked by other antibodies or miss aligned on

the particle, which lead to an decrease in antigen binding activity compared to unconjugated antibodies. PolyR-magnetite nanoparticles might be fully covered with antibodies but only a small conjugated antibody fraction is functional. For this reason, only a small fraction of antibodies is able to interact with the antibody recognition sites of the MamK_mCherry_His_6 filament and therefore polyR-magnetite nanoparticle chains cannot bind completely to the filament. To improve the antibody-nanoparticle conjugation, different cross linking reactions could be investigated. One example are two site-directed reactions which help to avoid unspecific binding (Hermanson, 2013a). The heavy chains of antibodies are connected via disulfide bonds in the hinge region of IgG and can be cleaved with a reducing agent, such as DDT. Thiols revel within the antibody and thiol reactive crosslinking with created free sulfhydryl groups is used for conjugation. Most likely, thiol containing antibodies could be also conjugated with our polyR-magnetite nanoparticles via a heterobifunctional Sulfo-SMCC crosslinker (sulfosuccinimidyl-4-(N-maleimidomethyl)-cyclohexane-1-carboxylate) which contains an amine reactive NHS ester, most likely reactive with polyR of our particles, and a thiol reactive maleimide group. The maleimide group forms a stable thioester linkage with the sulfhydryl containing antibody (Hermanson, 2013a).

Nevertheless, polyR-magnetite nanoparticles were bound to the filament and can further be optimized with prior mention cross linking strategies or by varying antibody and particle concentrations. However, these template-based *in vitro* formed structures and their fluorescent and magnetic functionalities can be used for various applications such as protein interaction studies, through florescent probes (Carillo et al., 2013). The functionalized biomimetic chain could be useful for biomedical applications, as extracted magnetosome chains show antitumoral activity when exposed to an alternative magnetic field (Philipse and Maas, 2002). Solely polyR-magnetite nanoparticle chains are biocompatible, whereas it would be interesting, if they keep their biocompatibility when conjugated with specific antibodies. Moreover, polyR-magnetite nanoparticle-antibody conjugates could be further used in order to track cancer cells. Biomimetic templating strategies were reported in recent years. However, they were only used for nucleation and organization of particles, in another fashion than MamK_mCherry_His_6 decorated filaments with polyR-magnetite nanoparticles. Several biomimetic templating strategies, using peptides or proteins (Meldrum et al., 1992), (Huggins et al., 2014) were introduced. In a study from (Huggins et al., 2014), the protein chlatrin self assembles into spherical cages forming scaffolds within inorganic species were

synthesized. Another publication shows, that a genetically engineered variant of human ferritin, was fused to a silver binding peptide, which was used to further form a template for synthesize silver nanoparticles (Meldrum et al., 1992). Nevertheless, the chemically stability of the template is limited, thus the synthesis of silver particles requires harsh chemicals, high temperature and it is not performed under physiological conditions. Linear arrangements of magnetite nanoparticles onto filamentous structures were mimicked by (Sone and Stupp, 2004), using amphiphilic peptides which self-assemble into fibers and nanoparticle nucleation and growth was again directly carried out on the fiber. In contrast to prior mentioned studies, we performed a three step process, whereas first polyR-magnetite nanoparticles are forehand fabricated without extra limitations in terms of composition, size and surface properties, secondly, particles are conjugated to prior selected specific antibodies and thirdly the antibody-particle construct binds to the antibody recognition sites of MamK_mCherry_His_6 filaments. It was further shown, that it is possible to decorate MamK_mCherry_His_6 filaments with magnetosomes and gold particles simultaneously. Compared to the MamK_mCherry_His_6 filaments decorated with polyR-magnetite nanoparticles, the magnetosomes show proper alignment on the MamK_mCherry_His_6 filaments, due to their red binding protein (RBP)-recognition sites interacting with mCherry of MamK_mCherry_His_6 filaments and it is equally distributed over the magnetosome chain (Jehle et al., 2016).

4. CONCLUSION

A magnetic nanoparticle system was introduced, which shows a variety of properties, useful for further applications.

4.1 POLYR-MAGNETITE NANOPARTICLES: STRUCTURE, MAGNETIC PROPERTIES AND FORMATION MECHANISM

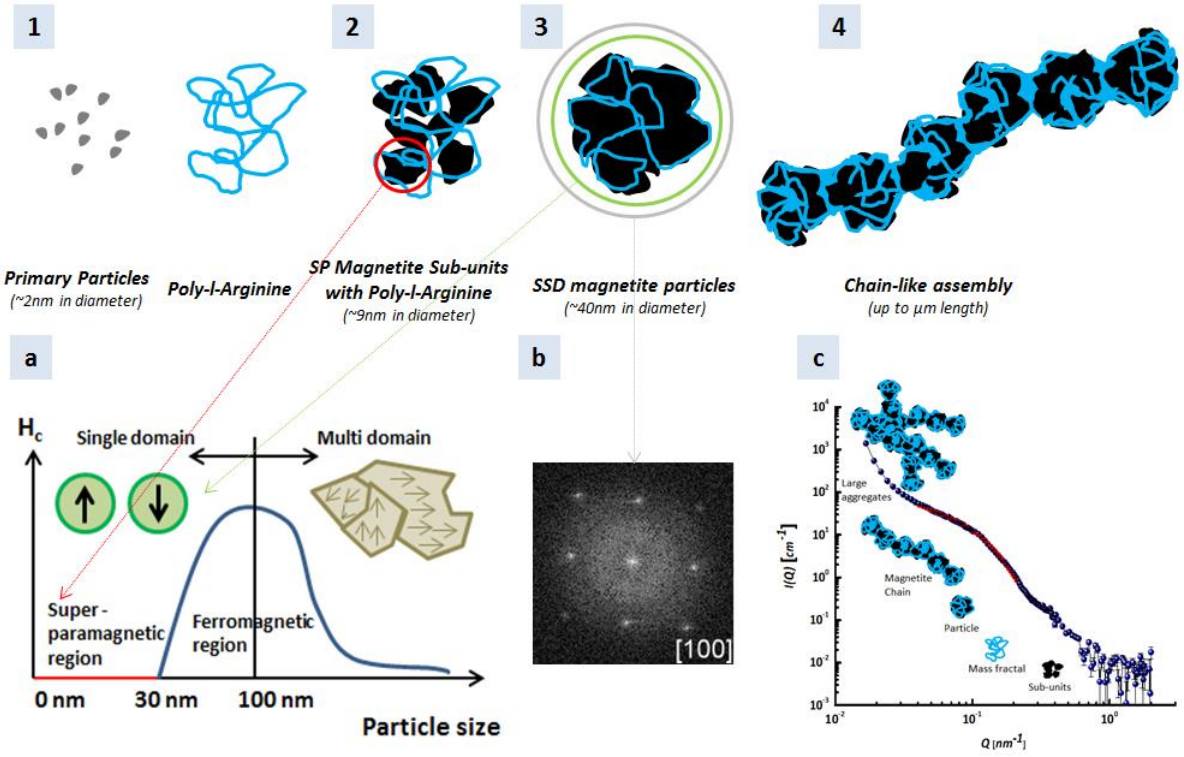

Figure 41: Schematic diagram of the formation mechanism of SSD mesocrystalline polyR-magnetite nanoparticles made from SP sub-units and their ability to form chain structures. The steps involve: (1) Formation of initial primary particles and their agglomeration, result in (2) nucleation of 9 nm magnetite sub-units. (3) These sub-units are assembled into the larger polyR-magnetite nanoparticles with the help of the additive and (d) assemble into chains, possibly originating from the fact that (a) each particle exhibits SSD magnetic behavior. (b) PolyR-magnetite nanoparticles diffract as single crystals. (c) SANS slope showing all structural components of the nanosystem, whereas especially the mass fractal indicates organic inclusions within sub-units.

The work presented in this thesis, showed that 40 nm magnetite nanoparticles can be synthesized in the presence of polyR, which is responsible for the polyR-magnetite nanoparticle`s monodispersity, shape and does introduce colloidal stability to the nanosystem. Each 40-nm polyR-magnetite nanoparticle is a real mesocrystal, comprising single crystallinity, exhibit stable single domain magnetic behavior, and its structural and magnetic properties are determined by the size of the superstructure rather than that of its components.

A three-stage process of polyR-magnetite nanoparticle formation is shown in Figure 41, whereby the (1) primary particles first form and then assemble into (2) magnetite sub-units with sizes of approximately 9 nm, as observed in experiments without additives (Baumgartner et al., 2013b). The latter size agrees well with the sizes of the sub-units shown in (3) the larger 40 nm particles. Chain formation occurs, thus it is most likely the consequence of the magnetic single-domain behavior of the particles.

As the mesocrystals consist of sub-units, EDXS, TGA and HRTEM studies were performed to analyze the organic fraction within the entire mesocrystal. Hence, the organic part is located around larger mesocrystalline nanoparticles but additionally it was shown that polyR is most likely located within the sub-units of each mesocrystal confirming the hypothesis of polyR assembling sub-units of magnetite to form large nanoparticles.

To verify this hypothesis, small angle neutron scattering (SANS) experiments were performed. Therefore, polyR-magnetite nanoparticles were synthesized using different iron isotopes in order to vary the scattering length density of the material for contrast variation experiments. Interestingly, polyR-^{57}magnetite nanoparticles show smaller mean sizes than polyR-magnetite nanoparticles, as well as ^{57}magnetite nanoparticles exhibit smaller diameters than magnetite nanoparticles.

The obtained SANS slopes of measured polyR-magnetite nanoparticles as well as polyR-^{57}magnetite nanoparticles exhibit all structural components as it was analyzed in TEM before. The most important observation of the prior SANS plots is a Q value which corresponds to a structure called “mass fractal”. This structure is located in the Q regime of the polyR-magnetite mesocrystals at a power law of Q^{-3}. It corresponds to gap-structures which are not highly dense packed and most likely filled with organic. Thus, it is suggested to be the proof for the location of polyR within polyR-magnetite nanoparticles.

Additionally, contrast variation experiments of polyR-^{57}magnetite nanoparticles in comparison to ^{57}magnetite nanoparticles were performed to further analyze the organic part of polyR-magnetite nanoparticles. Therefore, the isotope nanoparticles were tried to invisibly render within SANS measurements using so called match point solutions of D_2O and H_2O mixtures. Thus, when measuring polyR-^{57}magnetite nanoparticles in a (D_2O: H_2O of 67,3 %: 32,7% mixture), the inorganic part should be invisible rendered to solely record the organic fraction. A remaining signal from imperfectly matched contrast occurred in both particle samples but an upper limit for the amount of organics can be defined with this result, containing of little material, confirming the TGA results. Anyhow, it was possible to show the presence of the organic according to the prior mentioned mass fractal.

4.2 POLYR-MAGNETITE NANOPARTICLES AS POTENTIAL MEDICAL TOOLS

PolyR-magnetite nanoparticles are suitable for applications regarding to their structural and magnetically properties and additional chain formation. Interestingly, polyR-magnetite nanoparticles are non-toxic up to 100 µg/ml in static cell viability assays using human endothelial cells and they are comparable to the standard contrast agent Resovist®. It is important to highlight that the biocompatibility of polyR-magnetite nanoparticles is significantly improved under dynamic cell viability tests as compared to static conditions. Whereas 400 µg/ml were toxic under static conditions, only a minor decrease in cell numbers was observed at same concentrations under flow. Similarly, no endothelial growth inhibition was observed upon the exposure to 100 µg/ml of circulating polyR-magnetite nanoparticles.

Thus, polyR-magnetite nanoparticles exhibit similar biocompatibility compared to the standard contrast agent Resovist®, they are potentially candidates for MRI contrast agents. Furthermore, they showed better performance than Resovist® according to their R2/R1 ratios of 17, whereas Resovist® achieves R2/R1 ratios of 11. Hence, polyR-magnetite nanoparticles are not comparable with their biogenic counterparts, the magnetosomes; still, they show advantages in faster synthesis compared to time-consuming growth of biogenic magnetite nanoparticles.

Additionally, polyR-magnetite nanoparticles were tested towards their potential heating properties in hyperthermia, thus they exhibit SAR rates of 208 W/g, which shows a five times

better heating than that of a standard material Ferridex®. However, magnetosomes show five times higher SAR ratios than polyR-magnetite nanoparticles and are currently the best choice for hyperthermia in terms of heating. Thus, our polyR-magnetite nanoparticles are produced using green synthesis in comparison to other nanoparticles. Therefore, they are still compatible candidates for hyperthermia or MRI contrast agents.

4.3 FORMATION OF ORDERED MATERIALS BASED ON POLYR-MAGNETITE NANOPARTICLES

PolyR-magnetite nanoparticles were successfully conjugated with two different antibodies to introduce further functionalities onto nanoparticles. Thus, anti-mCherry-antibody conjugated polyR-magnetite nanoparticles were used to bind MamK_mCherry_His_6 filaments in order to create biomimetic multifunctional structures. As a biomimetic construction of magnetosome chains was desired, however, polyR-magnetite nanoparticle chains do not properly align along the filament. Hence, a hierarchical structure with various functionalities, such as magnetic and fluorescent properties was created. These post-synthetically assembly strategy exhibits various building blocks, which can be varied according to desirable applications.

5. OUTLOOK

In the future, SANS data from polyR-magnetite nanoparticles will further be analysed and a model will be applied, which should help to conclude the overall structure of the nanosystem. Additionally, recorded SANS data of magnetosomes will be compared with the synthetic chain structures of polyR-magnetite nanoparticls. Furthermore, different structural features could be applied to the model, thus magnetosomes are core-shell nanoparticles in contrast to mesocrystalline polyR-magnetite nanoparticles comprising the mass fractal.

PolyR-magnetite nanoparticles, which were synthesized in the presence of an iron isotope (^{57}Fe), exhibited smaller particle sizes; however the mesocrystalline structure of the particles remained. Therefore, different stable iron isotopes could be investigated during polyR-magnetite nanoparticle synthesis to establish a size dependend model system with comprising similar properties, such as monodispersity and colloidal stability. Hence, the magnetic behavior may change due to their smaller particle sizes.

Therefore, relaxivity measurements of the smaller polyR-magnetite nanoparticles could be performed and they may show a better performance in MRI than the large polyR-magnetite nanoparticles, synthesized without ^{57}Fe.

An additional candidate for biomedical applications is the multifunctional MamK_mCherry_His_6 biomimetic structure. Magnetite nanoparticles are linked to the elongated filaments and therefore the biomimetic structure may exhibit higher specific absorption rates due to anisotropic assemble in hyperthermia. However, the antibody-particle conjugation strategies have to be improved to equally distribute polyR-magnetite nanoparticle chains along the filament.

A comprehensive study could be operated in terms of biocompatibility, relaxivity for potential MRI contrast agents and heating capacity for hyperthermia, comparing different structures, such as magnetosomes from MTB, polyR-magnetite nanoparticle chains and the biomimetic multifunctional assembly.

REFERENCES

Acton, G., 2011. Essentials of Paleomagnetism. Eos, Transactions American Geophysical Union, 92(19): 166-166.

Aizenberg, J., Black, A.J., Whitesides, G.M., 1999. Oriented Growth of Calcite Controlled by Self-Assembled Monolayers of Functionalized Alkanethiols Supported on Gold and Silver. Journal of the American Chemical Society, 121(18): 4500-4509.

Alphandery, E., Faure, S., Seksek, O., Guyot, F.o., Chebbi, I.n., 2011. Chains of magnetosomes extracted from AMB-1 magnetotactic bacteria for application in alternative magnetic field cancer therapy. ACS nano, 5(8): 6279-6296.

Amor, M. et al., 2016. Mass-dependent and-independent signature of Fe isotopes in magnetotactic bacteria. Science, 352(6286): 705-708.

Annett, F.A., 1921. Electrical machinery: a practical study course on installation, operation and maintenance. McGraw-Hill book Company, Incorporated.

Arakaki, A., Webb, J., Matsunaga, T., 2003. A novel protein tightly bound to bacterial magnetic particles in Magnetospirillum magneticum strain AMB-1. Journal of Biological Chemistry, 278(10): 8745-8750.

Bae, K.H. et al., 2012. Chitosan oligosaccharide-stabilized ferrimagnetic iron oxide nanocubes for magnetically modulated cancer hyperthermia. ACS nano, 6(6): 5266-5273.

Bahareh, K., Damien, F., Stefan, K., 2015. Elastic properties of magnetosome chains. New Journal of Physics, 17(4): 043007.

Banc, A. et al., 2016. Small angle neutron scattering contrast variation reveals heterogeneities of interactions in protein gels. Soft Matter, 12(24): 5340-5352.

Baronzio, G.F., Hager, E.D., 2008. Hyperthermia in cancer treatment: a primer. Springer Science & Business Media.

Barreira, S.V., Silva, F., 2003. Surface modification chemistry based on the electrostatic adsorption of poly-L-arginine onto alkanethiol modified gold surfaces. Langmuir, 19(24): 10324-10331.

Bartczak, D., Kanaras, A.G., 2011. Preparation of peptide-functionalized gold nanoparticles using one pot EDC/sulfo-NHS coupling. Langmuir, 27(16): 10119-10123.

Baumgartner, J., Antonietta Carillo, M., Eckes, K.M., Werner, P., Faivre, D., 2014. Biomimetic magnetite formation: from biocombinatorial approaches to mineralization effects. Langmuir, 30(8): 2129-2136.

Baumgartner, J., Bertinetti, L., Widdrat, M., Hirt, A.M., Faivre, D., 2013a. Formation of magnetite nanoparticles at low temperature: from

superparamagnetic to stable single domain particles. PloS one, 8(3): e57070.
Baumgartner, J. et al., 2013b. Nucleation and growth of magnetite from solution. Nature materials, 12(4): 310-314.
Baumgartner, J. et al., 2012. From magnetotactic bacteria to hollow spirilla-shaped silica containing a magnetic chain. Rsc Advances, 2(21): 8007-8009.
Bazylinski, D.A., Frankel, R.B., 2004. Magnetosome formation in prokaryotes. Nat Rev Micro, 2(3): 217-230.
Bindschedler, S., Cailleau, G., Verrecchia, E., 2016. Role of Fungi in the Biomineralization of Calcite. Minerals, 6(2): 41.
Black, J., 2005. Biological performance of materials: fundamentals of biocompatibility. CRC Press.
Bourrinet, P. et al., 2006. Preclinical Safety and Pharmacokinetic Profile of Ferumoxtran-10, an Ultrasmall Superparamagnetic Iron Oxide Magnetic Resonance Contrast Agent. Investigative Radiology, 41(3): 313-324.
Byrom, J., Han, P., Savory, M., Biswal, S.L., 2014. Directing assembly of DNA-coated colloids with magnetic fields to generate rigid, semiflexible, and flexible chains. Langmuir, 30(30): 9045-9052.
Cabrera, L., Gutierrez, S., Menendez, N., Morales, M., Herrasti, P., 2008. Magnetite nanoparticles: electrochemical synthesis and characterization. Electrochimica Acta, 53(8): 3436-3441.
Cai, W., Wan, J., 2007. Facile synthesis of superparamagnetic magnetite nanoparticles in liquid polyols. Journal of Colloid and Interface Science, 305(2): 366-370.
Cano, L. et al., 2010. Synthesis and characterization of superparamagnetic iron oxide nanoparticles for biomedical applications. Hyperfine Interactions, 195(1-3): 275-280.
Caravan, P., Ellison, J.J., McMurry, T.J., Lauffer, R.B., 1999. Gadolinium (III) chelates as MRI contrast agents: structure, dynamics, and applications. Chemical reviews, 99(9): 2293-2352.
Carillo, M.A., 2014. Chains of nanomagnets: How biological macromolecules stabilize their assembly. . PhD Thesis, Universität Potsdam, Potsdam. .
Carillo, M.A., Bennet, M., Faivre, D., 2013. Interaction of proteins associated with the magnetosome assembly in magnetotactic bacteria as revealed by two-hybrid two-photon excitation fluorescence lifetime imaging microscopy Forster resonance energy transfer. The Journal of Physical Chemistry B, 117(47): 14642-14648.
Carpenter, C., Ward, R., 2010. Iron Determination in Meat Using Ferrozine Assay, Food Analysis Laboratory Manual. Springer, pp. 69-73.

Chen, C. et al., 2006. Nanoparticle-templated assembly of viral protein cages. Nano letters, 6(4): 611-615.
Chiu-Lam, A., Rinaldi, C., 2016. Nanoscale Thermal Phenomena in the Vicinity of Magnetic Nanoparticles in Alternating Magnetic Fields. Advanced Functional Materials.
Cicha, I., 2016. Strategies to enhance nanoparticle-endothelial interactions under flow. Journal of Cellular Biotechnology, 1(2): 191-208.
Cicha, I. et al., 2009. Shear stress preconditioning modulates endothelial susceptibility to circulating TNF-α and monocytic cell recruitment in a simplified model of arterial bifurcations. Atherosclerosis, 207(1): 93-102.
Clement, O., Siauve, N., Cuénod, C.-A., Frija, G., 1998. Liver Imaging With Ferumoxides (Feridex (R)): Fundamentals, Controversies, and Practical Aspects. Topics in Magnetic Resonance Imaging, 9(3): 167-182.
Cöelfen, H., Antonietti, M., 2008. Mesocrystals and nonclassical crystallization. John Wiley & Sons.
Cölfen, H., Antonietti, M., 2005. Mesocrystals: inorganic superstructures made by highly parallel crystallization and controlled alignment. Angewandte Chemie International Edition, 44(35): 5576-5591.
Cölfen, H., Antonietti, M., 2008. Nonclassical Crystallization. Mesocrystals and Nonclassical Crystallization: 73-101.
Cölfen, H., Mann, S., 2003. Higher-order organization by mesoscale self-assembly and transformation of hybrid nanostructures. Angewandte Chemie International Edition, 42(21): 2350-2365.
Cornell, R.M., Schwertmann, U., 2003. The iron oxides: structure, properties, reactions, occurrences and uses. John Wiley & Sons.
Daou, T.J. et al., 2006. Hydrothermal Synthesis of Monodisperse Magnetite Nanoparticles. Chemistry of Materials, 18(18): 4399-4404.
Das, R., Doniach, S., 2008. Structural studies of proteins and nucleic acids in solution using small angle X-ray scattering (SAXS), Soft Matter Characterization. Springer, pp. 1083-1108.
Dmitri, I.S., Michel, H.J.K., 2003. Small-angle scattering studies of biological macromolecules in solution. Reports on Progress in Physics, 66(10): 1735.
Dunin-Borkowski, R., McCartney, M., Smith, D., 2004. Encyclopedia of Nanoscience and Nanotechnology. 3American Scientific Publishers, Stevenson Ranch: 41-100.
Dunlop, D.J., Özdemir, Ö., 2001. Rock magnetism: fundamentals and frontiers, 3. Cambridge university press.
Dutz, S., Hergt, R., 2014. Magnetic particle hyperthermia—a promising tumour therapy? Nanotechnology, 25(45): 452001.

Egami, T., Billinge, S.J., 2003. Underneath the Bragg peaks: structural analysis of complex materials, 16. Elsevier.
Fabian, K. et al., 1996. Three-dimensional micromagnetic calculations for magnetite using FFT. Geophys. J. Int., 124(1): 89-104.
Faivre, D., 2016. Iron Oxides: From Nature to Applications. John Wiley & Sons.
Faivre, D., Bennet, M., 2016. Materials science: Magnetic nanoparticles line up. Nature, 535(7611): 235-236.
Faivre, D., Godec, T.U., 2015. From bacteria to mollusks: the principles underlying the biomineralization of iron oxide materials. Angewandte Chemie International Edition, 54(16): 4728-4747.
Faivre, D., Schuler, D., 2008. Magnetotactic bacteria and magnetosomes. Chemical Reviews, 108(11): 4875-4898.
Falbe, A.J., Regitz, M., Römpp Lexikon Chemie.
Frandsen, C. et al., 2005. Oriented attachment and exchange coupling of α− Fe 2 O 3 nanoparticles. Physical Review B, 72(21): 214406.
Fratzl, P., Weiner, S., 2010. Bio-Inspired Materials–Mining the Old Literature for New Ideas. Advanced Materials, 22(41): 4547-4550.
Gazeau, F., Lévy, M., Wilhelm, C., 2008. Optimizing magnetic nanoparticle design for nanothermotherapy.
Ge, J., Hu, Y., Biasini, M., Beyermann, W.P., Yin, Y., 2007. Superparamagnetic magnetite colloidal nanocrystal clusters. Angewandte Chemie International Edition, 46(23): 4342-4345.
Geiss, C.E., Egli, R., Zanner, C.W., 2008. Direct estimates of pedogenic magnetite as a tool to reconstruct past climates from buried soils. Journal of Geophysical Research: Solid Earth, 113(B11).
Grabarek, Z., Gergely, J., 1990. Zero-length crosslinking procedure with the use of active esters. Analytical biochemistry, 185(1): 131-135.
Hajdú, A., Illés, E., Tombácz, E., Borbáth, I., 2009. Surface charging, polyanionic coating and colloid stability of magnetite nanoparticles. Colloids and Surfaces A: Physicochemical and Engineering Aspects, 347(1): 104-108.
Hargrove, R.S., Kündig, W., 1970. Mössbauer measurements of magnetite below the Verwey transition. Solid State Communications, 8(5): 303-308.
Hergt, R., Dutz, S., Müller, R., Zeisberger, M., 2006. Magnetic particle hyperthermia: nanoparticle magnetism and materials development for cancer therapy. Journal of Physics: Condensed Matter, 18(38): S2919.
Hermanson, G.T., 2013a. Bioconjugate techniques. Academic press.
Hermanson, G.T., 2013b. Chapter 20 - Antibody Modification and Conjugation, Bioconjugate Techniques (Third edition). Academic Press, Boston, pp. 867-920.

Hoell, A., Wiedenmann, A., Heyen, U., Schüler, D., 2004. Nanostructure and field-induced arrangement of magnetosomes studied by SANSPOL. Physica B: Condensed Matter, 350(1–3, Supplement): E309-E313.
Hollamby, M.J., 2013. Practical applications of small-angle neutron scattering. Physical Chemistry Chemical Physics, 15(26): 10566-10579.
Hou, X., Amais, R.S., Jones, B.T., Donati, G.L., 2000. Inductively coupled plasma optical emission spectrometry. Encyclopedia of analytical chemistry.
Houben, L., Sadan, M.B., 2011. Refinement procedure for the image alignment in high-resolution electron tomography. Ultramicroscopy, 111(9): 1512-1520.
Hu, M.-J. et al., 2008. High yield synthesis of bracelet-like hydrophilic Ni− Co magnetic alloy flux-closure nanorings. Journal of the American Chemical Society, 130(35): 11606-11607.
Huggins, K.N., Schoen, A.P., Arunagirinathan, M.A., Heilshorn, S.C., 2014. Multi-Site Functionalization of Protein Scaffolds for Bimetallic Nanoparticle Templating. Advanced Functional Materials, 24(48): 7737-7744.
Hugounenq, P. et al., 2012. Iron oxide monocrystalline nanoflowers for highly efficient magnetic hyperthermia. The Journal of Physical Chemistry C, 116(29): 15702-15712.
Ikoma, T. et al., 2007. Drug-supported microparticles of calcium carbonate nanocrystals and its covering with hydroxyapatite. Journal of nanoscience and nanotechnology, 7(3): 822-827.
Ito, A., Shinkai, M., Honda, H., Kobayashi, T., 2005. Medical application of functionalized magnetic nanoparticles. Journal of bioscience and bioengineering, 100(1): 1-11.
Ito, A. et al., 2004. Tissue engineering using magnetite nanoparticles and magnetic force: heterotypic layers of cocultured hepatocytes and endothelial cells. Tissue engineering, 10(5-6): 833-840.
Jackson, A.J., 2008. Introduction to Small-Angle Neutron Scattering and Neutron Reflectometry. NIST Center for Neutron Research, Gaithersburg: 12.
Jehle, F. et al., 2016. Genetically Engineered Organization: Protein Template, Biological Recognition Sites, and Nanoparticles. Advanced Materials Interfaces: n/a-n/a.
Jogler, C., Schüler, D., 2009. Genomics, genetics, and cell biology of magnetosome formation. Annual review of microbiology, 63: 501-521.
Jolivet, J.-P., Chaneac, C., Tronc, E., 2004. Iron oxide chemistry. From molecular clusters to extended solid networks. Chemical Communications(5): 481-483.
Katzmann, E., Scheffel, A., Gruska, M., Plitzko, J.M., Schüler, D., 2010. Loss of the actin-like protein MamK has pleiotropic effects on magnetosome

formation and chain assembly in Magnetospirillum gryphiswaldense. Molecular Microbiology, 77(1): 208-224.
Ke, N., Wang, X., Xu, X., Abassi, Y.A., 2011. The xCELLigence system for real-time and label-free monitoring of cell viability. Mammalian Cell Viability: Methods and Protocols: 33-43.
Kiani, B., Faivre, D., Klumpp, S., 2015. Elastic properties of magnetosome chains. New Journal of Physics, 17(4): 043007.
Kievit, F.M. et al., 2009. PEI–PEG–chitosan-copolymer-coated iron oxide nanoparticles for safe gene delivery: synthesis, complexation, and transfection. Advanced functional materials, 19(14): 2244-2251.
Kolhatkar, A.G., Jamison, A.C., Litvinov, D., Willson, R.C., Lee, T.R., 2013. Tuning the magnetic properties of nanoparticles. International journal of molecular sciences, 14(8): 15977-16009.
Komeili, A., Li, Z., Newman, D.K., Jensen, G.J., 2006. Magnetosomes are cell membrane invaginations organized by the actin-like protein MamK. Science, 311(5758): 242-245.
Kooi, M. et al., 2003. Accumulation of ultrasmall superparamagnetic particles of iron oxide in human atherosclerotic plaques can be detected by in vivo magnetic resonance imaging. Circulation, 107(19): 2453-2458.
Kovalenko, M.V. et al., 2007. Fatty acid salts as stabilizers in size-and shape-controlled nanocrystal synthesis: the case of inverse spinel iron oxide. Journal of the American Chemical Society, 129(20): 6352-6353.
Krueger, S. et al., 1990. Small-angle neutron scattering from bacterial magnetite. Journal of Applied Physics, 67(9): 4475-4477.
Kruse, H.P., 1997. Römpp Lexikon Chemie. 10. Auflage, A-Cl. Herausgegeben von J. Falbe und M. Regitz. 780 Seiten. Georg Thieme Verlag, Stuttgart, New York 1996. Vorbestellpreis bis 31. 12. 1997: 248,-DM; danach 298,-DM. Food/Nahrung, 41(2): 122-122.
Kumari, M. et al., 2014. Distinguishing magnetic particle size of iron oxide nanoparticles with first-order reversal curves. Journal of Applied Physics, 116(12): 124304.
Kumfer, B.M., Shinoda, K., Jeyadevan, B., Kennedy, I.M., 2010. GAS-PHASE FLAME SYNTHESIS AND PROPERTIES OF MAGNETIC IRON OXIDE NANOPARTICLES WITH REDUCED OXIDATION STATE. Journal of aerosol science, 41(3): 257-265.
Kurppa, K. et al., 2007. Controlled Hybrid Nanostructures through Protein-Mediated Noncovalent Functionalization of Carbon Nanotubes. Angewandte Chemie International Edition, 46(34): 6446-6449.
Lai, Y., Yin, W., Liu, J., Xi, R., Zhan, J., 2009. One-pot green synthesis and bioapplication of l-arginine-capped superparamagnetic Fe 3 O 4 nanoparticles. Nanoscale research letters, 5(2): 302.

Laurent, S., Dutz, S., Häfeli, U.O., Mahmoudi, M., 2011. Magnetic fluid hyperthermia: focus on superparamagnetic iron oxide nanoparticles. Advances in colloid and interface science, 166(1): 8-23.

Laurent, S. et al., 2008. Magnetic iron oxide nanoparticles: synthesis, stabilization, vectorization, physicochemical characterizations, and biological applications. Chemical reviews, 108(6): 2064-2110.

Laurent, S., Mahmoudi, M., 2011. Superparamagnetic iron oxide nanoparticles: promises for diagnosis and treatment of cancer. Int J Mol Epidemiol Genet, 2(4): 367-390.

Lee, N. et al., 2012. Water-dispersible ferrimagnetic iron oxide nanocubes with extremely high r 2 relaxivity for highly sensitive in vivo MRI of tumors. Nano letters, 12(6): 3127-3131.

Lee, N. et al., 2015. Iron oxide based nanoparticles for multimodal imaging and magnetoresponsive therapy. Chemical reviews, 115(19): 10637-10689.

Lefèvre, C.T. et al., 2013. Comparative genomic analysis of magnetotactic bacteria from the Deltaproteobacteria provides new insights into magnetite and greigite magnetosome genes required for magnetotaxis. Environmental Microbiology, 15(10): 2712-2735.

Lenders, J.J. et al., 2015. Bioinspired magnetite crystallization directed by random copolypeptides. Advanced Functional Materials, 25(5): 711-719.

Lidmar, J., Mirny, L., Nelson, D.R., 2003. Virus shapes and buckling transitions in spherical shells. Physical Review E, 68(5): 051910.

Lin, H.-K., van der Schoot, P., Zandi, R., 2012. Impact of charge variation on the encapsulation of nanoparticles by virus coat proteins. Physical biology, 9(6): 066004.

Lin, W., Benzerara, K., Faivre, D., Pan, Y., 2014. Intracellular biomineralization in bacteria. Frontiers in Microbiology, 5: 293.

Lower, B.H., Bazylinski, D.A., 2013. The Bacterial Magnetosome: A Unique Prokaryotic Organelle. Journal of Molecular Microbiology and Biotechnology, 23(1-2): 63-80.

Lucon, J. et al., 2012. Use of the interior cavity of the P22 capsid for site-specific initiation of atom-transfer radical polymerization with high-density cargo loading. Nature chemistry, 4(10): 781-788.

Ma, M. et al., 2003. Preparation and characterization of magnetite nanoparticles coated by amino silane. Colloids and Surfaces A: Physicochemical and Engineering Aspects, 212(2–3): 219-226.

Maity, D., Agrawal, D., 2007. Synthesis of iron oxide nanoparticles under oxidizing environment and their stabilization in aqueous and non-aqueous media. Journal of Magnetism and Magnetic Materials, 308(1): 46-55.

Massart, R., 1981. Preparation of aqueous magnetic liquids in alkaline and acidic media. IEEE transactions on magnetics, 17(2): 1247-1248.
Matus, M. et al., 2016. Energy losses in mechanically modified bacterial magnetosomes. Journal of Physics D: Applied Physics, 49(36): 365002.
Matuszak, J. et al., 2016. Nanoparticles for intravascular applications: physicochemical characterization and cytotoxicity testing. Nanomedicine, 11(6): 597-616.
McBain, S.C., Yiu, H.H.P., Dobson, J., 2008. Magnetic nanoparticles for gene and drug delivery. International Journal of Nanomedicine, 3(2): 169-180.
Meldrum, F.C., Heywood, B.R., Mann, S., 1992. Magnetoferritin: in vitro synthesis of a novel magnetic protein. Science, 257(5069): 522-523.
Merbach, A.E., Tóth, É., 2001. The chemistry of contrast agents in medical magnetic resonance imaging, 46. Wiley Online Library.
Midgley, P.A., Dunin-Borkowski, R.E., 2009. Electron tomography and holography in materials science. Nature materials, 8(4): 271-280.
Mihai, M. et al., 2013. Calcium carbonate–magnetite–chondroitin sulfate composite microparticles with enhanced pH stability and superparamagnetic properties. Crystal Growth & Design, 13(8): 3535-3545.
Mikhaylova, M. et al., 2004. BSA immobilization on amine-functionalized superparamagnetic iron oxide nanoparticles. Chemistry of Materials, 16(12): 2344-2354.
Milonjić, S.K., Kopečni, M.M., Ilić, Z.E., 1983. The point of zero charge and adsorption properties of natural magnetite. Journal of Radioanalytical Chemistry, 78(1): 15-24.
Murat, D. et al., 2012. The magnetosome membrane protein, MmsF, is a major regulator of magnetite biomineralization in Magnetospirillum magneticum AMB-1. Molecular microbiology, 85(4): 684-699.
Muxworthy, A.R., Williams, W., 2009. Critical superparamagnetic/single-domain grain sizes in interacting magnetite particles: implications for magnetosome crystals. J. R. Soc. Interface, 6(41): 1207-1212.
Na, H.B., Song, I.C., Hyeon, T., 2009. Inorganic nanoparticles for MRI contrast agents. Advanced materials, 21(21): 2133-2148.
Nassar, N., Husein, M., 2006. Preparation of iron oxide nanoparticles from FeCl3 solid powder using microemulsions. physica status solidi (a), 203(6): 1324-1328.
Niederberger, M., Cölfen, H., 2006. Oriented attachment and mesocrystals: non-classical crystallization mechanisms based on nanoparticle assembly. Physical Chemistry Chemical Physics, 8(28): 3271-3287.

Nordling, S., Nilsson, B., Magnusson, P.U., 2014. A Novel In vitro Model for Studying the Interactions Between Human Whole Blood and Endothelium. Journal of visualized experiments: JoVE(93).

O'Neil, A., Reichhardt, C., Johnson, B., Prevelige, P.E., Douglas, T., 2011. Genetically programmed in vivo packaging of protein cargo and its controlled release from bacteriophage P22. Angewandte Chemie International Edition, 50(32): 7425-7428.

Oatley, C., Nixon, W., Pease, R., 1966. Scanning electron microscopy. Advances in Electronics and Electron Physics, 21: 181-247.

Olszewska, A., 2015. Forming magnetic chain with the help of biological organisms

Die Bildung magnetischer Kettenstrukturen mit Hilfe biologischer Organismen.

Onat, D., Brillon, D., Colombo, P.C., Schmidt, A.M., 2011. Human vascular endothelial cells: a model system for studying vascular inflammation in diabetes and atherosclerosis. Current diabetes reports, 11(3): 193-202.

Paris, O., Burgert, I., Fratzl, P., 2010. Biomimetics and biotemplating of natural materials. Mrs Bulletin, 35(03): 219-225.

Park, J.Y., Choi, E.S., Baek, M.J., Lee, G.H., 2009. Colloidal stability of amino acid coated magnetite nanoparticles in physiological fluid. Materials Letters, 63(3): 379-381.

Patterson, D.P., Rynda-Apple, A., Harmsen, A.L., Harmsen, A.G., Douglas, T., 2013. Biomimetic antigenic nanoparticles elicit controlled protective immune response to influenza. ACS nano, 7(4): 3036-3044.

Philipse, A.P., Maas, D., 2002. Magnetic colloids from magnetotactic bacteria: chain formation and colloidal stability. Langmuir, 18(25): 9977-9984.

Pipich, V., 2013. http://iffwww.iff.kfa-juelich.de/~pipich/dokuwiki/doku.php/qtikws.

Pradel, N., Santini, C.-L., Bernadac, A., Fukumori, Y., Wu, L.-F., 2006. Biogenesis of actin-like bacterial cytoskeletal filaments destined for positioning prokaryotic magnetic organelles. Proceedings of the National Academy of Sciences, 103(46): 17485-17489.

Pyrz, W.D., Buttrey, D.J., 2008. Particle size determination using TEM: a discussion of image acquisition and analysis for the novice microscopist. Langmuir, 24(20): 11350-11360.

Qazi, S. et al., 2012. P22 viral capsids as nanocomposite high-relaxivity MRI contrast agents. Molecular pharmaceutics, 10(1): 11-17.

Rawlings, A.E. et al., 2014. Self-assembled MmsF proteinosomes control magnetite nanoparticle formation in vitro. Proceedings of the National Academy of Sciences, 111(45): 16094-16099.

Reichhardt, C. et al., 2011. Templated assembly of organic–inorganic materials using the core shell structure of the P22 bacteriophage. Chemical Communications, 47(22): 6326-6328.

Reimer, P., Balzer, T., 2003. Ferucarbotran (Resovist): a new clinically approved RES-specific contrast agent for contrast-enhanced MRI of the liver: properties, clinical development, and applications. European radiology, 13(6): 1266-1276.

Roca, A.G. et al., 2009. Progress in the preparation of magnetic nanoparticles for applications in biomedicine. Journal of Physics D: Applied Physics, 42(22): 224002.

Roe, R.-J., 2000. Methods of X-ray and neutron scattering in polymer science, 739. Oxford University Press on Demand.

Rudolf, H., Silvio, D., Robert, M., Matthias, Z., 2006. Magnetic particle hyperthermia: nanoparticle magnetism and materials development for cancer therapy. Journal of Physics: Condensed Matter, 18(38): S2919.

Salazar-Alvarez, G., Muhammed, M., Zagorodni, A.A., 2006. Novel flow injection synthesis of iron oxide nanoparticles with narrow size distribution. Chemical Engineering Science, 61(14): 4625-4633.

Scheffel, A., Gärdes, A., Grünberg, K., Wanner, G., Schüler, D., 2008. The major magnetosome proteins MamGFDC are not essential for magnetite biomineralization in *Magnetospirillum gryphiswaldense*, but regulate the size of magnetosome crystals. J. Bacteriol., 190(1): 377-386.

Schmitz, M., 2010. High-Resolution Synchrotron X-ray Scattering reveals the Difference in the Ultrastructure of biogenic and Abiotic Magnetite Nanoparticles.

Schübbe, S. et al., 2003. Characterization of a spontaneous nonmagnetic mutant of Magnetospirillum gryphiswaldense reveals a large deletion comprising a putative magnetosome island. J. Bacteriol., 185(19): 5779-5790.

Schwertmann, U., Cornell, R.M., 2007. The Iron Oxides, Iron Oxides in the Laboratory. Wiley-VCH Verlag GmbH, pp. 5-18.

Serantes, D. et al., 2014. Multiplying magnetic hyperthermia response by nanoparticle assembling. The Journal of Physical Chemistry C, 118(11): 5927-5934.

Servid, A., Jordan, P., O'Neil, A., Prevelige, P., Douglas, T., 2013. Location of the bacteriophage P22 coat protein C-terminus provides opportunities for the design of capsid-based materials. Biomacromolecules, 14(9): 2989-2995.

Seto, J. et al., 2012. Structure-property relationships of a biological mesocrystal in the adult sea urchin spine. Proceedings of the National Academy of Sciences, 109(10): 3699-3704.

Shimizu, K. et al., 2007. Bone tissue engineering with human mesenchymal stem cell sheets constructed using magnetite nanoparticles and magnetic force. Journal of Biomedical Materials Research Part B: Applied Biomaterials, 82(2): 471-480.

Shubitidze, F., Kekalo, K., Stigliano, R., Baker, I., 2015. Magnetic nanoparticles with high specific absorption rate of electromagnetic energy at low field strength for hyperthermia therapy. Journal of applied physics, 117(9): 094302.

Siglreitmeier, M. et al., 2015. Multifunctional layered magnetic composites. Beilstein journal of nanotechnology, 6(1): 134-148.

Sigma-Aldrich, Poly-l-arginine.

Siponen, M.I. et al., 2013a. Structural insight into magnetochrome-mediated magnetite biomineralization. Nature, 502(7473): 681-684.

Siponen, M.I. et al., 2013b. Structural insight into magnetochrome-mediated magnetite biomineralization. Nature, 502(7473): 681-684.

Skeel, R.T., Khleif, S.N., 2011. Handbook of cancer chemotherapy. Lippincott Williams & Wilkins.

Sone, E.D., Stupp, S.I., 2004. Semiconductor-encapsulated peptide-amphiphile nanofibers. Journal of the American Chemical Society, 126(40): 12756-12757.

Sturm, E.V., Cölfen, H., 2016. Mesocrystals: structural and morphogenetic aspects. Chemical Society Reviews.

Susil, R.C. et al., 2003. System for MR Image–guided Prostate Interventions: Canine Study 1. Radiology, 228(3): 886-894.

Svergun, D.I., Koch, M.H., 2003. Small-angle scattering studies of biological macromolecules in solution. Reports on Progress in Physics, 66(10): 1735.

Sviben, S. et al., 2016. A vacuole-like compartment concentrates a disordered calcium phase in a key coccolithophorid alga. Nature communications, 7.

Tan, S.T., Wendorff, J.H., Pietzonka, C., Jia, Z.H., Wang, G.Q., 2005. Biocompatible and biodegradable polymer nanofibers displaying superparamagnetic properties. ChemPhysChem, 6(8): 1461-1465.

Taukulis, R. et al., 2015. Magnetic iron oxide nanoparticles as MRI contrast agents-a comprehensive physical and theoretical study. Magnetohydrodynamics, 51(4): 721-747.

Thiesen, B., Jordan, A., 2008. Clinical applications of magnetic nanoparticles for hyperthermia. International journal of hyperthermia, 24(6): 467-474.

Thomas-Keprta, K., Bazlinski, D., Kirschvink, J., 2000. SJ Clemett, DS McKay, SJ Wentworth, H. Vali, EK Gibson. Jr. CS Romanek. Geochim. Cosmochim. Acta, 64: 4049.

Tombacz, E., Majzik, A., Horvat, Z., Illes, E., 2006. Magnetite in aqueous medium: coating its surface and surface coated with it. Romanian Reports in physics, 58(3): 281.

Uchida, M. et al., 2011. Site-directed coordination chemistry with P22 virus-like particles. Langmuir, 28(4): 1998-2006.

Uebe, R., Schüler, D., 2016. Magnetosome biogenesis in magnetotactic bacteria. Nature Reviews Microbiology, 14(10): 621-637.

Ullrich, S., Kube, M., Schübbe, S., Reinhardt, R., Schüler, D., 2005. A Hypervariable 130-Kilobase Genomic Region of *Magnetospirillum gryphiswaldense* Comprises a Magnetosome Island Which Undergoes Frequent Rearrangements during Stationary Growth. J. Bacteriol., 187(21): 7176-7184.

Vayssieres, L., Chanéac, C., Tronc, E., Jolivet, J.P., 1998. Size tailoring of magnetite particles formed by aqueous precipitation: An example of thermodynamic stability of nanometric oxide particles. Journal of colloid and interface science, 205(2): 205-212.

Vikesland, P., Rebodos, R., Bottero, J., Rose, J., Masion, A., 2016. Aggregation and sedimentation of magnetite nanoparticle clusters. Environmental Science: Nano, 3(3): 567-577.

Vinogradov, A.V., Vinogradov, V.V., 2014. Low-temperature sol–gel synthesis of crystalline materials. RSC Advances, 4(86): 45903-45919.

Vyazovkin, S., 2002. Thermogravimetric Analysis, Characterization of Materials. John Wiley & Sons, Inc.

Wan, J., Tang, J., Zhang, C., Yuan, R., Chen, K., 2015. Insight into the formation of magnetite mesocrystals from ferrous precursors in ethylene glycol. Chemical Communications, 51(88): 15910-15913.

Wang, K. et al., 2011. BRCAA1 monoclonal antibody conjugated fluorescent magnetic nanoparticles for in vivo targeted magnetofluorescent imaging of gastric cancer. Journal of nanobiotechnology, 9(1): 1.

Wang, L., Bao, J., Wang, L., Zhang, F., Li, Y., 2006. One-Pot Synthesis and Bioapplication of Amine-Functionalized Magnetite Nanoparticles and Hollow Nanospheres. Chemistry–A European Journal, 12(24): 6341-6347.

Wei, W., Zhaohui, W., Taekyung, Y., Changzhong, J., Woo-Sik, K., 2015. Recent progress on magnetic iron oxide nanoparticles: synthesis, surface functional strategies and biomedical applications. Science and Technology of Advanced Materials, 16(2): 023501.

Weissleder, R., Kelly, K., Sun, E.Y., Shtatland, T., Josephson, L., 2005. Cell-specific targeting of nanoparticles by multivalent attachment of small molecules. Nature biotechnology, 23(11): 1418-1423.

Wiberg, N., 2001. Holleman-Wiberg's inorganic chemistry. Academic Press, New York.

Widdrat, M. et al., 2014. Keeping Nanoparticles Fully Functional: Long-Term Storage and Alteration of Magnetite. ChemPlusChem, 79(8): 1225-1233.
Williams, D.B., Carter, C.B., 1996. The transmission electron microscope, Transmission electron microscopy. Springer, pp. 3-17.
Wörsdörfer, B., Pianowski, Z., Hilvert, D., 2012. Efficient in vitro encapsulation of protein cargo by an engineered protein container. Journal of the American Chemical Society, 134(2): 909-911.
Wu, W., He, Q., Jiang, C., 2008. Magnetic iron oxide nanoparticles: synthesis and surface functionalization strategies. Nanoscale Research Letters, 3(11): 397.
Wust, P. et al., 2002. Hyperthermia in combined treatment of cancer. The Lancet Oncology, 3(8): 487-497.
Wyckoff, R.W.G., Wyckoff, R.W., 1960. Crystal structures, 2. Interscience New York.
Xiao, W. et al., 2012. Prolonged in vivo circulation time by zwitterionic modification of magnetite nanoparticles for blood pool contrast agents. Contrast media & molecular imaging, 7(3): 320-327.
Xu, C. et al., 2008. Monodisperse Magnetite Nanoparticles Coupled with Nuclear Localization Signal Peptide for Cell-Nucleus Targeting. Chemistry–An Asian Journal, 3(3): 548-552.
Xuan, S. et al., 2007. A FeCO3 precursor-based route to microsized peanutlike Fe3O4. Crystal growth & design, 7(2): 430-434.
Yang, L., Killian, C.E., Kunz, M., Tamura, N., Gilbert, P., 2011. Biomineral nanoparticles are space-filling. Nanoscale, 3(2): 603-609.
Yao, R., Cao, C., Bai, J., 2013. Self-assembly of magnetite mesocrystal microdisks with hierarchical architectures. CrystEngComm, 15(17): 3279-3283.
Yuwono, V.M., Burrows, N.D., Soltis, J.A., Penn, R.L., 2010. Oriented aggregation: formation and transformation of mesocrystal intermediates revealed. Journal of the American Chemical Society, 132(7): 2163-2165.
Zhang, L., Dou, Y.-H., Gu, H.-C., 2006. Sterically induced shape control of magnetite nanoparticles. Journal of crystal growth, 296(2): 221-226.
Zhang, Y., Kohler, N., Zhang, M., 2002. Surface modification of superparamagnetic magnetite nanoparticles and their intracellular uptake. Biomaterials, 23(7): 1553-1561.
Zhang, Z., Satpathy, S., 1991. Electron states, magnetism, and the Verwey transition in magnetite. Physical Review B, 44(24): 13319.
Zhao, J. et al., 2016. Continuous Paranematic Ordering of Rigid and Semiflexible Amyloid-Fe3O4 Hybrid Fibrils in an External Magnetic Field. Biomacromolecules, 17(8): 2555-2561.

Zhongjun, W., Hui, Z., Xiaolei, W., Fan, Y., Xiurong, Y., 2009. One-pot green synthesis of biocompatible arginine-stabilized magnetic nanoparticles. Nanotechnology, 20(46): 465606.
Zhou, L., O'Brien, P., 2008. Mesocrystals: a new class of solid materials. Small, 4(10): 1566-1574.

APPENDIX

SYNTHESES OF MAGNETITE NANOPARTICLES IN THE PRESENCE OF ADDITIVES (ADDITION TO CHAPTER 3.1)

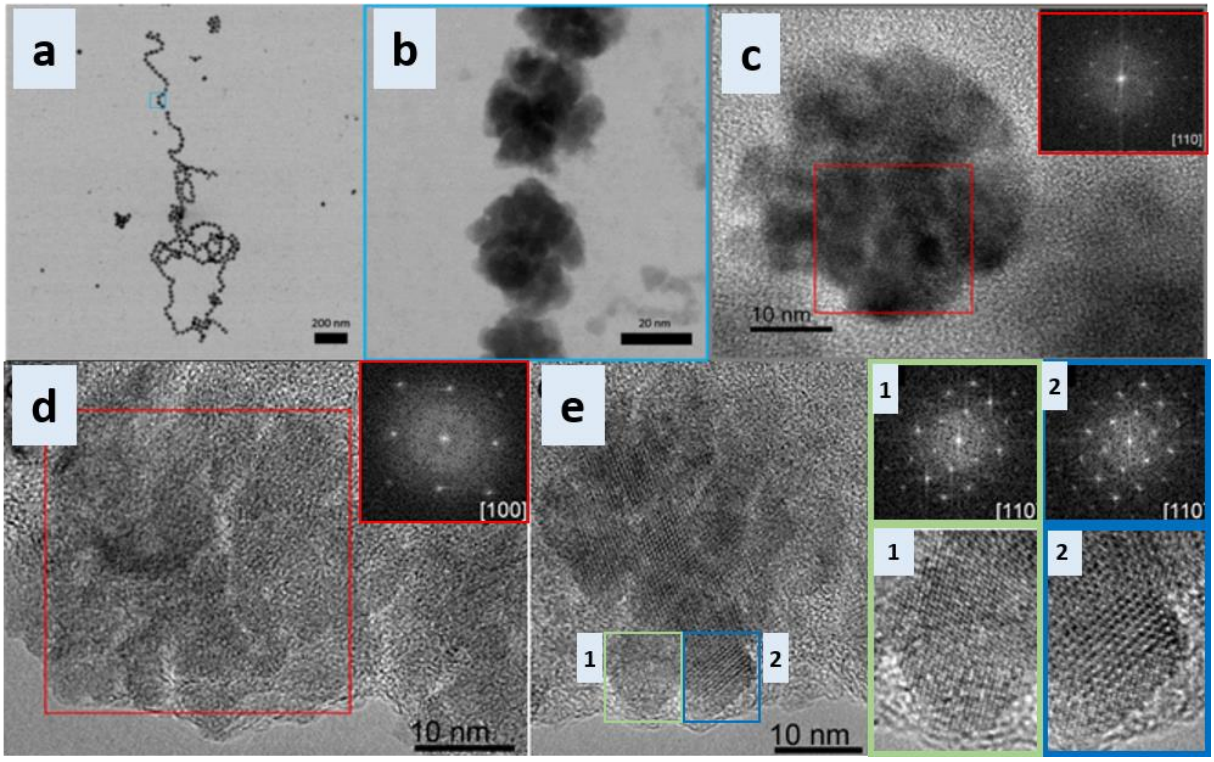

Figure 42: BF HRTEM images of polyR-magnetite nanoparticles: PolyR-magnetite nanoparticles forming (a) chain structures. Zoom within the chain: (b) Mesocrystal particles and higher magnification images of polyR-magnetite nanoparticles and (c-e) their corresponding FFT patterns showing single crystallinity.

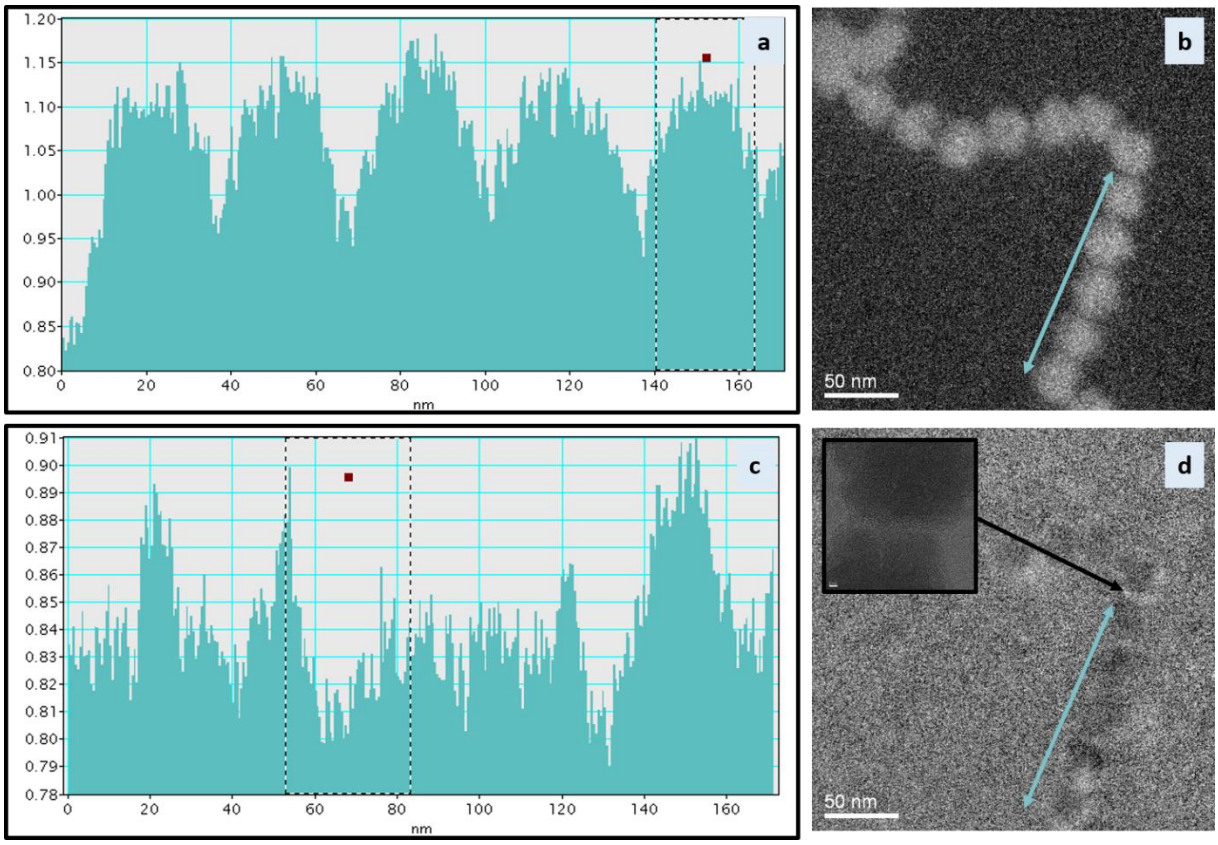

Figure 43: (a) Elemental distribution map of carbon of a polyR-magnetite nanoparticle chain of five particles derived from a (b) BF STEM image and marked with a blue arrow. (b) Elemental distribution map of carbon of a polyR-magnetite nanoparticle chain of five particles derived from a (d) BF STEM image and marked with a blue arrow. The inset in d shows a higher magnification BF STEM image of two particles with carbon in between.

Further EELS spectra were detected of 5 nanoparticles forming a chain according to the BF STEM images (Figure 43). In Figure 43a, an iron map is shown, which correspond to each of the five particles, alternating to that, Figure 43c shows the carbon map, which correspond to the carbon in between particles within the chain.

POLYR-MAGNETITE NANOPARTICLES AS MEDICAL TOOL (ADDITION TO CHAPTER 3.2)

ENDOTHELIAL EFFECTS OF POLYR-MAGNETITE NANOPARTICLES (ADDITION TO 3.2.4)

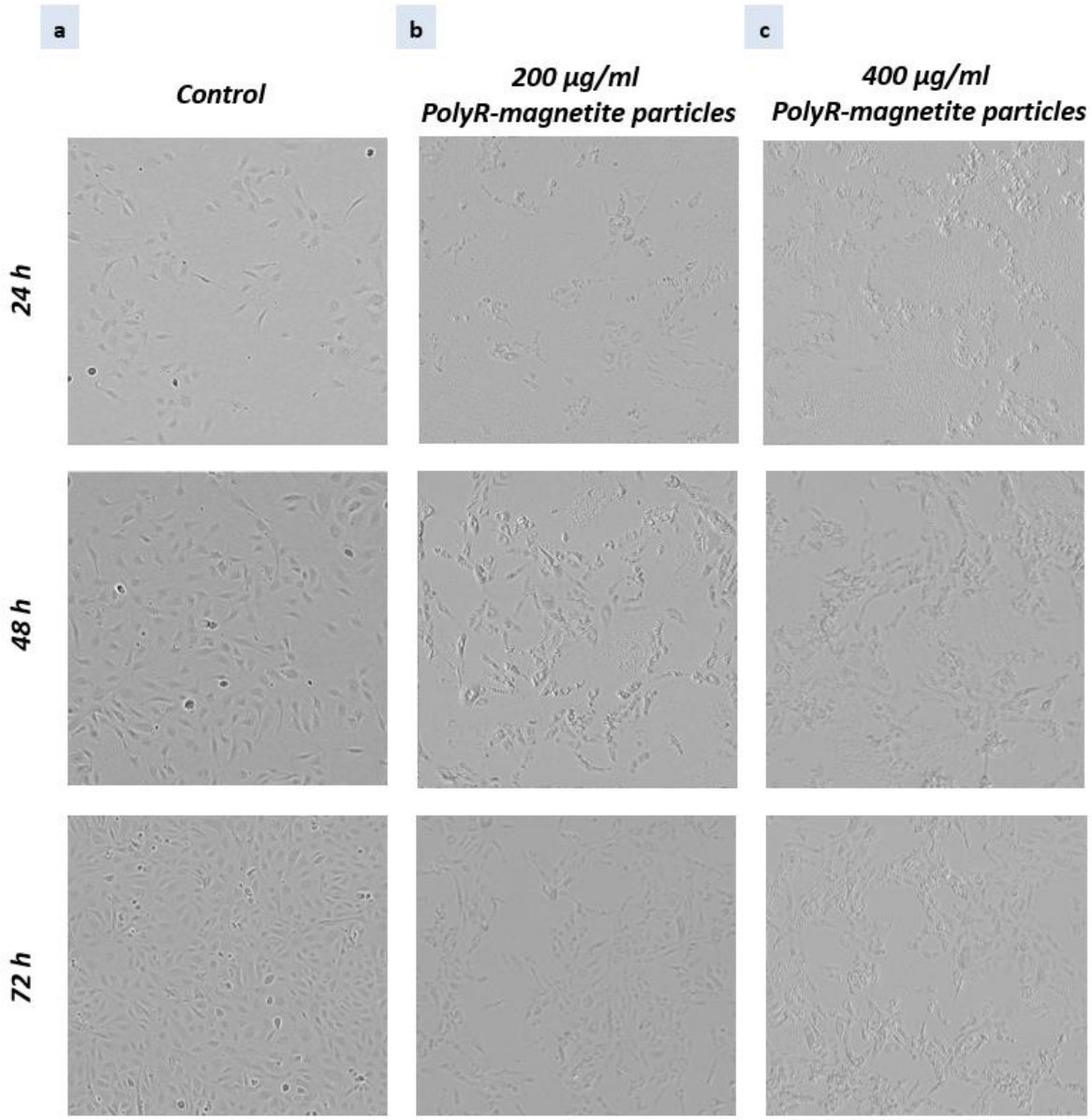

Figure 44: Live-cell microscopy of HUVECs treated with polyR-magnetite nanoparticles: Phase contrast images of HUVECs were taken after 24 h, 48 h and 72 h post particle addition. (a) HUVECs control, treated without any nanoparticles, (b) HUVECs treated with 200 µg/ml and (c) HUVECs treated with 400 µg/ml polyR-magnetite nanoparticles. Representative images of n=3 experiments are shown.

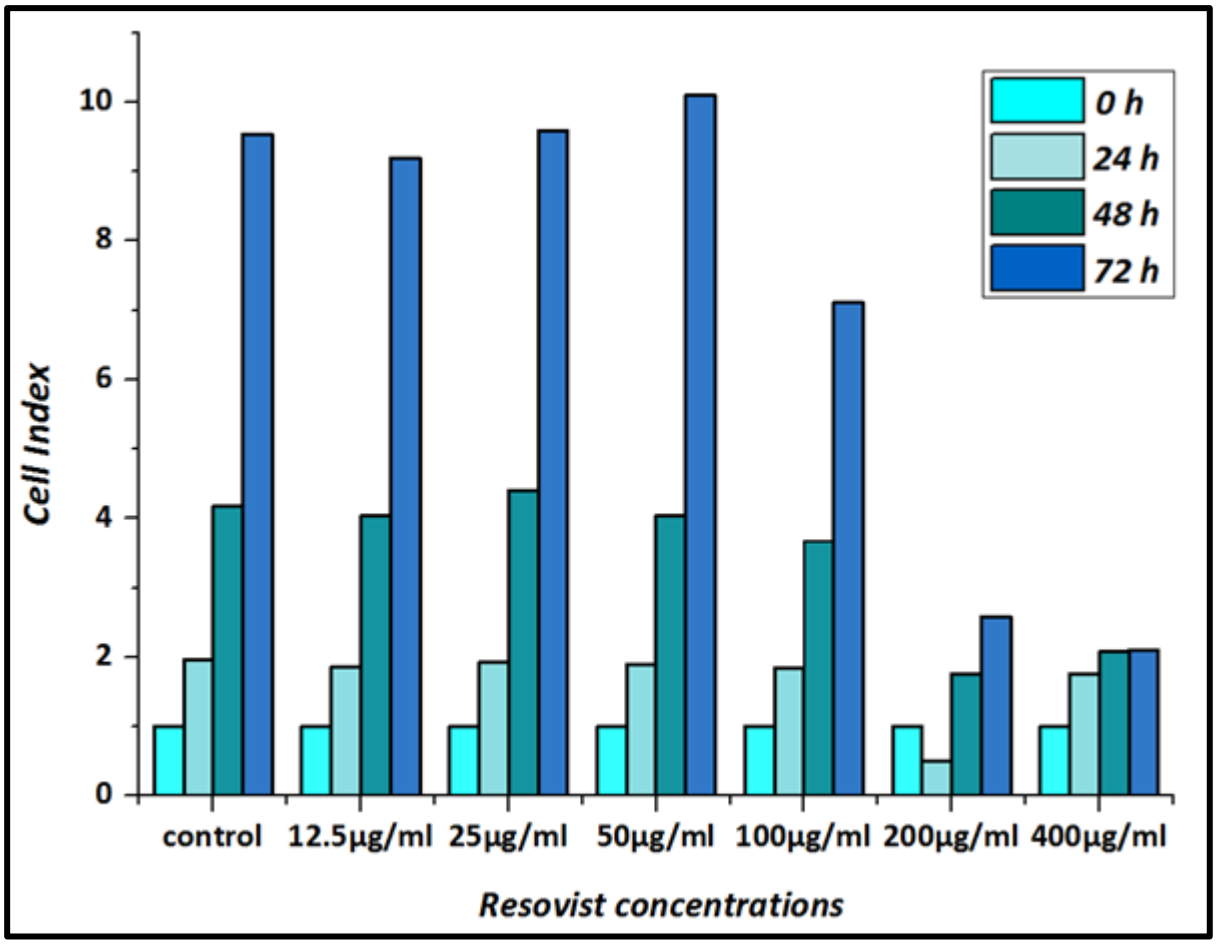

Figure 45: Biological effects of Resovist® on endothelial cells grown in static conditions by real-time cell analysis. HUVECs were seeded 24h before n Resovist® application. After these initial 24h, Resovist® in different concentrations was added and cell index was monitored up to 72h post application. Cell Index is displayed as x-fold of untreated controls. n=1. Data are expressed as mean of triplicate values.

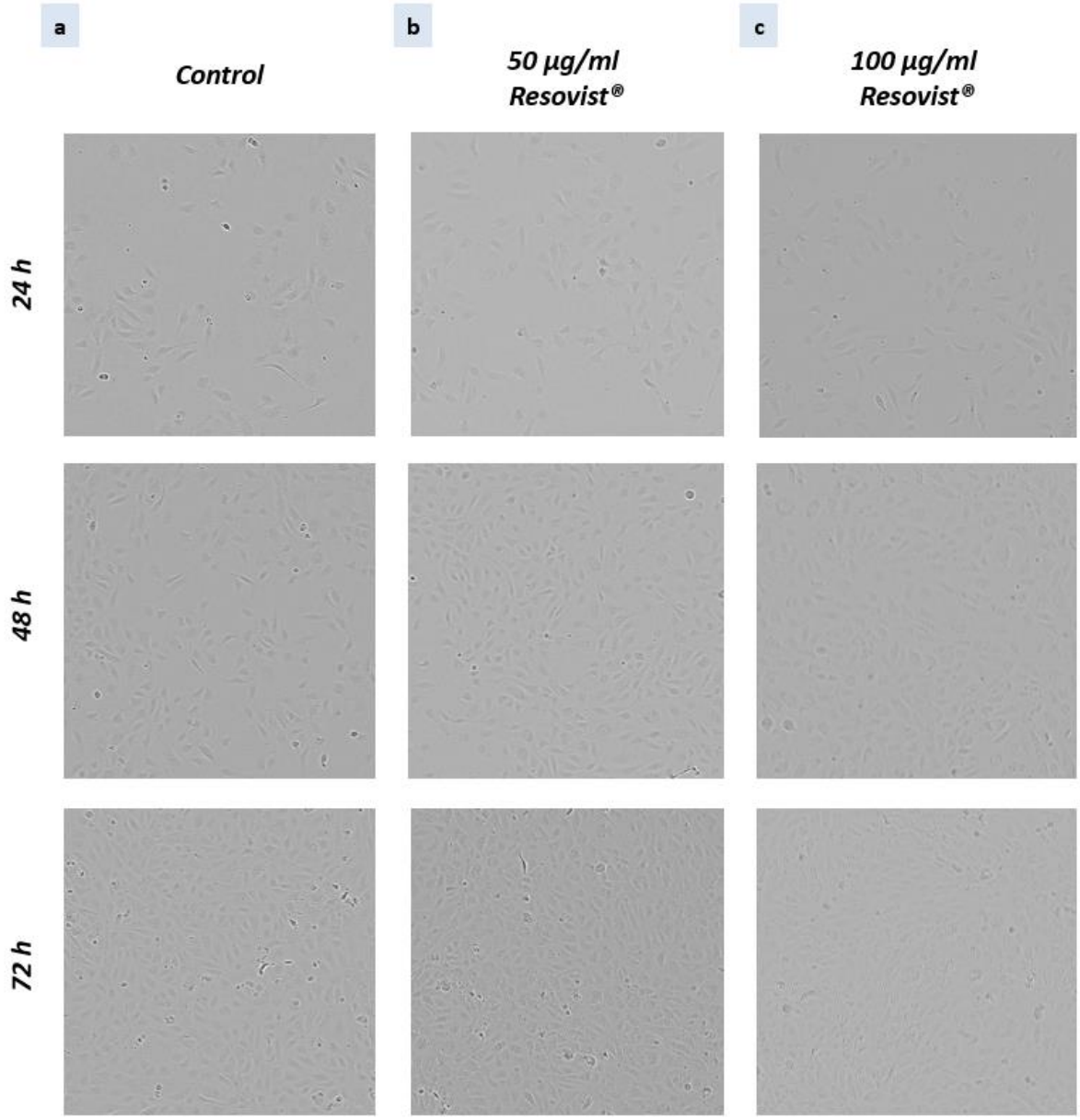

Figure 46: Live-cell microscopy of HUVECs treated with Resovist®: Phase contrast images of HUVECs were taken after 24 h, 48 h and 72 h post particle addition. (a) HUVECs control, treated without any nanoparticles, (b) HUVECs treated with 50 µg/ml and (c) HUVECs treated with 100 µg/ml Resovist®. Representative images of n=3 experiments are shown.

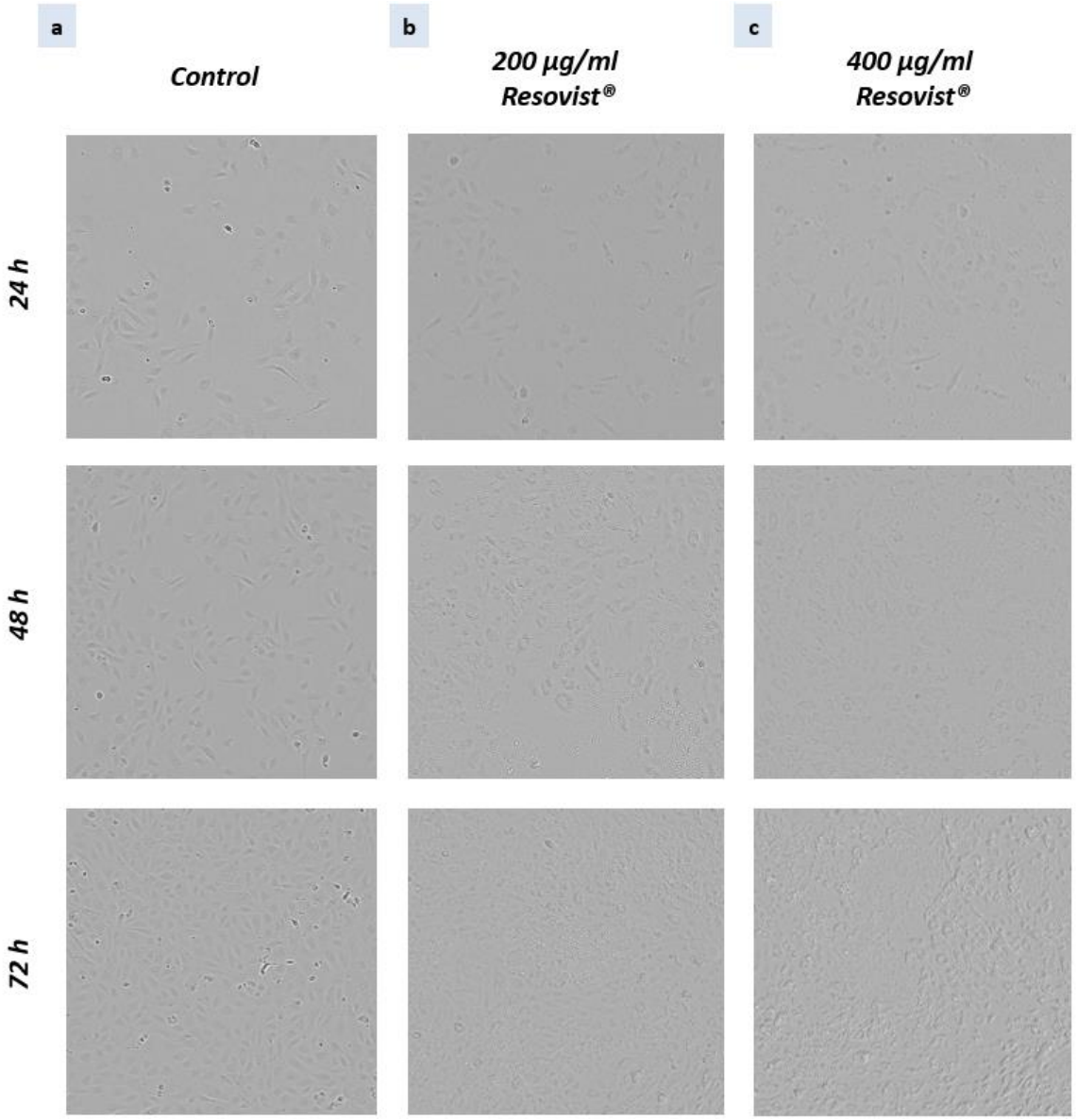

Figure 47: Live-cell microscopy of HUVECs treated with Resovist®: Phase contrast images of HUVECs were taken after 24 h, 48 h and 72 h post particle addition. (a) HUVECs control, treated without any nanoparticles, (b) HUVECs treated with 200 µg/ml and (c) HUVECs treated with 400 µg/ml Resovist®. Representative images of n=3 experiments are shown.

MAGNETITE PRECIPITATION IN THE PRESENCE OF CAPSIDS

Capsids- protein shells of viruses, are able to perform programmed packaging and sequestration of cargo molecules (Chen et al., 2006). Heterologous expressed protein-cages are excellent candidates for self-assembly nanocontainer systems from a limited number of protein subunits into symmetrical highly monodisperse structures, which can pack and release cargo molecules (Wörsdörfer et al., 2012), (Lin et al., 2012). Hence, viral capsids depict new approaches in synthetic encapsulation of molecules, e.g. enzymes, proteins and metal cores (Patterson et al., 2013). Here, the iron oxide magnetite should be precipitated within different capsid structures. Capsids enclose the viral genetic material and emerge in a broad variety of architecture (Lidmar et al., 2003). The icosahedral genetically engineered viral capsid P22 S39C has its origin in the P22 capsid of the Salmonella typhimurium bacteriophage P22 (Reichhardt et al., 2011), (Uchida et al., 2011), (Servid et al., 2013), (Lucon et al., 2012), (O'Neil et al., 2011). Different architectures of P22 S39C are available (Figure 48). ES is a 19 MDa capsid with consist of 420 subunits to 46 kDa each. The internal radius is 24 nm and its total volume is 58,000 nm3. The outer radius is 58 nm. In the case of EX consists of a more angular and larger icosahedron and the whole capsid gets bigger. Its inner radius is 29 nm, the outer radius is 62 nm and its total volume reaches 102,000 nm^3. In case of the WB the SP and the 12 pentamers on the P22 capsid leave.

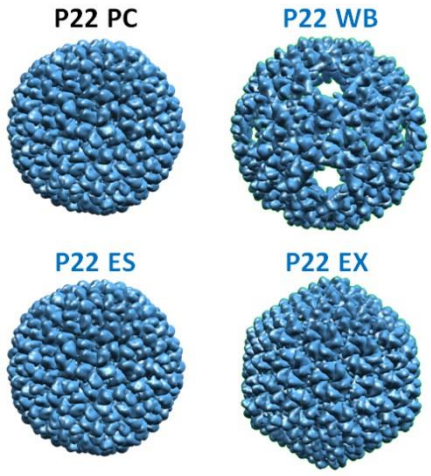

Figure 48: Different possible capsid structures based on the procapsid P22 PC.

EXPERIMENTAL

CAPSID BUFFER SEPARATION

In order to prepare capsids for further experiments, it was necessary to resuspend them in MilliQ H_2O to avoid salt residues which are disruptive in magnetite precipitation. Therefore, dialysis was performed, using 7000 MWCO Slide-A-Lyzer MINI Dialysis Units from Thermo Scientific. A sample volume of 100 µL was used. The Slide Lyzer MINI Dialysis Unit were closed and placed within a H_2O MilliQ (500 ml) filled covered baker glass under continuous stirring for 1.5 h to obtain equilibrium. The samples were collected from the corner of the Slide-A-Lyzer MINI Dialysis Unit to get the best sample recovery.

MAGNETITE PRECIPITATION IN THE PRESENCE OF CAPSIDS

Magnetite nanoparticles were precipitated in the presence of capsids using the co-precipitation method. Three types of capsids (see Figure 48) were used for further experiments. 0.1 M or 1 M degassed iron solutions and 0.1 M degassed sodium hydroxide solutions were prepared to ensure working under oxygen free conditions. 100 µl of the capsid solution was added to 1 ml of the iron solution. After 10 minutes of diffusion, sodium hydroxide was added under continuously stirring and oxygen free conditions and were adjusted to pH 9. After 10 minutes of continuous stirring, a magnetic separation was performed, whereas the remaining pellet was resuspended in 1 ml MilliQ H_2O.

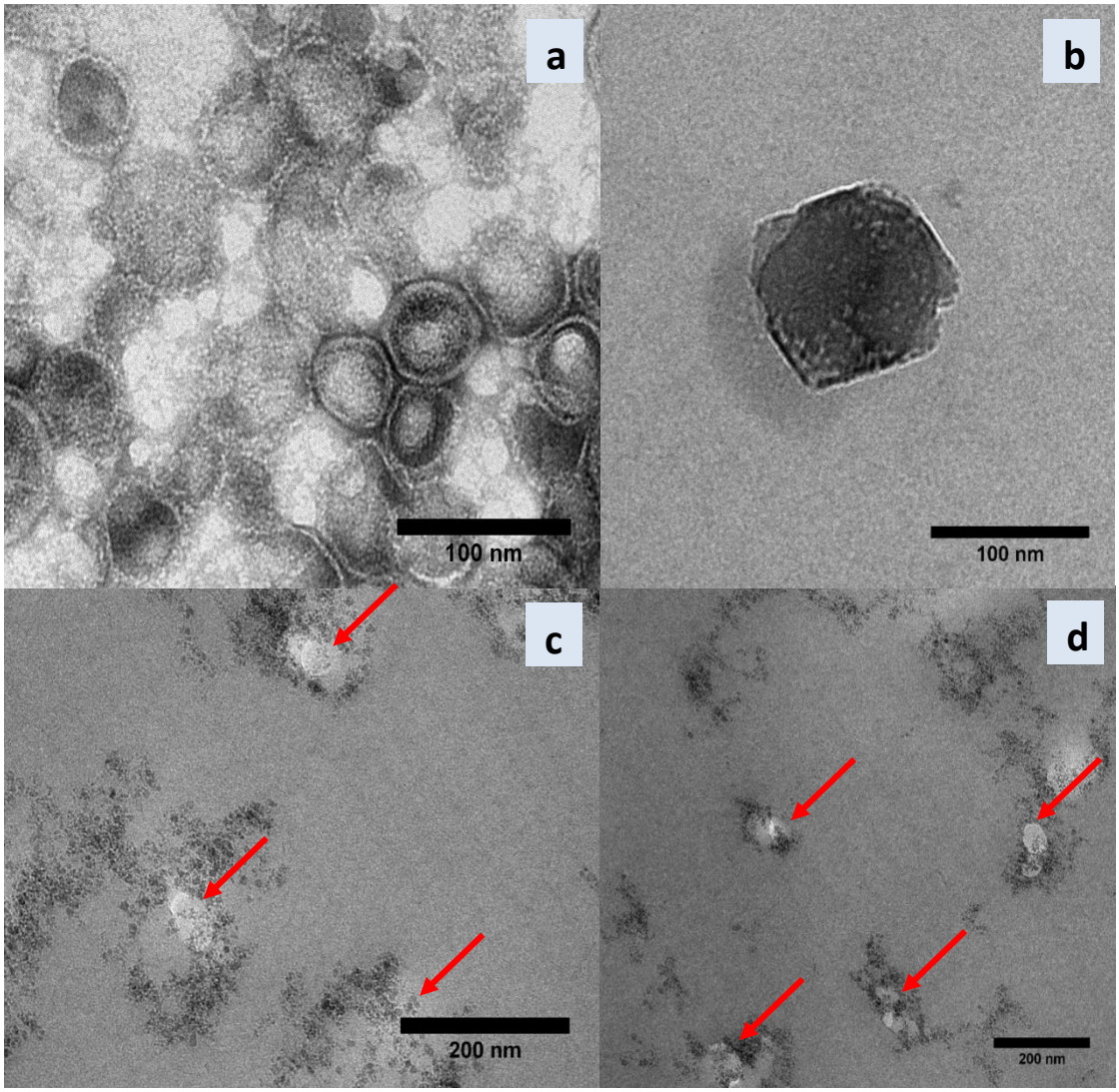

Figure 49: (a) TEM images of empty viral capsid shells, (b) capsid shell after magnetite precipitating and (c & d) HRTEM images after FIB cuts of capsids after magnetite precipitation. The red arrows indicate empty capsid shells.

Magnetite was precipitated in the presence of capsid shells under physiological conditions. Empty capsid shells are shown in Figure 49a. After magnetite precipitation in the presence of capsids, capsid structures are shown in TEM images (Figure 49b) after dialysis and several washing steps. It was promising that magnetite nanoparticles could have formed within the capsid, but due to TEM images, magnetite nanoparticles were solely observed at the outside of the capsid shells. Hence, it was not clear if magnetite nanoparticles have formed within

capsid shells. Therefore, the focused ion beam (FIB) was used to cut capsid shells. The capsid shells were completely empty as it is indicated by red arrows in Figure 49c, d. Magnetite nanoparticles were just precipitated on the capsid shells and no magnetite was observed within capsid shells.

MAGNETITE CALCITE COMPOSITE MATERIALS

Calcite is a natural occurring material, highly present in the biological and geological world (Cölfen and Antonietti, 2008). Synthetic single crystals are mainly composed of homogenous solids, whereas biogenic single crystals are inhomogeneous solids through their incooperated biomacromolecules. The incooperated materials control the properties of the sub-calcite-structure. It is of great interest to achieve non intrinsic properties of foreign materials into calcite crystals and create new material properties within those crystals. The incorporation material can be made of organic nature, or/and nano materials. Calcite crystals were recently grown in the presence of small molecules, such as nanoparticles comprising specific surface chemistry. Hydrogels were used to embed those nanomaterials within calcite crystals and the formation of micro-sized composites was performed. Composite materials are of great interest in the nano-scale level. Calcium carbonate plays an important role several organisms and exhibit a complex structure, which is hierarchically ordered (Faivre and Schuler, 2008), (Bahareh et al., 2015), (Sviben et al., 2016), (Siglreitmeier et al., 2015), (Bindschedler et al., 2016). The mineral phase of biominerals is always associated with organic molecules. These molecules are mostly located within the crystals or between crystal units. Also single crystal biominerals exhibit mechanical properties more improved than their synthetic counterparts. It is of great interest to incooperated new features in the calcium carbonate materials, such as magnetic features through magnetic particles.

VAPOR DIFFUSION DECOMPOSITION METHOD

The precipitation of calcium carbonate is obtained by a diffusion process of carbon dioxide vapor into a calcium chloride solution according to the following reaction (Aizenberg et al., 1999), using slow diffusion of ammonium carbonate (ammonia (NH_3) and carbon dioxide (CO_2) gases) using the vapor diffusion decomposition method (Figure 50).

$$(NH_4)_2CO_3\,(s) \rightarrow 2NH_3\,(g) + CO_2\,(g) + H_2O \qquad \textit{Eq. 14}$$

$$CO_2 + Ca^{2+} + H_2O \rightarrow CaCO_3\,(s) + 2H^+ \qquad \textit{Eq. 15}$$

$$2NH_3 + 2H^+ \rightarrow 2NH_4^+ \qquad \textit{Eq. 16}$$

Calcite, which is the least soluble phase, favors to crystallize before other more soluble polymorphs can form. CO_2 vapor interacts with the dissolved Ca^{2+} ions within the solution and crystallize to $CaCO_3$. NH_3 converts to NH^{4+} through additional hydrogen atoms created by the conversion into $CaCO_3$ (Aizenberg et al., 1999).

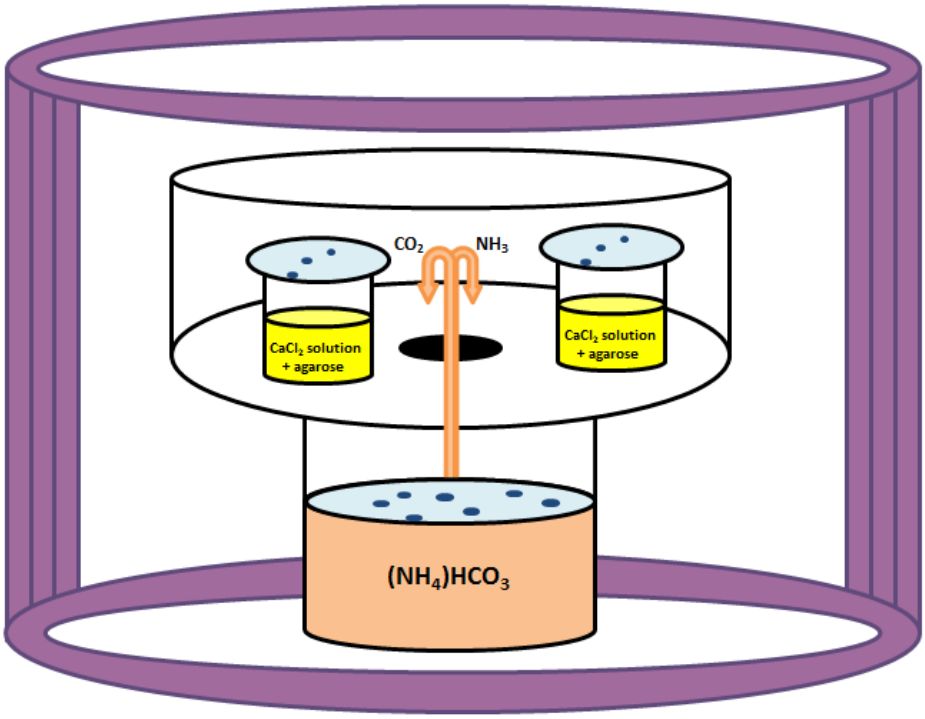

Figure 50: Vapor Diffusion Decomposition: Calcite can be produced using the vapor diffusion decomposition method, whereas $CaCl_2$ solutions are placed in small vials within a desiccator. $(NH_4)HCO_3$ powder is used to saturate the atmosphere. The desiccator is additionally surrounded by Helmholtz coils to achieve a magnetic field and align magnetic fillers within hydrogels containing $CaCl_2$.

EXPERIMENTAL

CRYSTALLIZATION

So called magnetic fillers, e.g. polyR-magnetite nanoparticles, pure magnetite nanoparticles, nanoparticles (later decorated with PolyR), or AMB-1 magnetosomes, were added to a 50 mM $CaCl_2$ solution containing 1 wt% low melt agarose. As a basic buffer 1M ammonium hydroxide ($(NH_4)OH$) was added to 1 M of ammonium chloride (NH_4Cl) whereas OH ions were present at 50 mM. Magnetic fillers were added at 1 mg/mL. Gels were dissolved at 60 °C with the $CaCl_2$ prior to addition of magnetic fillers. Each final sample volume amounted to 3 ml in a 15 ml screw cap glass container. All gels set within a magnetic field created by the Helmholtz coils. The magnetic flux density was set to 3.5 mT. Ammoniumcarbonat ($(NH_4)_2CO_3$) at 3 g/reaction was crushed and added to a petri dish, sealed with Parafilm. Thereafter, 7 holes were poked into the film with a syringe needle. The reaction vessels were closed using Parafilm and 3 holes were poked with a syringe needle. The reactions ran for 24 h within a closed desiccator.

PURIFICATION

The crystalline samples were removed from the desiccator, heated to 65 °C in a water bath and washed 3 times with H_2O MilliQ. The calcite was allowed to settle to the bottom of the reaction vessels, while most of the suspended magnetic fillers stayed in solution. Occasionally, the fillers, which are not occluded within crystals, would aggregate upon washing. A permanent magnet was then held above the solution to remove small aggregates through their easy movement to the magnet, which were then picked up with an absorbent paper. 3 mL of 1 % SDS solution was added to each reaction to remove the excess external material from the crystal surface. Two additional washing steps with H_2O MilliQ were performed following of two additional washes with ethanol. Samples were collected and dried at 40 °C overnight in an oven.

RESULTS AND DISCUSSION

Different magnetic fillers were used within the vapor diffusion decomposition method to incooperated them into growing calcite crystals, after their alignment and fixation (in an agarose gel) within a magnetic field. Different magnetic fillers were used, as they are shown in Figure 51. Polydisperse magnetite nanoparticles (Figure 51a) were synthesized and embedded within calcite crystals with and without any magnetic field. The same procedure was performed for polydisperse magnetite nanoparticles, which were later coated with polyR (Figure 51b), with polyR-magnetite nanoparticles (Figure 51c) and with biogenic magnetite nanoparticles, the magnetosomes of the magnetotactic bacteria strain AMB-1 (Figure 51d).

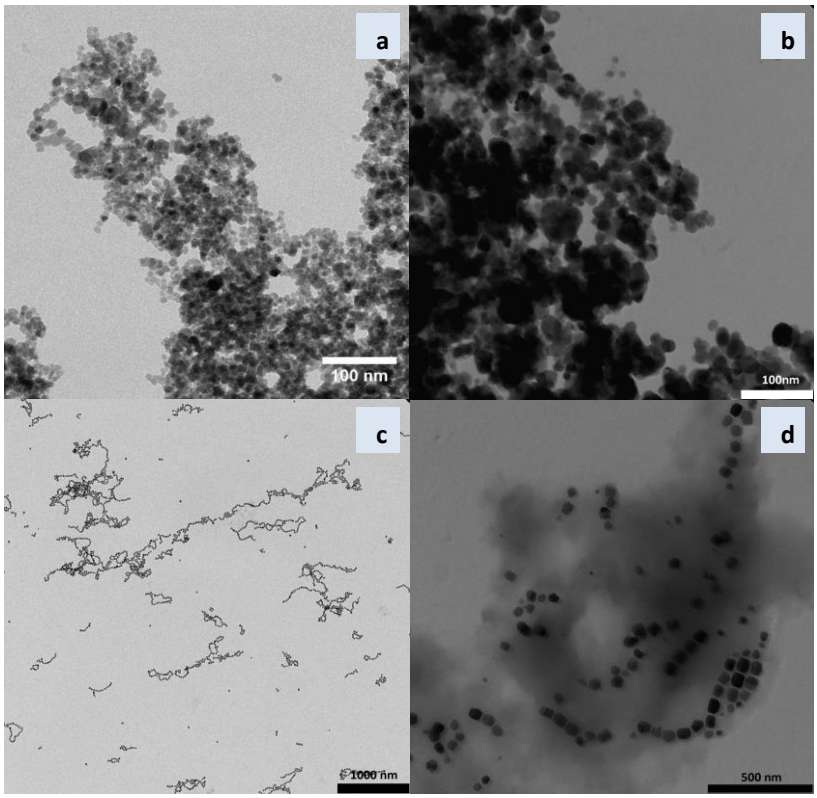

Figure 51: Magnetic fillers used for the incorporation within calcite crystals. (a) Fe_3O_4 nanoparticles, (b) Fe_3O_4 poly-l-arginine coated nanoparticles, (c) PolyR-magnetite nanoparticles (d) and AMB-1 magnetosomes.

After vapor diffusion decomposition method, SEM measurements of washed powders were performed. The different calcite crystals are shown in Figure 52. One can see that the pure

calcite control (Figure 52a) without any magnetic fillers is less porous than the observed calcite magnetite composite crystals (Figure 52b-e).

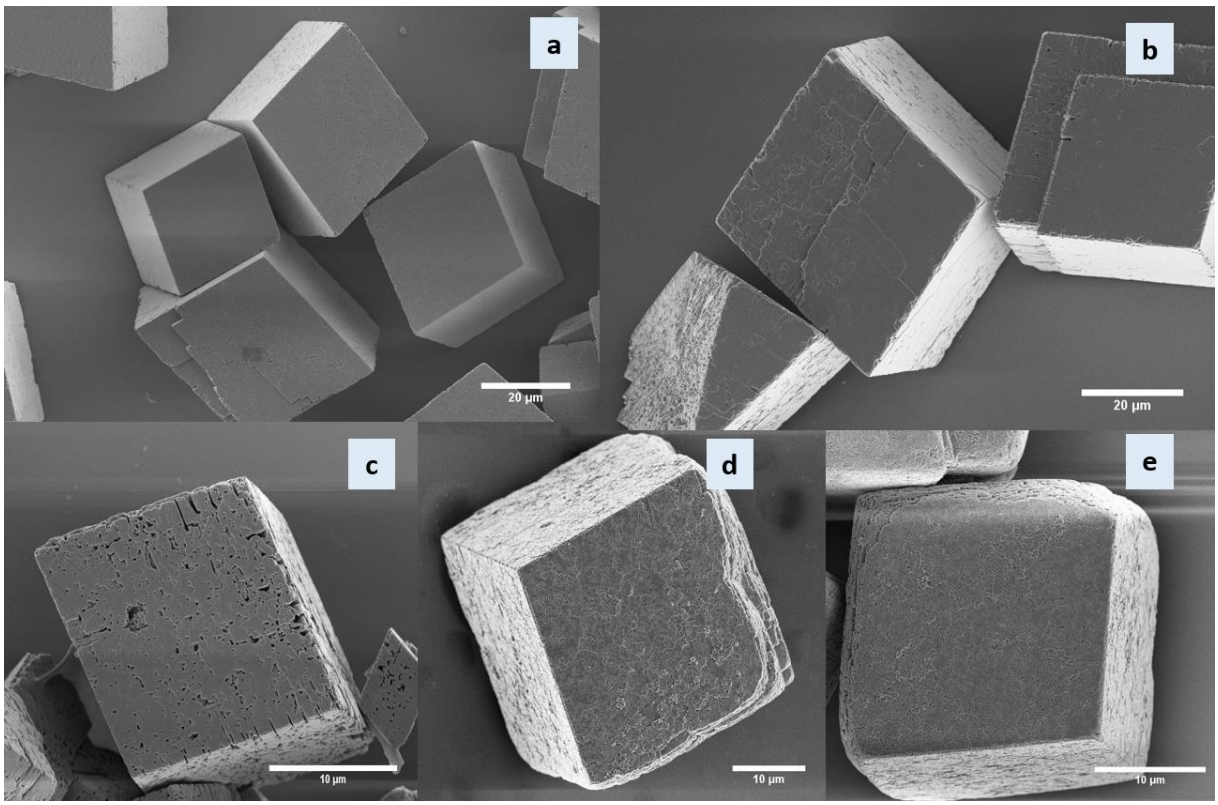

Figure 52: SEM images of calcite crystals after vapor diffusion decomposition method*. (a) Calcite control, synthesized without any magnetic fillers, (b) calcite crystals with entrapped magnetite nanoparticles (coated with polyR after synthesis), (c) PolyR-magnetite nanoparticles, (d) AMB-1 magnetosomes within an applied magnetic field and (e) AMB-1 magnetosomes without any applied magnetic field.*

To prove if magnetic fillers were embedded within calcite crystals, they were conjugated to Alexa Fluor® 488 before their entrapment. After the vapor diffusion decomposition method and purification, the crystals were analyzed using a confocal microscope and Alexa Fluor® 488 was detected. In Figure 53a, no fluorescence is detected due to the calcite crystal control, which do not consist of magnetite nanoparticles within their cavities. In Figure 53b, c, fluorescence was detected and hence, it was proven that the magnetic fillers are entrapped within the calcite crystals.

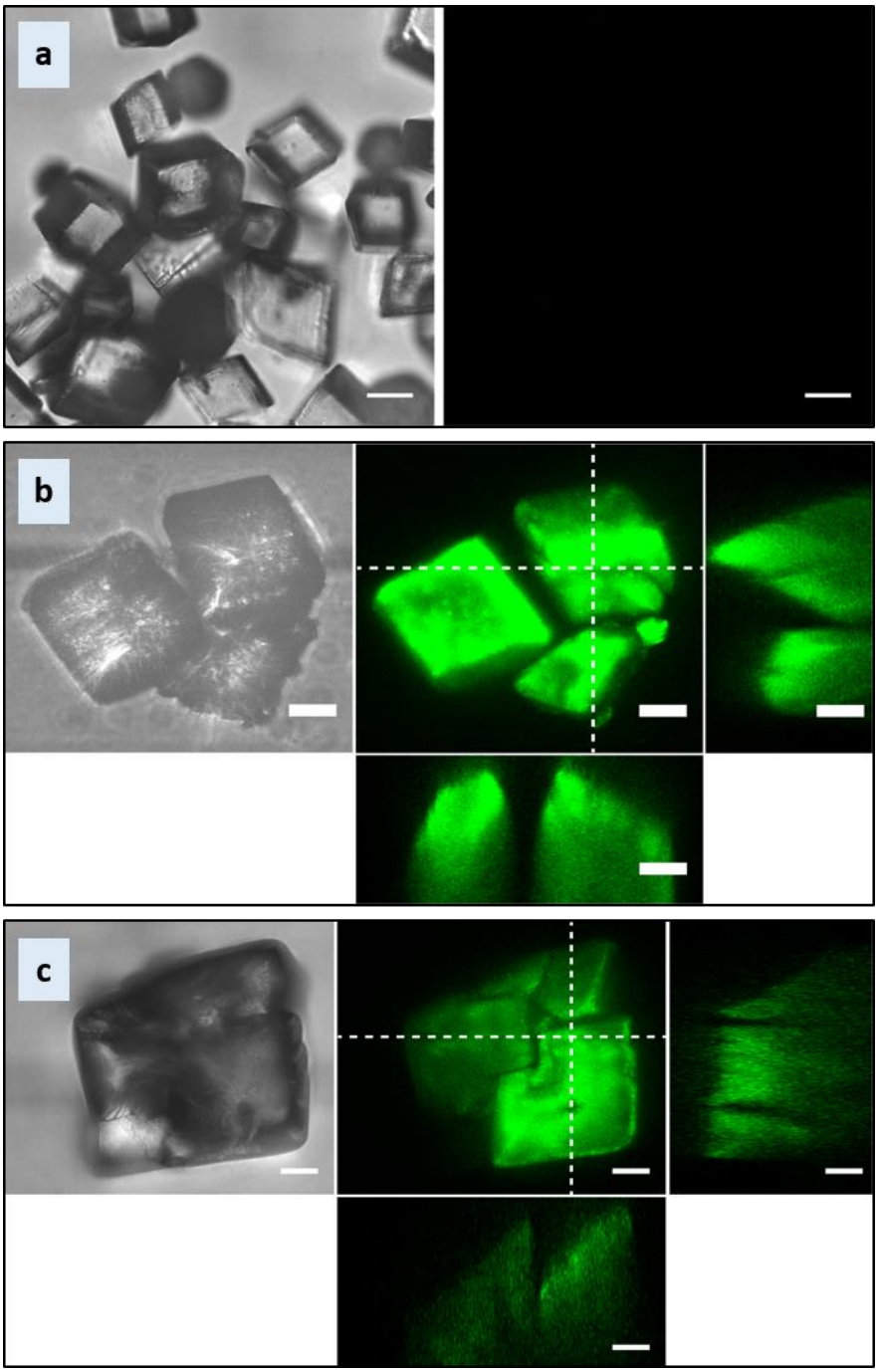

Figure 53: Alexa Fluor® 488 coated particles within calcite crystals. (a) Calcite crystal control, (b) calcite polyR-magnetite nanoparticle composites and (c) calcite magnetosome composites.

The calcite magnetite composite crystals were furthermore monitored in the optical microscope while placing a strong magnet close to a capillary filled with crystals. The crystals in the capillary were dispersed within ethanol. When moving the magnetite, one can see the crystals movement towards the magnet. The pure calcite crystal control does not react according to the magnet.

Generally speaking, it is possible to embed magnetic fillers within calcite crystals and modify the morphology of the calcite crystals towards a more porous structure. It is of great interest to embed anisotropic nanoparticles, such as polyR-magnetite nanoparticles and magnetosomes, to create new mechanical properties and occasionally change them within magnetic fields. Hence, it is very interesting to compare synthetic magnetic fillers with biogenic ones. As one can see, the new composite calcite crystals exhibit highly porous structures, which can be used for different applications, such as magnetically tunable filtration system, sensors, or encapsulation of bio-active molecules for drug delivery (Mihai et al., 2013), (Ikoma et al., 2007).

ABBREVIATIONS

PP, primary particles; SP, superparamagnetic; SSD, stable single domain; VSM, vibrating sample magnetometer; MPI, mean inner potential; FORC, first ordered reversal curve; Ms, saturation magnetization; Mrs, saturation remanent magnetization Hc, coercivity; Hcr, remanent coercivity; on; IRM, isothermal remanent magnetization; CCD, charged-coupled device; EH, electron holography; ET, electron tomography; (HR)TEM, (high resolution) transmission electron microscope; HAADF, High-angle annular dark-field; STEM, scanning TEM; EELS, electron energy loss spectroscopy; EDX, energy dispersive x-ray spectroscopy; WAXS, wide angle x-ray scattering; SAS, small angle scattering; SAXS, small angle x-ray scattering; SANS, small angle neutron scattering; SLP, specific loss power; MTB, magnetotactic bacteria; polyR, poly-l-arginine; TGA, thermogravimetric analysis.

ACKNOWLEDGMENTS

First, I would gratefully thank my supervisor PD Dr. Damien Faivre for his guidance and encouragement over the last three years. I am very glad that he always enabled creativity and scientific freedom. I am very thankful for his help in chemistry, his support at the beam lines and his never ending patience.

I would also like to thank my supervisor Prof. Dr. Elke Dittmann from University of Potsdam and my mentor Dr.habil. Richard Weinkamer for the support and for joining my thesis committee during these three years.

I would also like to acknowledge Prof. Dr. Dr. h.c. Peter Fratzl for welcoming me in the institute and for establishing a wonderful working atmosphere in the Department of Biomaterials.

A big thank goes to Dr. Emanuel Schneck and Dr. Jens Baumgartner who were always patient with me, answered all the questions about neutron scattering and magnetite and joined me for the beam times as well.

I am very thankful for the last three years and for all the wonderful people I have met. Therefore, my special thanks go to Dr. Mark Widdrat, who introduced me in the world of magnetite synthesis, Dr. Matthew Hood who had always an open ear for me and helped me through scientific challenges, Dr. Mathieu Bennet, who helped me with the fluorescence measurements, Dr. Carmen Valverde Tercedor, Dr. Agata Olszewska, Dr. Maria Antonietta Carillo and Dr. Teresa P. Gonzales, who welcomed me with open arms in the group and always supported me, my office mate Ana Licuco Massouh who became a wonderful friend, Anna Pohl, with whom I spent a great time in the lab and at the synchrotron facility, and Erika Günther, Franziska Jehle, Sara Ghaisari, Sadra Kashef and Vahid Satarifard who became not indispensable friends and colleagues. Furthermore, I would like to thank all the former and recent group members of the Magneto Group.

Special thanks also goes to my colleagues Dr. Marie Albéric, Dr. Agata Olszewska, Sara Ghaisari, Dr. Matthew Hood, Dr. Klaas Bente, Dr. Jens Baumgartner and Dr. Mathieu Bennet for accompanying me through the writing process and helped me with fruitful discussions.

Additionally, many thanks goes to our technicians, who are always helping and supporting with sample preparations and measurements, and to my students, Julia, Pierre and Aurelien, who helped and supported me in the lab. I would also like to thank our collaboration partners for the interesting and nice work together.

Last but not least, I have to emphasize that I am very thankful for the great help of my parents Sonja und HS-Prof. Dr. Erich Reichel, without their infinite love and support during the last 30 years, I would have never been there where I am now. I am very thankful for all the support of my family and friends, especially Mag. Franziska Hütter, Dipl.-Ing. Sarah Poguntke, Florian Pijanowsky, Ben Krenz and Anton. I am also extremely thankful for the biggest support, which I always get from my beloved boyfriend Stephan Ulz, who always encouraged and believed in me!

EIDESSTATTLICHE ERKLÄRUNG

Ich erkläre an Eides statt, dass ich die vorliegende Arbeit selbstständig und nur unter Verwendung der angegebenen Literatur und Hilfsmittel erarbeitet und verfasst habe.

Potsdam, am ……05.10..2016…… ……..

(Victoria E. Reichel)